University of Illinois at Urbana-Champaign

ACRC

Air Conditioning and Refrigeration Center A National Science Foundation/University Cooperative Research Center

An Experimental Investigation of Pressure Drop and Heat Transfer in Internally Enhanced Aluminum Microchannels

C. A. Monroe, T. A. Newell, and J. C. Chato

ACRC TR-213 April 2003

For additional information:

Air Conditioning and Refrigeration Center
University of Illinois
Mechanical & Industrial Engineering Dept.
1206 West Green Street
Urbana, IL 61801

(217) 333-3115

Prepared as part of ACRC Project #135
Microfinned Microchannel and Flat Plate Heat Exchangers
T. A. Newell, and J. C. Chato, Principal Investigators

The Air Conditioning and Refrigeration Center was founded in 1988 with a grant from the estate of Richard W. Kritzer, the founder of Peerless of America Inc. A State of Illinois Technology Challenge Grant helped build the laboratory facilities. The ACRC receives continuing support from the Richard W. Kritzer Endowment and the National Science Foundation. The following organizations have also become sponsors of the Center.

Alcan Aluminum Corporation
Amana Refrigeration, Inc.
Arçelik A. S.
Brazeway, Inc.
Carrier Corporation
Copeland Corporation
Dacor
Daikin Industries, Ltd.
Delphi Harrison Thermal Systems
Embraco S. A.
General Motors Corporation
Hill PHOENIX
Honeywell, Inc.
Hydro Aluminum Adrian, Inc.
Ingersoll-Rand Company
Kelon Electrical Holdings Co., Ltd.
Lennox International, Inc.
LG Electronics, Inc.
Modine Manufacturing Co.
Parker Hannifin Corporation
Peerless of America, Inc.
Samsung Electronics Co., Ltd.
Sanyo Electric Co., Ltd.
Tecumseh Products Company
The Trane Company
Valeo, Inc.
Visteon Automotive Systems
Wieland-Werke, AG
Wolverine Tube, Inc.

For additional information:

Air Conditioning & Refrigeration Center
Mechanical & Industrial Engineering Dept.
University of Illinois
1206 West Green Street
Urbana, IL 61801

217 333 3115

Abstract

Pressure drop and heat transfer measurements were taken for smooth and internally enhanced aluminum microchannels using pure R134a. Adiabatic, evaporation, and condensation tests were conducted in the horizontally-oriented test sections. Hydraulic diameters for the real dimensions of the two test sections measured 1.66 and 0.76 mm (0.065" and 0.030"), respectively. The test conditions included mass fluxes from 50 to 430 kg/m^2s (37—317 $klbm/ft^2hr$), inlet qualities of 0 to 100%, and test section heat fluxes from 2.3 to 8.0 kW/m^2 (730 to 2540 Btu/ft^2hr). All two-phase experiments were run at an inlet temperature of 5°C (41°F).

Experimental data showed an average increase of a factor of two in pressure drop for the enhanced test section, but with diminishing effects at higher mass fluxes and qualities. Heat transfer data showed an increased heat transfer coefficient in the enhanced test section, with average increases of a factor of two over the basic test section. When coupled with the area enhancement, the enhanced test section gave almost four times the heat transfer capacity of the basic test section. Condensation experiments were also conducted to try to isolate nucleate boiling effects in evaporation. Numerical simulations were constructed to help illustrate the differences between the two test sections and their potential applications.

Results from these experiments are presented in this thesis. In addition, the data is compared to pressure drop and heat transfer correlations to help explain the characteristics of the two test sections.

Table of Contents

List of Figures

Page

List of Tables

Page

Nomenclature

A	Area (m^2)
C_p	Specific Heat (kJ/kgK)
D	Diameter (m)
D_h	Hydraulic Diameter (m)
EF	Enhancement Factor
f	Fin Height (m)
f_C	Churchill Friction Factor
f_D	Darcy Friction Factor
f_F	Fanning Friction Factor
G	Mass Flux (kg/m^2s)
g	Gravitational Constant (9.81 m/s^2)
h	Enthalpy (kJ/kg)
h	Heat Transfer Coefficient (kW/m^2K)
k	Conductivity (W/mK)
L	Length (m)
M	Molecular Weight
$\dot{m}$	Mass Flow Rate (kg/s)
P	Pressure (kPa)
P_r	Reduced Pressure
PF	Penalty Factor
q''	Heat Flux (kW/m^2)
$\dot{Q}$	Heat Transfer Rate (kW)
T_r	Reduced Temperature
V	Fluid Velocity (m/s)
v	Specific Volume (m^3/kg)
x	Quality
z	Distance (m)

Greek Symbols

α	Void Fraction
Δ	Change
δ	Liquid Film Thickness (m)
ε	Effective Surface Roughness (m)
Φ	Two Phase Multiplier
μ	Viscosity (kg/ms)
ρ	Density (kg/m^3)
σ	Surface Tension (N/m)
τ_w	Perimeter Average Shear Stress (Pa)

Dimensionless Parameters

Co	Convection Number
Bo	Boiling Number
Fr	Froude Number
Nu	Nusselt Number
Re	Reynolds Number

Pe	Péclet Number
Pr	Prandtl Number
We	Weber Number
X_{tt}	Lockhart-Martinelli Parameter

Subscripts

2ϕ	Two Phase
a	Accelerational
ave	Average
cb	Convective Boiling
cr	Cross Sectional
crit	Critical
eq	Equivalent
f	Frictional
g	Gravitational
i	Inlet
l	Liquid
lo	Liquid Only
nb	Nucleate Boiling
o	Outlet
PH	Preheater
ref	Refrigerant
sat	Saturation
sub	Subcooled
surf	Surface
tp	Two Phase
TS	Test Section
v	Vapor
vo	Vapor Only
W	Wall
x	Generic Subscript

Chapter 1. Introduction

Aluminum microchannel tubes are a relatively new technology that has helped to increase the efficiency of heat exchangers. Aluminum microchannel heat exchangers offer advantages in reduced refrigerant charge with better air side and refrigerant side heat transfer when compared to conventional fin-and-tube heat exchangers. Today, microchannel heat exchangers are commonly used in the automotive industry as condensers and radiators, and are also gaining interest for use in stationary air conditioning units. A schematic of a typical microchannel heat exchanger can be seen in Figure 1.1 below:

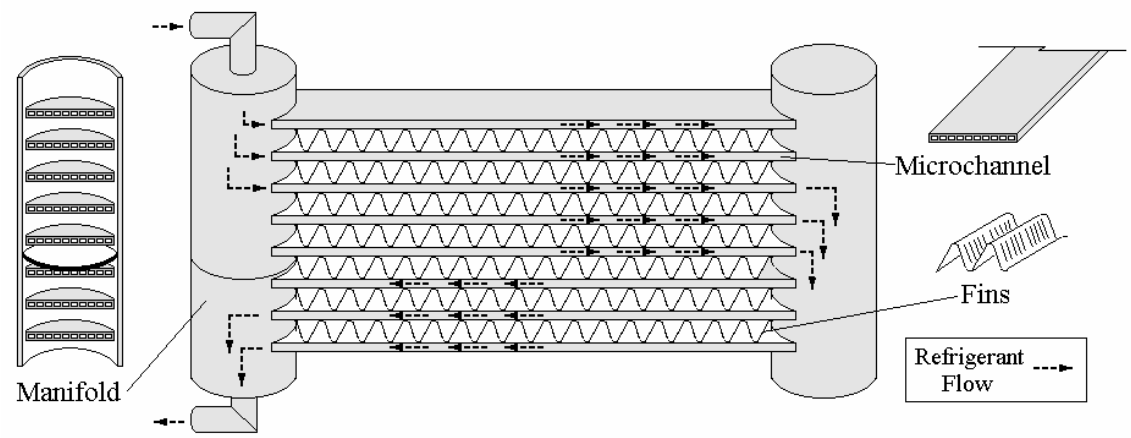

Figure 1.1: Schematic Drawing of a Microchannel Heat Exchanger

In the above schematic, refrigerant enters the heat exchanger and flows into the manifold. There is a block-off plate placed in this manifold that diverts the refrigerant into the microchannel tubes. The refrigerant then flows through the second manifold, through the next set of microchannel tubes and into the lower half of the original manifold before exiting the heat exchanger.

Aluminum microchannel tubes are flat, multi-port tubes with hydraulic diameters on the order of 0.5 to 2 mm. Please note that the prefix 'micro' implies dimensions on the order of micrometers (μm); however, in this investigation, it refers to the types of tubes described above.

Internal surface enhancements have been used extensively in copper tubes to increase their heat transfer capabilities. The motivation exists to determine if this concept can be applied to aluminum microchannels to give a better-performing aluminum microchannel. Typical internal enhancements for copper tubes are on the order of 0.2 mm in depth. Microchannels have been produced with larger scale internal enhancements in which the cross section took on an "H" profile. The surface enhancements used in this project were made on a smaller scale—the grooves were roughly 0.18 mm in width and 0.38 mm in depth with 12 grooves per port. These dimensions resulted in 10 fins per port with a width of 0.22 mm. A picture of the enhanced test section is shown in Figure 1.2 and described later in section 3.1.4.

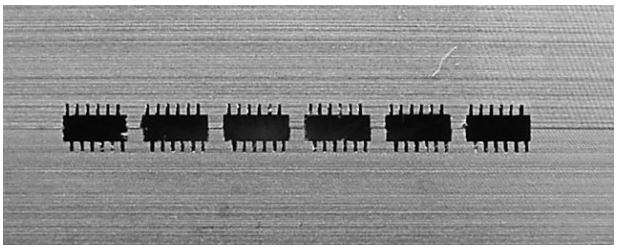

Figure 1.2: Cross Sectional View of Enhanced Test Section

1.1 Objectives of this Investigation

Heat transfer and pressure drop tests were conducted on a smooth walled 6-port microchannel test section and an enhanced test section with hydraulic diameters of 1.66 mm and 0.76 mm, respectively. Test results for R134a with mass fluxes from 50 to 450 kg/m^{2}s, at a saturation temperature of 5°C are presented. The results are compared to pressure drop and heat transfer models to help characterize the effects of the internal enhancements.

The primary goal of this project is to characterize the pressure drop and heat transfer of internally enhanced aluminum microchannel tubes in evaporation. Even though the test section was designed with rather aggressive groove geometries, the results of this investigation can be used to show the overall effects of this type of enhancement, and possibly fuel further research in this area. Current extrusion technology is limited in the ability to consistently make this type of enhancement in extruded aluminum tubes; however, further advances in technology could make this type of channel geometry a possibility. Although mass producing this type of geometry is not yet a reality, several possible applications currently exist in smaller scale production, such as electronics cooling. As stated earlier, aluminum microchannel heat exchangers are currently used as automotive condensers and radiators, in which the air side heat transfer represents the greatest restriction to overall heat transfer. In this type of application, enhancement geometries of the type studied here may not offer increased overall performance; however, their use in refrigerant-to-refrigerant or refrigerant-to-liquid heat exchangers could make effective use of the increased heat transfer capabilities.

Chapter 2. Literature Review

This chapter describes the relevant work in pressure drop and heat transfer. Several correlations are described that will be used later in the analysis, including single phase and two phase pressure drop and heat transfer correlations.

2.1 Preliminaries

A common roadblock which arises when analyzing the characteristics of channels with non-circular cross section, such as those used in this study, is how to define their inner diameter. In order to define the inner diameter of non-circular channels, the accepted practice is to use the hydraulic diameter, defined by

$$D_h \equiv \frac{4A_{cr}}{P} \tag{2.1}$$

Using this approach, the cross-sectional area A_{cr} and perimeter P are used. For a circular geometry, this definition results in the channel's standard diameter D. In the discussion in this paper, any reference to D or D_h can be considered synonymous.

2.2 Single Phase Pressure Drop

The most common way to express the pressure drop of single phase flow is to use a friction factor. The Darcy friction factor is defined as:

$$f_D = \frac{4t_w}{\frac{1}{2}rV^2} \tag{2.2}$$

where V is the fluid velocity, r is the fluid density, and t_w is the perimeter-average wall shear stress. In the literature, it is common to see several variations of the friction factor, including the Fanning f_F and Churchill f_C friction factors. These three forms of the friction factor are related by:

$$f_C = \frac{f_F}{2} = \frac{f_D}{8} \tag{2.3}$$

Table 2.1: Frequently Used Non-Dimensional Groups

Group	Interpretation	Definition
Reynolds Number, Re	Ratio of inertial to viscous forces	$\mathrm{Re} = \frac{GD_h}{m}$
Superficial Reynolds Number, Re_l, Re_v	Assumes actual phase flow occupies entire tube	$\mathrm{Re}_l = \frac{GD_h(1-x)}{m_l}$ liquid $\mathrm{Re}_l = \frac{GD_h x}{m_v}$ vapor
Phase Only Reynolds Number, Re_{lo}, Re_{vo}	Assumes flow consists of liquid or vapor only	$\mathrm{Re}_{lo} = \frac{GD_h}{m_l}$ liquid only $\mathrm{Re}_{vo} = \frac{GD_h}{m_v}$ vapor only
Liquid Froude Number, Fr_l	Ratio of inertial to gravitational forces	$Fr_l = \frac{G^2}{r_l^{\,2} g D_h}$
Liquid Weber Number, We_l	Ratio of inertial to surface tension forces	$We_l = \frac{G^2 D_h}{r_l s}$
Nusselt Number, Nu	Dimensionless heat transfer coefficient	$Nu = \frac{hD_h}{k_l}$
Liquid Prandtl Number, Pr_l	Ratio of momentum diffusivity to heat diffusivity	$\mathrm{Pr}_l = \frac{m_l c_{p,l}}{k_l}$
Turbulent Lockhart-Martinelli Parameter, X_{tt}	Ratio of vapor to liquid pressure drop	$X_{tt} = \left(\frac{1-x}{x}\right)^{0.9}\left(\frac{r_v}{r_l}\right)^{0.5}\left(\frac{m_l}{m_v}\right)^{0.1}$

For fully developed flow, the velocity profile is constant with distance along the length of the channel. A momentum balance on this region reduces to:

$$\frac{dP}{dz} = \frac{2 f_F G^2}{r D_h} = \frac{f_D G^2}{2 r D_h} \tag{2.4}$$

The above equation can be used to calculate the pressure gradient of any single phase flow. In order to fully implement the equation, the friction factor must be known. Much work has been done to find friction factor equations that can accurately predict the friction factor of single phase flows. The following discussion will highlight some of the work that has been done in this area.

2.2.1 Fully Developed Laminar Flow

The axial momentum equation can be solved to analytically determine the friction factor equation for fully developed laminar flow. For circular channels, the result of that analysis results in the simple equation:

$$f_D = \frac{64}{\mathrm{Re}} \tag{2.5}$$

2.2.2 Fully Developed Turbulent Flow

As seen in the previous equation, finding the friction factor for laminar flow is straightforward. For turbulent flow, however, the flow field becomes very complicated and solving the momentum equation becomes impossible. Therefore, the turbulent friction factor is typically computed through the use of correlations built on experimental data. Many correlations exist to calculate this friction factor, and several of these works will be discussed in this section.

It is commonly accepted that the transition to turbulence occurs near a Reynolds number of 2300 for circular ducts, although the transition to fully turbulent flow can occur up to a Reynolds number of 4000. Prandtl et al. (1935) developed a friction factor correlation to model turbulent flow in a smooth walled pipe.

$$\frac{1}{\sqrt{f_D}} = 0.8686 \ln\left(\mathrm{Re}\sqrt{f_D}\right) - 0.9967 \tag{2.6}$$

Nikuradse (1933) developed a correlation to model the pressure drop in a fully rough pipe:

$$\frac{1}{\sqrt{f_D}} = 0.8687 \ln\left(3.707 \frac{D}{e}\right) \tag{2.7}$$

where *e* is the effective surface roughness. As can be seen, the friction factor is independent of Reynolds number for a fully rough pipe.

Colebrook (1939) combined the two equations above and developed a friction factor correlation that spanned the smooth and fully rough regions, including the intermediate transitionally rough zone.

$$\frac{1}{\sqrt{f_D}} = 1.74 - 0.8686 \ln\left(\frac{e}{D} + \frac{18.7}{\mathrm{Re}\sqrt{f_D}}\right) \tag{2.8}$$

Churchill (1977a) developed an explicit friction factor equation that spans all laminar and turbulent flow regimes as well as all pipe roughnesses.

$$f_C = \left[\left(\frac{8}{\mathrm{Re}} \right)^{12} + \frac{1}{(A+B)^{3/2}} \right]^{1/12} \tag{2.9}$$

$$A = \left[2.457 \cdot \ln\left(\frac{1}{(7/\mathrm{Re})^{0.9} + 0.27e/D} \right) \right]^{16} \tag{2.10}$$

$$B = \left(\frac{37530}{\mathrm{Re}} \right)^{16} \tag{2.11}$$

In addition to the correlation equations presented above, a graphical form exists to evaluate the friction factor. In this classical work, Moody (1944) developed a graphical representation of friction factor plotted against Reynolds number, based on the previous work of Colebrook (equation 2.8).

2.3 Two Phase Pressure Drop

In two phase flow, the pressure drop has three contributing factors: frictional, accelerational, and gravitational dissipation.

$$\left.\frac{dP}{dz}\right)_{tp} = \left.\frac{dP}{dz}\right)_f + \left.\frac{dP}{dz}\right)_a + \left.\frac{dP}{dz}\right)_g \tag{2.12}$$

The gravitational term can be ignored for horizontal flow. The accelerational pressure drop term applies when the refrigerant flow is undergoing a quality change, for example, during evaporation or condensation. A momentum balance is used to calculate this term if the void fraction is known.

$$\left.\frac{dP}{dz}\right)_a = -\frac{G^2}{L}\left[\left\{ \frac{x_o^2}{r_v a_o} + \frac{(1-x_o)^2}{r_l(1-a_o)} \right\} - \left\{ \frac{x_i^2}{r_v a_i} + \frac{(1-x_i)^2}{r_l(1-a_i)} \right\} \right] \tag{2.13}$$

The final contribution to the pressure drop, the frictional dissipation term, is usually calculated through the use of correlations based on experimental results. These correlations are made to calculate a two phase multiplier, Φ^2, which relates the two phase frictional pressure drop in terms of either the single phase liquid or vapor pressure drop.

$$\left.\frac{dP}{dz}\right)_f = \Phi_l^2 \left.\frac{dP}{dz}\right)_l \tag{2.14a}$$

$$\left.\frac{dP}{dz}\right)_f = \Phi_v^2 \left.\frac{dP}{dz}\right)_v \tag{2.14b}$$

$$\left.\frac{dP}{dz}\right)_f = \Phi_{lo}^2 \left.\frac{dP}{dz}\right)_{lo} \tag{2.14c}$$

$$\left.\frac{dP}{dz}\right)_f = \Phi_{vo}^2 \left.\frac{dP}{dz}\right)_{vo} \tag{2.14d}$$

In the above equations, *l* is for liquid, *v* is for vapor, *lo* is for liquid only, and *vo* is for vapor only. In these interpretations, *l* and *v* imply that the actual fraction of liquid or vapor is the only flow present in the channel, while *lo* and *vo* imply that the entire flow in the channel is made up of liquid or vapor only. All of the literature that was researched for this section uses the liquid only pressure drop as a basis for the two phase pressure drop multiplier, so the ensuing discussion will be limited to the equations relevant for liquid only analysis.

As with the accelerational pressure drop becoming non-zero, another step must be taken when the refrigerant flow changes phase. The two phase pressure drop multiplier must be integrated over the range of quality change to give the frictional pressure drop:

$$\left(\frac{dP}{dz}\right)_f = \left[\frac{1}{\Delta x}\int_{x_i}^{x_o} \Phi_{lo}^2 \cdot dx\right]\left(\frac{dP}{dz}\right)_{lo} \tag{2.15}$$

As mentioned above, finding the two phase pressure drop begins with the liquid only pressure drop, which is given by:

$$\left(\frac{dP}{dz}\right)_{lo} = -\frac{2 f_{lo} G^2}{r_l D_h} \tag{2.16}$$

In the above equation, the single phase friction factor f_{lo} can be calculated through either

$$f = 0.079\,\mathrm{Re}^{-0.25} \tag{2.17a}$$

or

$$f = 0.046\,\mathrm{Re}^{-0.20} \tag{2.17b}$$

The two equations above represent the Fanning form of the friction factor (see equation 2.3), which is used in all further analysis. Incropera and Dewitt (1996) suggest that equation 2.17a be used for $\mathrm{Re} < 2\cdot10^4$ while equation 2.17b should be used for $\mathrm{Re} > 2\cdot10^4$.

In order to account for entrance and exit effects, the equations suggested by Collier and Thome (1996). For the test section inlet, the equation below represents the pressure loss from a sudden contraction of a two phase flow.

$$\Delta P_i = \left(\frac{G}{C_c}\right)^2 (1-C_c)\left[\frac{(1+C_c)\left\{\frac{x^3 v_v^3}{a^2} + \frac{(1-x)^3 v_l^2}{(1-a)^2}\right\}}{2[x v_v + (1-x) v_l]} - C_c\left\{\frac{x^2 v_v}{a} + \frac{(1-x)^2 v_l}{(1-a)}\right\}\right] \tag{2.18}$$

For the test section outlet, the pressure loss from a sudden expansion is:

$$\Delta P_o = G^2 s\,(1-s)\,v_l\left[\frac{(1-x)^2}{(1-a)} + \frac{v_v}{v_l}\frac{x^2}{a}\right] \tag{2.19}$$

In the above equations, σ and C_c are functions of the cross-sectional areas of the two regions of interest for the pressure drop, and are defined in by Collier and Thome in their book.

2.3.1 Large Tube Pressure Drop Correlations

Friedel (1979) developed a pressure drop correlation based on experimental results from horizontal, vertical up, and vertical down tests with water, R12, air-water, and air-oil mixtures. Several types of tubes were used, including circular and rectangular tubes, and the smallest diameter tested was 4 mm. For horizontal flow, Friedel's correlation includes dependence on ratios of density, viscosity, and single phase friction factors. The flow quality and Froude and Weber numbers are used in the model.

$$\Phi_{lo}^{\ 2} = C_1 + \frac{3.24 C_2}{\mathrm{Fr}^{0.045}\mathrm{We}^{0.035}} \tag{2.20}$$

$$C_1 = (1-x)^2 + x^2\left(\frac{r_l}{r_v}\right)\left(\frac{f_{vo}}{f_{lo}}\right) \tag{2.21}$$

$$C_2 = x^{0.78}(1-x)^{0.224}\left(\frac{r_l}{r_v}\right)^{0.91}\left(\frac{m_v}{m_l}\right)^{0.19}\left(1-\frac{m_v}{m_l}\right)^{0.7} \tag{2.22}$$

where the two phase Froude and Weber numbers are as follows:

$$\mathrm{Fr} = \frac{G^2}{r_{2f}^{\ 2} D_h g} \tag{2.23}$$

$$\mathrm{We} = \frac{G^2 D_h}{r_{2f} s} \tag{2.24}$$

$$r_{2f} = \frac{r_l r_v}{x r_l + (1-x) r_v} \tag{2.25}$$

for the friction factors required in equation 2.21 above, the following equations are used. In these equations, *x* is a general subscript that implies the phase of interest, so either *l* or *v* should be substituted for actual implementation.

For $\mathrm{Re}_x < 1055$: $f_{xo} = \frac{16}{\mathrm{Re}_x}$ (2.26a)

For $\mathrm{Re}_x > 1055$: $f_{xo} = 0.25\left[0.86859 \ln\left(\frac{\mathrm{Re}_x}{1.964\ln(\mathrm{Re}_x) - 3.8215}\right)\right]^{-2}$ (2.26b)

Jung and Radermacher (1989) developed a correlation based on experimental results using pure and mixed combinations of R22, R114, R12, and R152a in evaporation under a uniform heat flux. The tube used in this work is a circular 9.1 mm inner diameter 304 stainless steel tube with smooth inner walls. Jung and Radermacher found that their experimental data is well correlated by the Lockhart-Martinelli parameter. Their correlation is relatively simple to implement and is of the form:

$$\Phi_{lo}^{\ 2} = 12.82 X_{tt}^{\ -1.47}(1-x)^{1.8} \tag{2.27}$$

As used above, the Lockhart-Martinelli parameter is a common parameter used in many pressure drop and heat transfer correlations. In this classical work, referenced quite often in the literature, Lockhart and Martinelli (1949)

found that their pressure drop results could be correlated by a parameter *X* which depends on quality and fluid properties. Their experiments included analyzing air flowing with liquid phases of benzene, kerosene, water, and oils in pipes with diameters from 1.4 to 4 mm. The *tt* subscripts indicated that the liquid and vapor phases are both turbulent, which is commonly assumed for two phase refrigerant flows.

$$X_{tt} = \left(\frac{1-x}{x}\right)^{0.9}\left(\frac{r_v}{r_l}\right)^{0.5}\left(\frac{m_l}{m_v}\right)^{0.1} \tag{2.28}$$

Souza et al. (1993) studied pressure drop of R12 and R134a, flowing with and without oil. The oils used were PAG and ester oils for R134a and mineral oils for R12, in concentrations of 0 to 5% by weight. A 10.9 mm inner diameter smooth copper tube was used, and their tests were run in evaporation. Their correlation is as follows:

$$\Phi_{lo}^{\ 2} = \left(1.376 + c_1 X_{tt}^{\ -c_2}\right)(1-x)^{1.75} \tag{2.29}$$

$$c_1 = \begin{cases} 4.172 + 5.480\mathrm{Fr}_l - 1.564\mathrm{Fr}_l^{\ 2} & (0 < \mathrm{Fr}_l \le 0.7) \\ 7.242 & (Fr_l > 0.7) \end{cases} \tag{2.30}$$

$$c_2 = \begin{cases} 1.773 - 0.169\mathrm{Fr}_l & (0 < \mathrm{Fr}_l \le 0.7) \\ 1.655 & (Fr_l > 0.7) \end{cases} \tag{2.31}$$

The liquid Froude number is defined as (differently than in equation 2.23):

$$\mathrm{Fr}_l = \frac{G^2}{r_l^{\ 2} g D_h} \tag{2.32}$$

For their work, Souza et al. defined the Lockhart-Martinelli parameter as:

$$X_{tt} = \left(\frac{1-x}{x}\right)^{0.875}\left(\frac{r_v}{r_l}\right)^{0.5}\left(\frac{m_l}{m_v}\right)^{0.125} \tag{2.33}$$

2.3.2 Microchannel Pressure Drop Correlations

Yang and Webb (1996) examined adiabatic, single phase and two phase pressure drop of R12 flowing in smooth and microfinned rectangular microchannels. The hydraulic diameters of the two test sections were 2.64 and 1.56 mm, respectively. They observed that the pressure drop of the microfinned tube was higher than that of the smooth tube at the same flow conditions. They found that using an equivalent mass velocity concept originally suggested by Ackers et al. (1959) correlated their data well, instead of using the Lockhart-Martinelli parameter, which did not correlate their small tube data very well. Their correlation is given by the following set of equations:

$$\left(\frac{dP}{dz}\right)_{2f} = \frac{2 f \,\mathrm{Re}_{eq}^2 \, m_l^2}{r_l D_h^3} \tag{2.34}$$

$$\mathrm{Re}_{eq} = \frac{G_{eq} D_h}{m_l} \tag{2.35}$$

$$G_{eq} = G\left[(1-x) + x\left(\frac{r_l}{r_v}\right)^{0.5}\right] \tag{2.36}$$

$$f_{lo} = 0.0676\,\mathrm{Re}_l^{-0.22} \tag{2.37}$$

$$f = f_{lo}\left(0.435\,\mathrm{Re}_{eq}^{0.12}\right) \tag{2.38}$$

Zhang and Kwon (1999) developed a correlation based on their work with R22, R134a, and R404A. They used 6.2 and 3.25 mm copper tubes and a multi-port extruded aluminum microchannel with hydraulic diameter of 2.13 mm. Their results were correlated by the following two phase pressure drop multiplier:

$$\Phi_{lo}^{\ 2} = (1-x)^2 + 2.87x^2 P_r^{-1} + 1.68x^{0.8}(1-x)^{0.25}(P_r)^{-1.64} \tag{2.39}$$

In their work, Zhang and Kwon used equation 2.17b for their single phase friction factor, and the reduced pressure P_r is defined as:

$$P_r = \frac{P_{sat}}{P_{crit}} \tag{2.40}$$

Tran et al. (2000) studied the two phase pressure drop of pure R134a, R12, and R113 under evaporation. The channels used in their study include 2.46 mm brass and 2.92 mm stainless steel round tubes and a 4.06 x 1.7 mm brass rectangular channel. Their correlation is given by:

$$\Phi_{lo}^{\ 2} = \left[1 + \left(4.3\Gamma^2 - 1\right)\left(\mathrm{N}_{conf}\, x^{0.875}(1-x)^{0.875} + x^{1.75}\right)\right] \tag{2.41}$$

$$N_{conf} = \frac{\left[\dfrac{s}{g(r_l - r_v)}\right]^{0.5}}{D_h} \tag{2.42}$$

$$\Gamma = \left(\frac{r_l}{r_v}\right)^{0.5}\left(\frac{m_v}{m_l}\right)^{0.125} \tag{2.43}$$

2.4 Single Phase Heat Transfer

Many options exist for finding the single phase heat transfer coefficient. In this section, several correlations will be presented for both laminar and turbulent single phase heat transfer coefficients.

In single phase heat transfer, the heat transfer coefficient is usually expressed in terms of the dimensionless Nusselt number:

$$Nu = \frac{hD}{k} \tag{2.44}$$

2.4.1 Fully Developed Laminar Heat Transfer

Incropera and Dewitt (1996) present theoretical results for the solution of the energy equation for fully developed laminar conditions. For the case of constant surface heat flux, the Nusselt number is shown to be equal to 4.36. For the constant surface temperature boundary condition, the Nusselt number is found through an iterative procedure to be equal to 3.66.

In their book, Shah and London (1978), present a method for calculating the laminar heat transfer in a circular duct. Their analysis takes into account axial conduction in the fluid, and is expressed in terms of the Péclet number:

$$Pe \equiv \mathrm{Re} \cdot \mathrm{Pr} \tag{2.45}$$

For the constant wall temperature boundary condition, their equations are:

$$Nu = 3.6568\left(1 + \frac{1.227}{Pe^2} + ...\right) \quad \text{For Pe} > 5 \tag{2.46a}$$

$$Nu = 4.1807\left(1 - 0.0439Pe\right) \quad \text{For Pe} < 1.5 \tag{2.46b}$$

For Pe values outside of the range covered in equations 2.46, Shah and London present a table for the Nusselt number. After implementing this correlation, it was found that this relation gave the same value as the correlation by Churchill (1977b), described below for equation 2.52.

In addition to the relation valid for circular ducts, Shah and London also present an equation valid for rectangular ducts. For the constant wall temperature boundary condition, they express the Nusselt number in terms of the aspect ratio a as follows:

$$Nu = 7.541\left(1 - 2.610a + 4.970a^2 - 5.119a^3 + 2.702a^4 - 0.548a^5\right) \tag{2.47}$$

where the aspect ratio α is the ratio of the channel height to the channel width. For rectangular channels similar to those used in this investigation, the aspect ratio will have a value less than one. When inspecting equation 2.47, it is seen that the laminar Nusselt number is only a function of channel dimensions.

2.4.2 Fully Developed Turbulent Heat Transfer

As in single phase pressure drop, predicting the single phase turbulent heat transfer is much more difficult than predicting the laminar heat transfer. Due to these additional difficulties, the prediction of turbulent heat transfer is typically accomplished through the use of empirical correlations.

In Incropera and Dewitt (1996), several turbulent heat transfer correlations are presented. For heat transfer in a smooth circular tube, the classic work by Colburn (1933) resulted in the following correlation:

$$Nu = 0.023\,\mathrm{Re}^{4/5}\,\mathrm{Pr}^{1/3} \tag{2.48}$$

Dittus and Boelter (1930) developed a slightly different form of the above equation, which is also preferred over the Colburn equation. The Dittus-Boelter equation is:

$$Nu = 0.023\,\mathrm{Re}^{4/5}\,\mathrm{Pr}^{n} \tag{2.49}$$

where n=0.4 for fluid heating and n=0.3 for fluid cooling.

Gnielinski (1976) presented several methods for improved prediction of turbulent heat transfer. He reported that the Hausen equation underpredicted Nu at high values of Re. His work resulted in an improved correlation based on the work of Petukhov (1970) that accounts for the decrease in Nu as Re becomes smaller.

$$Nu = \left(\frac{(f_F/2)(\mathrm{Re}-1000)\,\mathrm{Pr}}{1+12.7\sqrt{f_F/2}(\mathrm{Pr}^{2/3}-1)} \right) \left(1+\left[\frac{D}{L}\right]^{2/3} \right) \left[\frac{\mathrm{Pr}}{\mathrm{Pr}_W}\right]^{0.11} \tag{2.50}$$

where Pr_w implies the Prandtl number evaluated at the wall temperature. In the above equation, the friction factors are found according to:

$$4f_F = \left[1.82\ln(\mathrm{Re})-1.64\right]^{-2} \quad \text{for Re} > 10^4 \tag{2.51a}$$

$$4f_F = 0.3164\,\mathrm{Re}^{-0.25} \quad \text{for } 2300 < \mathrm{Re} < 10^4 \tag{2.51b}$$

Churchill (1977b) developed an asymptotic form heat transfer correlation applicable for all ranges of Re and Pr:

$$Nu = Nu_l^{10} + \left[\left(\frac{\exp\left[\frac{2200-\mathrm{Re}}{365}\right]}{Nu_l^2} \right) + \left(Nu_o + \frac{0.079\sqrt{f_C}\,\mathrm{Re}\,\mathrm{Pr}}{(1+\mathrm{Pr}^{4/5})^{5/6}} \right)^{-2} \right]^{-5} \tag{2.52}$$

where f_C is calculated with equation 2.8. For the constant heat flux boundary condition, Nu_l=4.364 and Nu_o=6.3. For the constant temperature boundary condition, Nu_l=3.657 and Nu_o=4.8.

2.5 Two Phase Heat Transfer

Two methods are commonly found in the literature as the form of two phase heat transfer correlations. The first, similar to the two phase pressure drop correlations, uses a two phase multiplier to express the two phase heat transfer in terms of the single phase liquid heat transfer. The second type is a superposition method that combines convective and nucleate boiling terms to compute the two phase heat transfer coefficient. The idea behind the superposition method is that, for certain flow regimes, either of the two terms will dominate the heat transfer, so this method allows that term to have an increasing effect without suppressing the limited contribution from the other heat transfer contribution.

2.5.1 Two Phase Multiplier Heat Transfer Correlations

Gungor and Winterton (1987) developed a general correlation for flow boiling in tubes and annuli in both vertical and horizontal orientations. A very large data bank of nearly 5000 data points was collected from 30 sources in the literature. The data bank includes tube diameters from 2.95 to 32 mm and several refrigerants. Gungor and Winterton used the pool boiling correlation from Cooper (1984) as the basis of their model, which is given by:

$$h_{tp} = Eh_l \tag{2.53}$$

$$E = 1+3000Bo^{0.86}+1.12\left[\frac{x}{1-x}\right]^{0.75}\left[\frac{r_l}{r_v}\right]^{0.41} \tag{2.54}$$

The single phase liquid heat transfer coefficient h_l is calculated by the Dittus-Boelter correlation (equation 2.49). If the tube is horizontal and the Froude number is less than 0.05, then E should be multiplied by

$$E_2 = Fr^{(0.1-2Fr)} \tag{2.55}$$

In their paper, Kew and Cornwell (1997), reference a correlation by Tran et al. (1995), which is given as:

$$h_{tp} = 840\left(Bo \cdot We_l\right)^{0.3}\left(\frac{r_l}{r_v}\right)^{-0.4} \tag{2.56}$$

The above equation is dimensionalized in kW/m^{2}K.

Yan and Lin (1998) investigated the evaporative heat transfer of R134a in a horizontal, circular pipe an with inner diameter of 2.0 mm. They state that the flow patterns of small diameter tubes are predominantly annular or plug, and therefore, give better heat transfer than in large tubes where stratified flow patterns are commonly observed. Consequently, Yan and Lin report that the heat transfer coefficients in their small pipe are between 30 and 80% higher than those for larger pipes (D>8.0 mm) reported in the literature. The Yan and Lin correlation is:

$$h_{tp} = (C_1 C_0^{C_2} + C_3 B_0^{C_4} Fr_{lo})(1 - X_m)^{0.8} h_l \tag{2.57}$$

where the single phase, laminar liquid heat transfer coefficient h_l is given by the virtually constant relationship:

$$h_l = 4.364\left(\frac{k_l}{D_h}\right) \tag{2.58}$$

It should be noted that the above equation was stated incorrectly in their paper. The constants C_m in equation 2.57 above are computed by the following relation, in which a table is presented for the constants $C_{m,1}$, $C_{m,2}$, and $C_{m,3}$. The reduced temperature T_r is the ratio of the actual temperature to the critical temperature.

$$C_m \equiv C_{m,1}\,\mathrm{Re}_1^{C_{m,2}}\,T_r^{C_{m,3}} \tag{2.59}$$

Yun et al. (2002) developed a correlation based on flow boiling heat transfer in horizontal micro-fin tubes. Their correlation is based on an experimental database from many different studies, using broad ranges of fin orientations, temperatures, mass fluxes, and heat fluxes. It takes into account surface tension, turbulence effects, fin height, and liquid film thickness, in addition to the standard fluid flow properties.

$$\frac{h_{tp}}{h_l} = \left[0.009622\,Bo^{0.1106}\left(\frac{P_{sat} D_h}{s}\right)^{0.3814} + 7.6850\left(\frac{1}{X_{tt}}\right)^{0.5100}\left(\frac{Gf}{m_1}\right)^{-0.7360}\right]\mathrm{Re}_l^{0.2045}\,\mathrm{Pr}_l^{0.7452}\left(\frac{d}{f}\right)^{-0.1302} \tag{2.60}$$

$$d = \frac{D_h(1-e)}{4} \tag{2.61}$$

where the single phase liquid heat transfer coefficient is given by the Dittus-Boelter correlation (Equation 2.49), and the fin height is *f*. The void fraction a is calculated by the correlation suggested by Rouhani and Axelson (1970), which had a slight error as reported by Yun et al. in their paper.

$$a = \frac{x}{r_g}\left\{1.12\left[\frac{x}{r_g} + \frac{1-x}{r_l}\right] + \frac{1.18}{G}\left[\frac{s \cdot g(r_l - r_g)}{r_l^2}\right]^{1/4}\right\}^{-1} \tag{2.62}$$

2.5.2 Superposition Heat Transfer Correlations

Wattelet et al. (1994) conducted flow boiling heat transfer experiments using R12, R22, R134a, and a R32/R125 mixture with horizontal copper tubes ranging from 7.04 to 10.92 mm inner diameters. Their correlation is based on a "greater of the two" form, which includes a natural suppression of weaker heat transfer component. Nucleate boiling and convective heat transfer terms are included in their correlation. The nucleate boiling term is based on the Cooper (1984) correlation for pool boiling, and the convective term is based on the Dittus-Boelter single phase liquid heat transfer correlation. The correlation also included a Froude number dependent term that takes into account the stratification effects on the heat transfer coefficient. The Wattelet et al. correlation is:

$$h_{tp} = \left[h_{nb}^{n} + h_{cb}^{n}\right]^{1/n} \quad \text{with n=2.5} \tag{2.63}$$

$$h_{nb} = 55 q''^{0.67} M^{-0.5} P_r^{0.12} \left[-\log_{10} P_r\right]^{-0.55} \tag{2.64}$$

$$h_{cb} = F h_1 R \tag{2.65}$$

$$F = 1 + 1.925 X_{tt}^{-0.83} \tag{2.66}$$

$$R = 1.32 Fr_1^{0.2} \quad \text{for } \mathrm{Fr}_1 < 0.25 \tag{2.67}$$

$$R = 1 \quad \text{for } Fr_1 \geq 0.25 \tag{2.68}$$

where the h_l term in equation 2.65 is given by the Dittus-Boelter correlation, equation 2.49.

Wattelet et al. reported that for annular flow at low heat fluxes, convective boiling was the dominant mode of heat transfer. As the heat flux was increased, the nucleate boiling contribution increased, particularly for low qualities and high reduced pressures.

Choi et al. (2000) studied evaporation in a horizontal smooth tube with R32, R134a, R32/143a, and R407C. A 7.75 mm inner diameter stainless steel tube served as their test section. Their correlation is:

$$h_{tp} = E h_{DB} + S h_{SA} \tag{2.69}$$

$$E = 49.971 Bo^{0.383} X_{tt}^{-0.758} \tag{2.70}$$

$$S = 0.909 Co^{0.301} \tag{2.71}$$

$$h_{SA} = 207 \frac{k_l}{bd} \left(\frac{q'' bd}{k_l T_S} \right)^{0.745} \left(\frac{r_v}{r_l} \right)^{0.581} \mathrm{Pr}_l^{0.533} \tag{2.72}$$

$$bd = 0.0146 b \left[\frac{2s}{g(r_l - r_v)} \right]^{0.5} \quad \text{with } ß = 35° \tag{2.73}$$

where h_{DB} implies the single phase liquid heat transfer coefficient given by Dittus and Boelter (equation 2.49). Choi et al. observed that the heat flux had limited effect on the heat transfer coefficient in the convective-dominated high quality flow regions.

2.5.3 Condensation Heat Transfer Correlations

Heun (1995) developed a condensation correlation based on condensation of R134a in several port shape geometries of aluminum microchannel tubes. The tubes used in their investigation included hydraulic diameters

from 0.6 to 1.5 mm in port shapes of circles, squares, triangles, enhanced squares, and small circles. The enhanced square geometry used in their study was the type referred to in the Introduction chapter, in which there is a single fin protruding from the top and bottom portions of each microchannel port. Their correlation was found to accurately predict their condensation heat transfer data:

$$h_{tp} = F_{tp} h_{l,DB} \tag{2.74}$$

$$F_{tp} = 1 + \frac{1.130}{X_{tt}^{1.064}} \tag{2.75}$$

The above correlation is a slightly modified version of the condensation heat transfer correlation suggested by Dobson (1994, 1998):

$$F_{tp} = 1 + \frac{2.220}{X_{tt}^{0.889}} \tag{2.76}$$

Chapter 3. Experimental Apparatus and Procedure

3.1 Experimental Apparatus

This section describes the experimental test facility, including the refrigerant loop, chiller loops, water loop, instrumentation, data acquisition, and test section design. Parameters calculated from the measured data are also discussed.

3.1.1 Refrigerant Loop

The purpose of the refrigerant loop is to allow continuous, controlled circulation of the refrigerant being tested. The refrigerant loop contains numerous instruments which interface with the data acquisition system to provide feedback for important test conditions, such as mass flux, quality, and temperature. The loop used for these experiments is unique in that it contains a liquid line and preheater capable of achieving the desired two phase flow conditions, but it also contains a vapor compressor that can be used in conjunction with the liquid line to supply the two phase flow. A schematic of the refrigerant loop can be seen in Figure 3.1. The refrigerant flow begins at the separation tank, where liquid is drawn from the bottom of the tank and then passes through a subcooler (Alfa Laval #CB22-10H H24E21, rated at 2.64 kW) to ensure liquid flow into the variable speed gear pump. The gear pump uses a MicroPump gear head (Cole Parmer #73004-00) connected to a variable voltage Cole Parmer power supply (#07144-04) in order to control the mass flux. After exiting the gear pump, the liquid flows through a coriolis-type mass flow meter and then into the preheater section where it can be heated to the appropriate two-phase flow condition. The preheater is constructed of three serpentine tube passes wrapped in ten electric resistance heater strips, which are powered in groups by one variable voltage and several constant voltage switches to supply the desired amount of heat. After leaving the preheater, the refrigerant flow enters the test section. The refrigerant then flows through a condenser (Alfa Laval #CB14-28H S02, rated at 4.40 kW) to remove any heat added in the test section (if applicable), as well as to lower the overall temperature of the refrigerant in the loop.

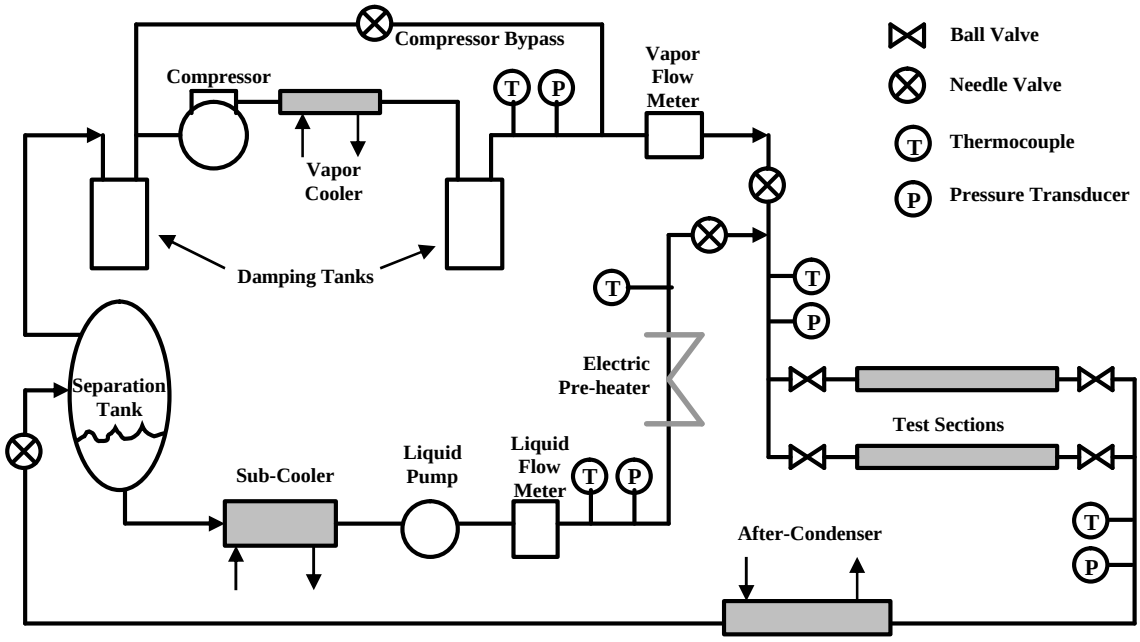

Figure 3.1: Refrigerant Loop Schematic

The refrigerant loop also contains a vapor compressor, which draws vapor from the top of the separation tank. The vapor is then drawn into the compressor, which has two 30 lb refrigerant reclamation tanks positioned before and after in order to dampen pressure oscillations caused by the reciprocating action of the compressor. After the compressor, the vapor travels through a heat exchanger to remove some of the superheat condition caused by the compressor. The heat exchanger in use here is a flat plate heat exchanger with building chilled water flowing on the opposite side. Because the vapor compressor runs at a constant speed, at this point, the vapor can go through a bypass valve to change the amount that actually enters the loop. The vapor then flows through another coriolis-type mass flow meter, after which it then meets up with the liquid line to mix and form the desired two phase flow condition. The vapor compressor in use is a Corken #D91BJ4FBB. Special seals are used in order to seal the compression chamber from the oil in the crankcase, thus allowing pure refrigerant to flow through the test loop without contamination.

3.1.2 Chiller Loops

As discussed in the previous section, the refrigerant loop uses two heat exchangers to cool the flow, which are operated as part of two separate chiller loops. The two chiller loops contain an R22/ISO 32 oil mix and use identical components, except for the heat exchangers on the experimental loop side. Each loop is powered by a compressor from a 1.5 ton (5.3 kW) window air conditioning unit. Heat picked up from the experimental loop is rejected through a Standard Refrigeration tube-in-tube condenser (TNT-150), which is connected to the building chilled water supply. A schematic of the chiller loop is shown in Figure 3.2.

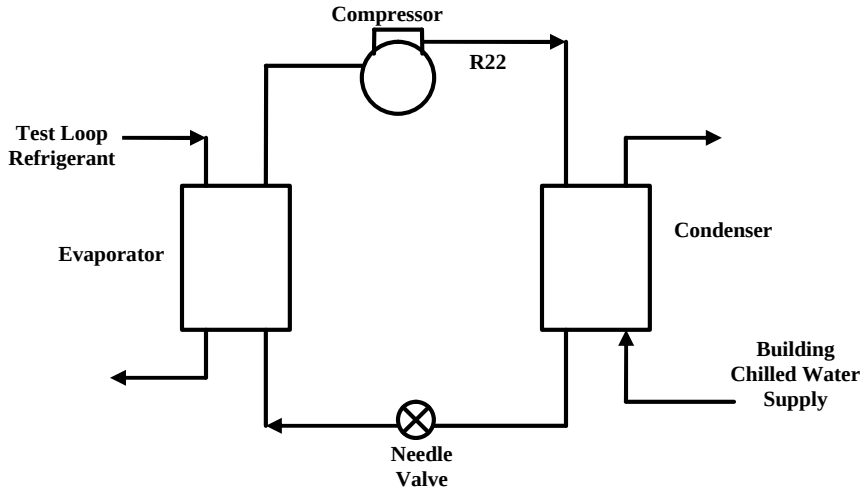

Figure 3.2: Chiller Loop Schematic

3.1.3 Test Section Water Loop

The water loop, which can be seen in Figure 3.3, is used to circulate heating or cooling water through the water jackets on the test sections. At the heart of the water loop is a Thermo Neslab (model RTE-220) constant temperature bath with digital controller, which includes electric heating elements and a vapor-compression cooling cycle that work in conjunction to provide consistent operation at a wide variety of operating temperatures. Although almost 20 years old, this unit was saved from inoperable retirement by refurbishing it with new heating coils and

electric switches to return it to original working order. The constant temperature bath also has an internal water pump which is used to pump the water through water jackets. After leaving the constant temperature bath, the water flows through a filter and then into a turbine-type volumetric flow meter (Cole Parmer #EW-32709-60). The water then goes into the selection board, which contains several valves which are used to divert the flow into either of the test sections in a parallel-flow configuration. Two direct-reading variable area flowmeters and needle valves are also present on the selection board to allow visual inspection of the flow rate and flow balancing for the two water jacket sides per test section. After being diverted into the correct test section, the water flows back into the constant temperature bath. The selection board also contains valves to allow the pressure transducers to be switched from either test section.

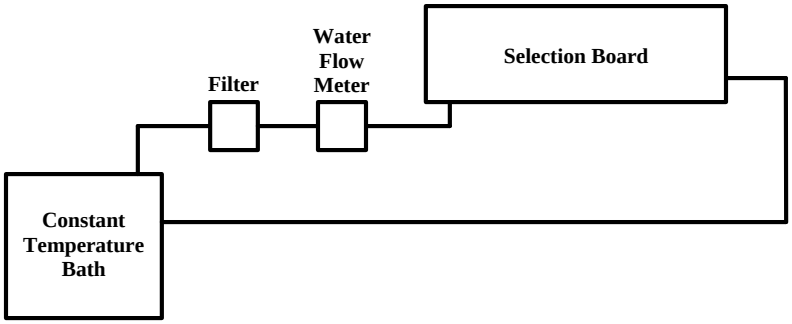

Figure 3.3: Water Loop Schematic

3.1.4 Test Section Design

Two test sections were designed for use in this project. The first test section is a basic test section with smooth walls, which was derived from a commercially-available 6-port aluminum microchannel.

The enhanced test section was designed as a derivative of the basic test section. In order to keep the cross sections of the two channels similar, the midpoint of the grooves in the enhanced test section is the same as the port depth in the basic test section. After analyzing both sections under a high-power microscope, the actual dimensions resulted in cross sectional areas that were within 0.1% of each other. This created an interesting result in that when testing at any given mass flux, the corresponding mass flow rate is the same for the two test sections. Although the enhanced test section gives the same cross sectional area, it more than doubles the heat transfer area (a factor of 2.2) when compared to the basic test section. There are 12 grooves in each of the six microchannel ports and the dimensions of the grooves are 0.178 mm (0.007 in) wide by 0.381 mm (0.015 in) deep. Figure 3.4 shows the cross section of the enhanced test section.

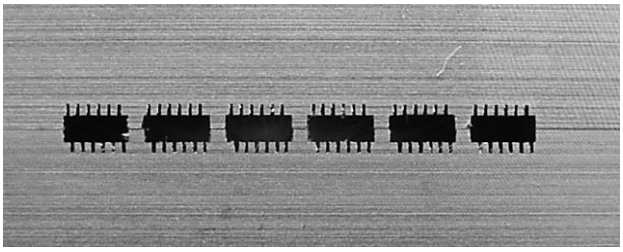

Figure 3.4: Cross Section of Enhanced Test Section

The basic and enhanced test sections have been designed and manufactured using CAD/CAM and a CNC mill to ensure accurate dimensions. Each test section consists of two symmetric halves that are bolted together. Figure 3.6 shows a CAD drawing of the entrance/exit regions of the basic test section. Each half of the test sections is made from a 7.6 x. 53.3 x 0.95 cm (3 x 21 x 3/8") bar of 2024-T4 aluminum. This figure shows the refrigerant entrance/exit hole as well as the pressure tap hole located just outside of the microchannel grooves. A thermocouple is inserted in each entrance/exit hole to give local measurement of the refrigerant temperatures. The seal groove is also visible, going around the circumference of the microchannel grooves but inside of the bolt holes. Each test section half contains four holes drilled in the side, going just below the midpoint of the microchannel grooves. These holes allow the insertion of thermocouple probes in order to measure wall temperatures for the heat transfer experiments.

Table 3.1: Measured Dimensions of Test Sections (Dimensions in mm.)

	Basic	***Enhanced***
Port Height	1.310	0.914
Port Width	2.265	2.360
# Fins	-	10
Fin Depth	-	0.381
Fin Width	-	0.215
Fin Spacing (Groove Width)	-	0.178

Table 3.1 shows the resulting dimensions of the two test sections as they were machined. Several methods are used in the literature to define the geometry of an internally enhanced channel. For example, a common way to define the diameter of an enhanced channel is to use the midplane of the grooves. For this project, three options were used to define the geometry of the enhanced test section, labeled 'full', 'mid', and 'tip' in all figures, tables, and discussion. The reason for these methods is because the behavior of the flow in the grooves is not known. By considering the different ways to express the geometry of the enhanced test section, the behavior of the flow in the grooves can be studied. The data from actual, as-machined, areas for the enhanced test section are labeled 'full', meaning the full cross sectional area is used. This data comes directly from the experimental results. The second method uses the midplane of the enhancements to define the cross section and is labeled 'mid'. This method is implemented by assuming that the grooves are only half as deep, and the lower half essentially does not exist. The final method, labeled 'tip', is implemented by assuming that there are no grooves at all, thus making it look like a slightly smaller version of the basic test section. The 'tip' geometry, therefore, uses the inscribed area in the cross section area. The two alterations in geometry ('mid' and 'tip') cause the hydraulic diameter and effective mass flux to increase. Figure 3.5 shows a visual comparison of the basic and three enhanced test section geometries, where the test section dimensions are based on the visible port shape geometries. Table 3.2 summarizes the variations caused by the three geometry definitions, in which A_{surf} represents the total surface area, including entrance and exit regions.

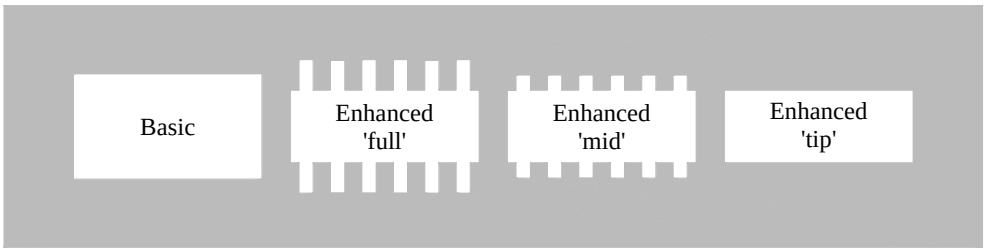

Figure 3.5: Comparison of Test Section Geometry Definitions

Table 3.2: Important Test Section Geometric Parameters

		Enhanced		
	Basic	***Full***	***Mid***	***Tip***
Dh (mm)	1.66	0.76	0.92	1.32
A_{cr} (mm^2)	17.81	17.82	15.38	12.95
A_{surf} (mm^2)	20363	41843	30346	18849

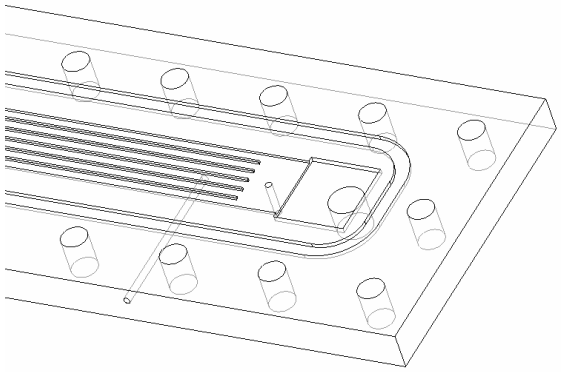

Figure 3.6: Basic Test Section

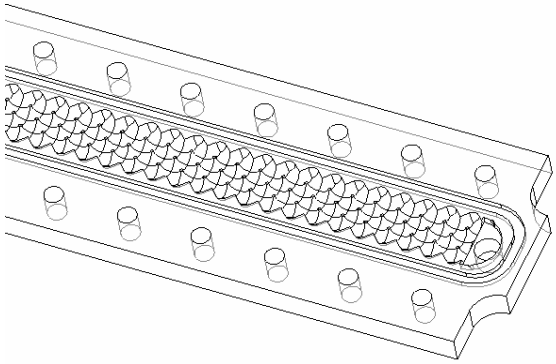

Figure 3.7: Water Jacket

In order to heat or cool the test sections for the heat transfer experiments, two water jackets are bolted to each side of the microchannel plates. Figure 3.7 shows a CAD drawing of the end of one of the water jackets, which were machined using the same bar stock as the test sections. The water jacket plates were designed so that the inlet

of the water is directly above the beginning of the microchannel grooves. A chevron surface was used for the water passage in order to increase the turbulence and mixing of the water flow.

3.1.5 Instrumentation

The experimental facility contains numerous instruments to ensure accurate measurement of critical process parameters. Measured quantities include temperature, pressure, mass flow rate, and power.

All temperature measurements are made with type-T copper-constantan thermocouple probes. Temperatures measured in the experimental apparatus include preheater inlet, preheater outlet, compressor outlet, test section inlet, test section outlet, water jacket inlet, water jacket outlet, and eight wall temperature measurements per test section. All thermocouple probes are calibrated against a NIST-traceable platinum RTD thermometer (Omega DP-251, ±0.035°C accuracy) using a constant temperature water bath. The preheater inlet, preheater outlet, and compressor outlet thermocouples are calibrated using a single point offset. All other thermocouples were calibrated 5°C beyond their range of measurement using at least eight reference points, and a first-order curve fit was then applied to these probes. Although the probes were expected to have a direct relationship between reference temperature and output voltage, the first order curve fits gave a maximum of 0.036% difference when compared to an assumed constant slope. This small difference suggests that an assumed constant slope would still result in high accuracy measurements. The thermocouple probes were spot-checked throughout the course of experimentation and found to have remained within 0.1°C of their original calibrations; therefore, the error associated with the temperature measurements is ±0.1°C.

Several pressure transducers are incorporated into the experimental apparatus in order to measure the absolute pressure at the preheater inlet, compressor outlet, and test section inlet. The pressure transducer at the preheater inlet is BEC strain-gage type transducer (GP8-46DW-D-*-C-3) with a range of 0-300 psig (0-2100 kPa) and a full scale accuracy of ±0.75%. The compressor outlet pressure is measured by a Setra (#280E) pressure transducer with a range of 0-1000 psia (0-6900 kPa) and an accuracy of ±0.25% full scale. The test section inlet pressure transducer is an Omega polysilicon strain gage type (PX215-300AI) with a range of 0-300 psia (0-2100 kPa) and an accuracy of ±0.25% full scale. A differential pressure transducer is used to measure the pressure drop across the test sections. This unit is made by Sensotec (#Z/5556-05) with a range of 0-10 psid (0-70 kPa) and an accuracy of ±0.25% full scale.

The absolute pressure transducers were all calibrated against two pressure calibrators: a Fluke #700-P07 (±1.7 kPa accuracy) and an SI Pressure Instruments #DTG-2K-30 (±1.5 kPa calibrated accuracy at range of interest). The differential pressure transducer was calibrated against a water manometer. Second order calibration curve fits were applied to all pressure transducers to ensure accurate measurements. All pressure transducers and thermocouple probes were calibrated ‘end-to-end’ while installed in the data acquisition system. This technique eliminates any errors caused by differences in measurement techniques when an external multimeter is used to measure output parameters.

As mentioned earlier, two coriolis-type mass flow meters are used to measure the mass flow rates in the liquid and vapor lines. These sensors operate by measuring the vibrational frequency of a U-tube, and a specific current is output corresponding to a given flow rate. With the use of a 250 ohm shunt resistor, the voltage is read by

the data acquisition system. The liquid mass flow meter is a Micromotion model DS0065100R with a maximum flow rate of 0.083 kg/s and an accuracy of ±0.2% of the reading. The vapor mass flow meter is a Micromotion model CMF025M314NU with a maximum flow rate of 1.89 kg/s and an accuracy of ±0.5% of the reading.

Power transducers are used to measure the power used by the electric resistance heater strips in the preheater. The power consumed by the constant voltage-supply heater strips is measured by an Ohio Semitronics #PC5-50D292. The power consumed by the variable voltage supply heaters is measured by an Ohio Semitronics #PC5-010D. Both power transducers were calibrated by the manufacturer to have an accuracy of ±0.2% of the full scale reading.

The water loop flow rate is measured by a turbine type volumetric flow meter. This flow meter was calibrated by measuring the amount of water flowing into a bucket in a certain amount of time. Over 25 calibration points were taken in the range of measurement for this experiment. To determine the volume of water for each calibration point, the mass of the bucket was measured and subtracted from the total mass with water, which was then converted using the density of water. The time period was measured with a handheld electronic stopwatch. The uncertainty of the water flow meter after calibration is assumed to be ±1% of the reading.

3.1.6 Data Acquisition

Process parameters are measured by a computerized data acquisition system comprised of a Hewlett Packard 75000 series B mainframe (E1300B) connected to a personal computer. An internal 5.5 digit multimeter (E1326B) allows measurements to be conducted from the three multiplexer boards to which the instrument outputs are connected. Two 16 channel thermocouple multiplexer modules (E1347A) are used for all temperature measurements. One 16 channel multiplexer board (E1345A) is used to measure voltage outputs (or current outputs converted to voltage) of the various pressure transducers, flow meters, and power meters. The multiplexer boards are connected to jack panels with grounded and shielded wire to limit electrical interference and drifting in the measured voltages. The jack panels allow for quick connection of instrument outputs and thermocouples to the data acquisition system.

This system, interfacing with HP VEE data acquisition software, allows visual readouts of desired parameters as well as broad data analysis capabilities. Several computations are performed in the data acquisition program, such as calculating mass flux, heat flux, test section inlet quality, and quality change during evaporation or condensation. HP VEE also interfaces easily with Microsoft Excel, which facilitates data recording and analysis.

3.1.7 Calculated Parameters

As mentioned above, the HP VEE data acquisition program performs several computations necessary to carry out experimental procedures. This includes calculating mass flux, heat flux, enthalpies at various locations, and qualities.

Mass flux is determined by simply dividing total mass flow rate (the sum of the liquid and vapor flows) by the test section cross sectional area. In a similar manner, the test section heat flux is calculated by dividing the heat exchanged in the test section by the surface area of the test section.

Several energy balances are used in order to calculate the quality of the two phase refrigerant flow entering the test section and the change in quality during heat exchange experiments. The enthalpy of the subcooled liquid at

the preheater inlet is calculated through the temperature and pressure measurements at that location, with the use of the following equation:

$$h_{sub} = h_l + v_l\left(P_{sub} - P_l\right) \tag{3.1}$$

Internal energy for the subcooled and saturated liquid states is assumed to be equal; however, a small modification is used for the *Pv* term in the enthalpy relation. As can be seen from equation 3.1, the $P_l v_l$ term is subtracted while the $P_{sub} v_l$ term is added. Since in subcooled conditions, v_l very nearly equals v_{sub}, the $P_{sub} v_l$ term is nearly exact.

The vapor line exit enthalpy is superheated at the exit of the compressor, so the enthalpy just prior to mixing is found by knowing the temperature and pressure at that location. When the HP VEE program was written, there was no method available to use property lookup tables or interface directly with programs with that capability, so curve fits are used to find the vapor line exit enthalpy. The curve fits used were generated in Engineering Equation Solver (EES), an f-chart software program developed by S.A. Klein and F.L. Alvarado, with refrigerant property calculation capabilities. This program uses the Martin-Hou equation of state for the property values of R134a.

The test section inlet quality is found by beginning with the equation below, which is an energy balance on the refrigerant line:

$$\dot{m}_{in} h_{TS\_in} = \dot{m}_v h_v + \dot{m}_l h_l + \dot{Q}_{PH} \tag{3.2}$$

where $\dot{m}_{in}$ is the sum of the liquid and vapor mass flow rates, as stated earlier. When the liquid is flowing alone, the vapor term from the compressor is zero, so the total mass flow rate is equal to the liquid mass flow rate. Equation 3.2 is then rearranged as follows:

$$h_{TS\_in} = \frac{\dot{Q}_{PH}}{\dot{m}_l} + h_{sub} \tag{3.3}$$

In the above equation, the test section inlet enthalpy is calculated from the measured preheater power and the enthalpy of the subcooled liquid at the preheater inlet as described above in equation 3.1. Since there is no heat addition from the preheater outlet to the test section inlet, this enthalpy is assumed to be that of the flow entering the test section. This enthalpy is then used to calculate the test section inlet quality through the use of the following equation:

$$x = \frac{h_{TS\_in} - h_l}{h_v - h_l} \tag{3.4}$$

In equation 3.4 above, the saturated liquid and saturated vapor enthalpies are calculated using curve fits from EES.

When the compressor is in use, finding the quality at the test section inlet requires a mixture calculation because the liquid from the pump and vapor from the compressor are now combining to provide the two phase flow to the test section. Equations 3.2 and 3.4 can then be rearranged accordingly to calculate the test section inlet quality.

During heat exchange experiments, a similar energy balance relation is used to calculate the change in quality in the test section.

3.2 Experimental Procedure

This section describes the loop operation and test conditions used for the various adiabatic and heat exchange experiments.

3.2.1 Adiabatic Experiments

Although the goals of this project deal with heat transfer performance of enhanced aluminum microchannels, adiabatic experiments were conducted to help characterize the pressure drop of the two test sections. In addition to a full quality range, subcooled liquid and superheated vapor experiments were conducted for the adiabatic experiments. For two phase experiments, the preheater was used to partially evaporate the flow in order to achieve the desired flow condition. Even though the compressor could be used to supply vapor in conjunction with the liquid line, its use was discontinued in favor of using the liquid line and preheater alone. When the compressor was in use, although it takes less time to establish a certain flow condition, it was not as stable as when the liquid line was used alone. For the adiabatic experiments, the water side of the test sections was completely drained and blown out with compressed air to ensure no extra water was left inside the water jackets.

All two phase experiments were conducted at a test section inlet temperature of 5°C. When a two phase condition exists, the temperature is directly related to the pressure of the flow. Using this principle, the inlet temperature was controlled by adjusting a needle valve located downstream of the test sections to control the pressure of the flow. These experiments were conducted at inlet qualities of 20, 40, 60, and 80%. The mass fluxes used were 50, 100, 150, 200, 300, and 400 kg/m^{2}s. Limitations in the pressure regulating capabilities of the refrigerant loop meant that a maximum quality of only 40% could be achieved for the 400 kg/m^{2}s mass flux experiments.

Subcooled liquid experiments were conducted by using the preheater to heat the liquid entering the test section, but not to the point that it begins to evaporate. If vapor pockets were visible in a sight glass downstream of the test section, the pressure was increased by tightening the needle valve, thus forcing the flow back into subcooled conditions. Typical subcooling for these experiments was 5 to 10°C below saturation. Because properties are more constant with temperature for single phase conditions, it was decided that it was not critical to have inlet temperature set to 5°C for these experiments. Instead, the subcooled liquid entered the test sections at temperatures ranging from 1 to 10°C. The mass fluxes used for subcooled liquid experiments ranged from 70 to 440 kg/m^{2}s, run in increments of 30-40 kg/m^{2}s. Since the values for the individual test conditions were not as rigidly defined as for the two phase experiments, this testing scheme was quicker, and also resulted in a broader range and greater number of data points available for analysis.

Superheated vapor experiments were conducted by using the vapor compressor alone. Similar testing schemes were used for these experiments, but limitations in the cooling capacity of the vapor cooler in the compressor line dictated that the inlet temperatures were between 13 and 17°C. Also, the compressor was not capable of reaching as high of mass fluxes, so the mass flux ranged from 30 to 260 kg/m^{2}s.

3.2.2 Heat Exchange Experiments

Heat transfer experiments are the heart of the work for this project. Evaporation experiments were conducted for two phase conditions, in addition to the subcooled liquid and superheated vapor heating experiments.

For the two phase evaporation experiments, heated water was supplied to the water jackets by the constant temperature bath. As with the two phase adiabatic experiments, the inlet temperature was set at 5°C for all evaporation tests. Mass fluxes used were 100, 150, 200, 300, and 400 kg/m^{2}s, and the inlet qualities were 5, 20, 40, 60, and 80%. This test matrix is similar to the conditions described above, except that the 50 kg/m^{2}s mass flux was eliminated due to instabilities introduced by the heat addition and the 5% inlet quality was added to give data at lower average qualities. As for the adiabatic experiments, a maximum quality of only 60% was attainable at the 400 kg/m^{2}s mass flux. The warm water entered the water jackets at 9 or 10°C, depending on the mass flux. Heat input to the test sections was set at constant values. Although this approach resulted in different heat fluxes delivered to each test section, it allowed direct comparison of the results because the quality change was the same for each test section. Table 3.3 shows the heat input values used with the corresponding quality change values.

Table 3.3: Heat Input and Quality Change Values

G (kg/m2s)	Heat Input (W)	Quality Change
100	100	0.28
150	100	0.19
200	100	0.14
300	150	0.14
400	150	0.11

Subcooled liquid tests were run as described above, but the heat input for these tests was set between 18 and 54 W. For each mass flux, several values of heat input were used to give a broader data range. The water temperature entering the test sections was much higher than for the evaporation experiments, typically between 12 and 20°C. Superheated vapor tests were run in the same manner as described above for the adiabatic experiments. Heat input values, typically between 13 and 60 W, were set according to the same scheme as the subcooled liquid experiments.

Although the main goal of this project is to characterize the heat transfer of enhanced aluminum microchannels during evaporation, limited condensation experiments were run under similar conditions. The purpose of the condensation experiments is to compare with the evaporation results and be able to describe the differences, particularly with regard to the nucleate boiling contribution of the enhanced test section. Condensation experiments were run at mass fluxes of 150 and 300 kg/m^{2}s, inlet qualities of 20, 40, 60, and 80%, and inlet temperatures of 5°C. The water temperatures entering the water jackets were kept as low as possible by using an ice slurry in the constant temperature bath, which gave inlet water temperatures of around 0.5°C. The cooling values for these experiments were the same magnitude, but opposite value, of the heating values used for the same mass fluxes in evaporation.

3.3 Methodology

Pressure gradient and heat transfer are the two parameters we are interested in for this investigation. To compute the pressure gradient, the differential pressure is measured by the data acquisition system. Equations 2.18 and 2.19 are then applied to the raw pressure drop data to adjust for the entrance and exit effects caused by the

microchannel grooves. It should be noted that the maximum change in pressure drop caused by the entrance and exit effects was 2.8%, and the average difference was only 1.4%. After the entrance and exit effects have been accounted for, the pressure gradient is calculated by simply dividing the pressure drop by the test section length. The length of the microchannel grooves for both test sections is 41.91 cm (16.5 in).

Several parameters are measured by the data acquisition system to compute the heat transfer coefficient. To determine the heat flux, the heat transmitted by the water-side is required. This heat input is calculated from the water flow rate measured by the water flow meter, and the temperature change as measured by thermocouple probes inserted into inlet and outlet of the water stream. The equation used to calculate the test section heat input is

$$\dot{Q}_{TS} = \left(r\dot{V}\right)C_p\left(T_i - T_o\right) \tag{3.5}$$

The test section heat flux is then calculated by dividing the heat transfer above by the total surface area of the test sections. The entrance and exit regions are assumed to have the same heat transfer coefficient as the overall flow in the microchannel grooves. The flow in these areas is very turbulent due to the angled entrance and exit required for this type of test section, so the heat transfer will be high in these areas. Therefore, the areas of the entrance and exit of the test sections are added to the surface areas of Table 3.2 to compute the overall heat flux into the test section which will then be used to calculate the overall heat transfer coefficient.

$$h = \frac{\dot{Q}_{TS}}{A_{surf}\left(T_w - T_{ref}\right)} \tag{3.6}$$

Since there are four pairs of wall temperature thermocouples along the length of each test section, the refrigerant temperature must be determined for those locations. Since their axial locations are known, this is accomplished by interpolating between the inlet and outlet temperature readings. The inlet and outlet thermocouples are inserted directly into the entrance and exit holes of the test sections (see Figure 3.6) to ensure accurate measurement of the actual entrance and exit refrigerant temperatures. The wall temperatures are compensated for conduction to find the wall surface temperature at each of the axial locations. The four temperature differences T_w-T_{ref} are then averaged according to the amount of length they cover in the test section. Since the thermocouple probes are spaced equally along the length of the test section and not the length in which refrigerant actually flows, the average turns out the be a weighted average and not a straight average of the thermocouple readings.

Chapter 4. Adiabatic Pressure Drop Results

In this chapter, results for the adiabatic pressure drop experiments will be presented. Experimental results for single phase and two phase pressure drop are discussed and compared to pressure drop correlations discussed in Chapter 2. The Full, Mid, and Tip geometries are used to define the dimensions of the enhanced test section as described in section 3.1.4.

4.1 Single Phase Adiabatic Pressure Drop

In this section, single phase pressure drop results will be presented and discussed. Subcooled liquid and superheated vapor results are presented and compared to pressure drop correlations found in the literature. For the single phase results, the raw pressure drop data is converted to the Darcy friction factor f_D through the use of equation 2.4.

4.1.1 Subcooled Liquid Results

The experimental results for subcooled liquid flow in both test sections are shown in Figure 4.1. This figure also includes the Churchill (1977a) friction factor correlation for a smooth wall tube in order to give a common reference for the data sets. The effect of increased effective mass flux for the three enhanced test section geometry definitions can be seen as an increase in Reynolds number, resulting in a horizontal shift of the same friction factor data set. As can be seen in Figure 4.1, the subcooled liquid data are quite scattered. However, upon closer inspection, it can be seen that the basic test section friction factors group closely with the commonly accepted laminar to turbulent shift near a Reynolds number of 2300.

The friction factor data for the enhanced test section also shows a large amount of scatter. However, when the 'full' dimensions are used, the enhanced test section friction factors appear to group closely with the laminar portion of the Churchill correlation. Therefore, the results shown in Figure 4.1 tend to suggest that the enhanced test section is using the full area during all-liquid flow. This result is somewhat contrary to what was initially expected. Due to the higher density and viscosity of the liquid phase, the grooves were thought to be too narrow and deep for the liquid phase to make full use of their areas.

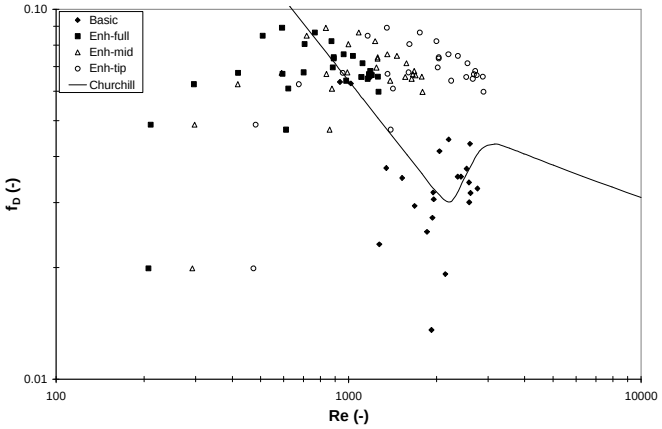

Figure 4.1: Friction Factor vs. Reynolds Number for Adiabatic Subcooled Liquid

The large scatter in the liquid data can be attributed to the relatively small pressure drops recorded for liquid flow. In many cases, the pressure drops were only three to four times the magnitude of the uncertainty of the pressure transducer. Some efforts were made to achieve better resolution at this low range of pressure drops, including the use of a smaller, 0-14 kPa differential pressure transducer. Even though the pressure ports were valved off and equalized when not in use, this pressure transducer was promptly overpressurized and did not last long enough to finish the single phase tests. However, the valves from this smaller capacity pressure transducer were then connected to the standard pressure transducer to allow for quick re-zeroing of the reading throughout each day of testing. Typical drift in this pressure transducer was less than 0.05 kPa when left for several days.

The experimental results were also compared to single phase pressure drop correlations found in the literature and discussed in section 2.2. Figure 4.2 shows the results of these correlations when applied to the basic test section. Several trends are seen in this figure. The Nikuradse (1933) correlation predicts a constant friction factor because it was developed for a fully rough pipe, in which the friction factor does not depend on Reynolds number. The laminar friction factor lines up with the Churchill (1977a) correlation for most of the data points because the Churchill correlation was developed to span the entire range of Reynolds numbers, including the laminar regime. However, in general, none of the correlations appear to accurately predict, or even correlate to a limited degree, the friction factors of the basic test section with liquid flow. The only points that seem to line up adequately occur at higher experimental pressure drops, which could suggest that the error in the lower range of experimental friction factors clouds the overall representation of the data.

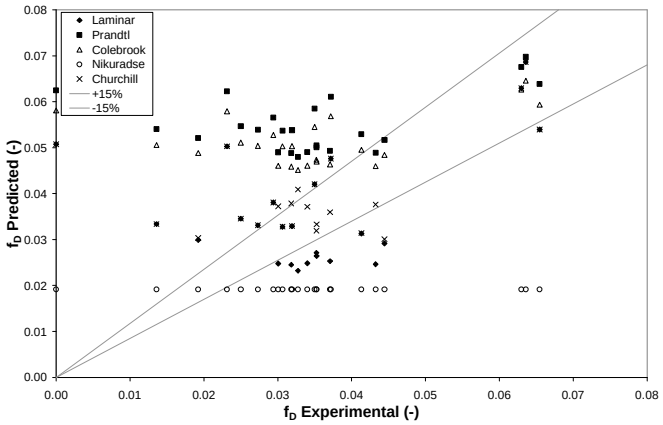

Figure 4.2: Correlation Comparison for Basic Test Section Adiabatic Subcooled Liquid

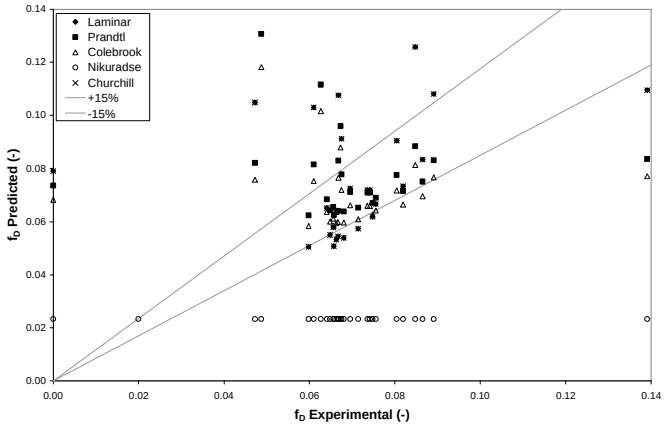

Figure 4.3: Correlation Comparison for Enhanced Test Section Adiabatic Subcooled Liquid—Full Geometry

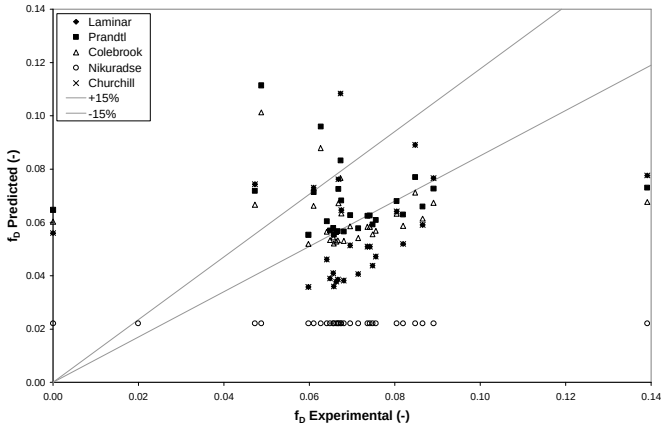

Figure 4.4: Correlation Comparison for Enhanced Test Section Adiabatic Subcooled Liquid—Mid Geometry

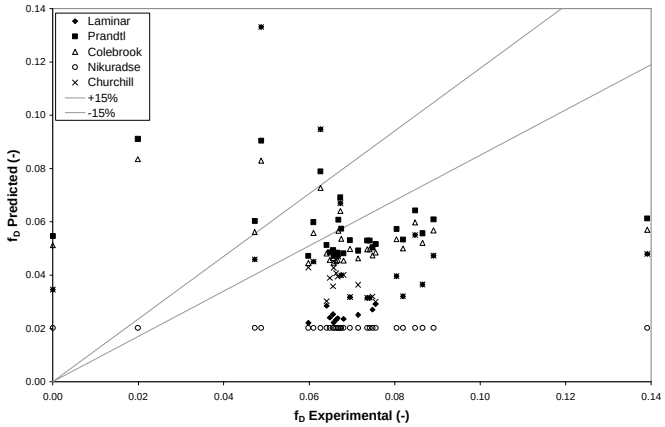

Figure 4.5: Correlation Comparison for Enhanced Test Section Adiabatic Subcooled Liquid—Tip Geometry

The results for the single phase friction factor correlations for the enhanced test section Full, Mid, and Tip geometries can be seen in Figures 4.3, 4.4, and 4.5, respectively.

As with the basic test section, the Nikuradse correlation predicts a constant friction factor and the Churchill correlation matches up with the laminar friction factor for most points. However, for the Tip geometry, the Churchill correlation begins to separate from the laminar friction factor at points where the Reynolds number has passed the laminar to turbulent transition of around Re=2300. When comparing the correlation results for the three enhanced test section geometries, we can see that the effect of changing dimensions results in a systematic shift in the data sets. This behavior is typical of all pressure drop (and heat transfer) correlations, and in this case, is caused by the changing hydraulic diameter and effective mass flux for the different geometries. Overall, none of the correlations are shown to adequately predict the friction factors of the enhanced test section. However, between the three geometries, the best agreement occurs for the Full geometry. Figure 4.3 shows that the correlation results for the Full geometry fall in a close group near the middle of the predicted vs. experimental friction factor plot. As with the experimental data seen in Figure 4.1 above, we come to the conclusion that the subcooled liquid friction factor is best predicted using the Full geometry for the enhanced test section.

4.1.2 Superheated Vapor Results

Figure 4.6 shows the friction factor vs. Reynolds number for the superheated vapor experiments. As can be seen, the Reynolds numbers have passed into the turbulent range, but the data do not line up with, or follow the same slope as, the Churchill (1977a) correlation. The reasons for this behavior are unclear; however, some inferences can be made about the characteristics of the vapor flow. When defining the enhanced test section geometry without the grooves (Tip), the friction factor data line up closely with the data for the basic test section. This result shows that vapor flow in the enhanced test section does not appear to communicate with the grooves, thus acting as if they are not present.

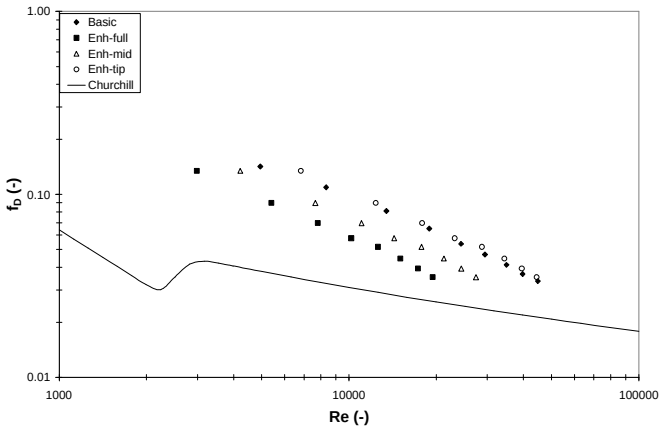

Figure 4.6: Friction Factor vs. Reynolds Number for Adiabatic Superheated Vapor

The correlation results for the basic test section and three enhanced test section geometries are shown in Figures 4.7, 4.8, 4.9, and 4.10, respectively. For the three geometries, the Prandtl (1935), Colebrook (1939), and Churchill (1977a) correlation results are nearly the same. The reason for this agreement is because the Prandtl correlation is made for smooth-walled tubes, and the Colebrook and Churchill correlations were applied to represent a smooth wall with a roughness, ε, of 10^{-6} m. When comparing the three figures for the enhanced test section, there is little variation between the results for the three geometries. Although it is clear that none of the correlations

predict the superheated vapor flow to any degree of accuracy in either test section, the data do fall very nicely on lines of constant slope. This suggests that any of these correlations could possibly be modified to improve their accuracy in predicting the adiabatic superheated vapor friction factors.

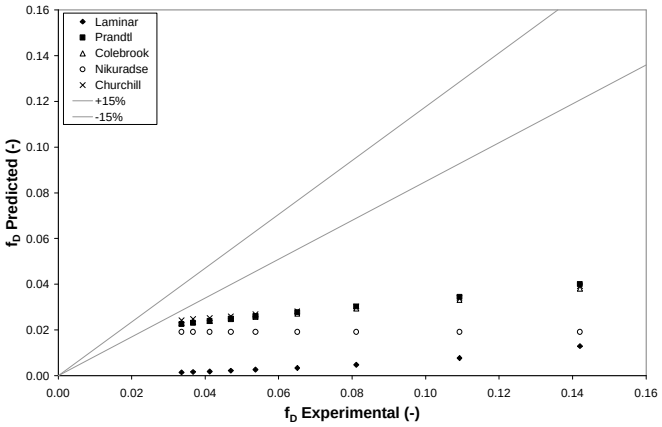

Figure 4.7: Correlation Comparison for Basic Test Section Adiabatic Superheated Vapor

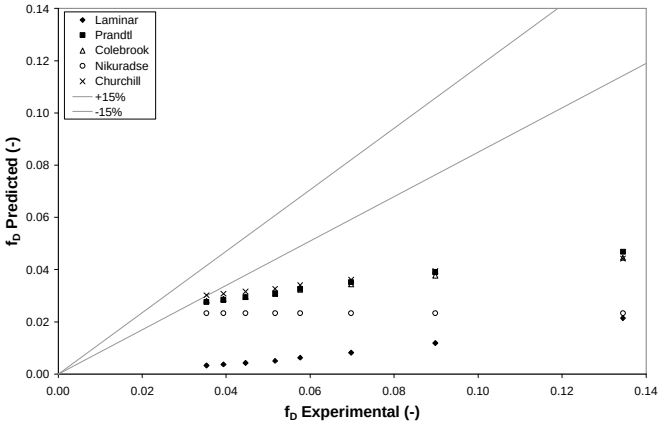

Figure 4.8: Correlation Comparison for Enhanced Test Section Adiabatic Superheated Vapor—Full Geometry

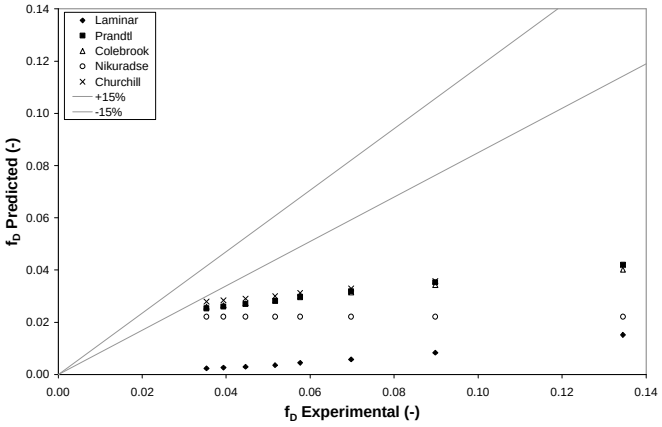

Figure 4.9: Correlation Comparison for Enhanced Test Section Adiabatic Superheated Vapor—Mid Geometry

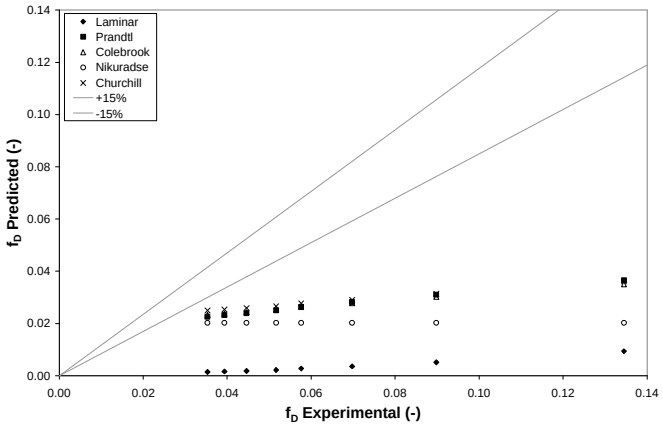

Figure 4.10: Correlation Comparison for Enhanced Test Section Adiabatic Superheated Vapor—Tip Geometry

4.2 Two Phase Adiabatic Pressure Drop

Two phase adiabatic pressure drop results are presented in this section. Since the flow is adiabatic, and therefore, does not change in quality, the accelerational pressure drop from equation 2.13 is not necessary. The entrance and exit effects are characterized by equations 2.18 and 2.19. The experimental data for the basic and enhanced test section are shown in Figures 4.11 and 4.12, respectively. In order to not obscure the data with error bars, a copy of Figure 4.11 is shown in Figure A.1 with error bars included.

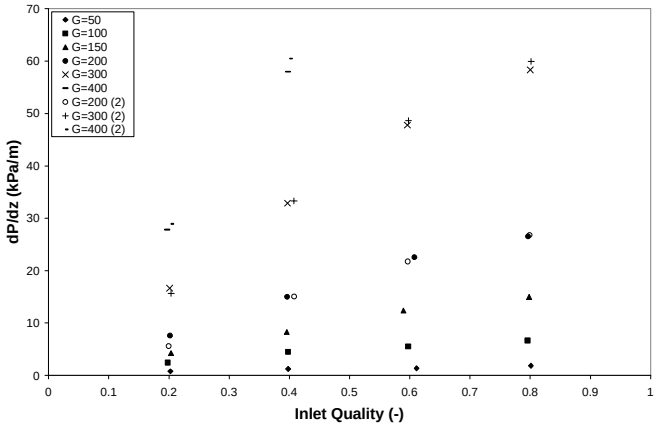

Figure 4.11: Experimental Pressure Gradient vs. Inlet Quality for Basic Test Section Adiabatic Two Phase Flow (Mass Flux, G, in kg/m^2s)

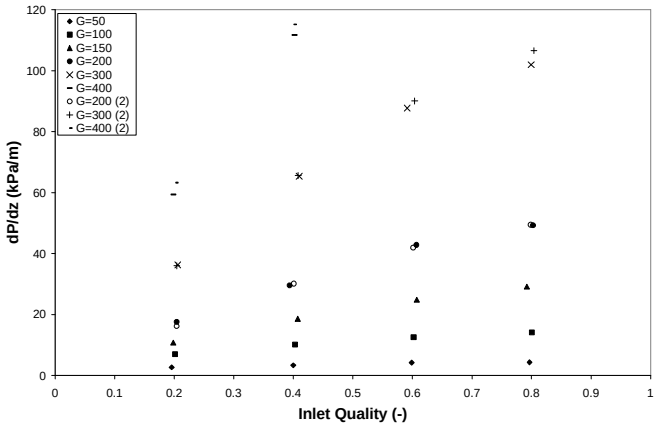

Figure 4.12: Experimental Pressure Gradient vs. Inlet Quality for Enhanced Test Section Adiabatic Two Phase Flow (Mass Flux, G, in kg/m^{2}s)

The data in Figures 4.11 and 4.12 include two pressure drop data sets, taken about three months apart. As can be seen, the two data sets are very close to each other, which demonstrates the repeatability of the pressure drop measurements. For a given mass flux, these figures show that the pressure drop increases linearly with quality until around 70%, where a very slight downward curvature is seen in the data. Although the effect is not very pronounced, this slight change can be attributed to the liquid layer thickness. At low values of quality, the liquid layer is thicker, making the channel seem smaller. As the quality increases, the liquid layer becomes thinner but begins to contain more turbulent waves. This increased turbulence results in an effective roughness which then causes the pressure drop to increase. However, at intermediate qualities of around 70%, this liquid layer is becoming thinner and cannot sustain the same turbulent waves as at a lower quality. This, in turn, decreases the rate at which the pressure gradient increases with quality, which is why the data appear to slightly curve over. This effect is seen more prominently in the pressure drop data from the evaporation tests, which will be discussed in the next chapter.

In order to compare the pressure drop results between the two test sections, a penalty factor was defined. The penalty factor is simply the ratio of the pressure gradient of the enhanced test section to that of the basic test section.

$$PF = \frac{\left(dP/dz\right)_{Enhanced}}{\left(dP/dz\right)_{Basic}} \tag{4.1}$$

Penalty factors are calculated using only the same mass flux and quality conditions.

The penalty factor results are shown in Figure 4.13, in which several interesting trends are observed. Although the penalty factor for a mass flux of G=50 kg/m^{2}s gives an odd fluctuation with quality, the rest of the data show a decreasing penalty factor as the quality is increased. This means that while the pressure drop of the basic test section is increasing with quality, the pressure drop of the enhanced test section is not increasing as quickly. A possible explanation for this result lies in the behavior of the liquid layer in the microgrooves of the enhanced test section. As stated earlier, the liquid layer sustains a certain amount of turbulence which then effects the pressure

drop for a given quality. However, for the enhanced test section, the liquid layer could possibly be 'hidden' in the grooves, causing turbulent waves extending into the middle of the ports to be smaller and not increase the pressure drop proportionately.

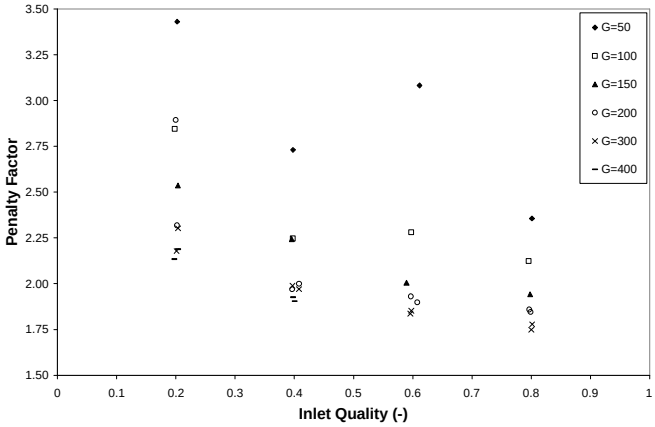

Figure 4.13: Penalty Factor vs. Inlet Quality for Adiabatic Two Phase Tests (Mass Flux, G, in kg/m^{2}s)

Another interesting result seen in the penalty factor data of Figure 4.13 is that the penalty factor actually decreases as the mass flux is increased. As with the quality effects, the increasing mass flux could have a similar effect on the liquid layer. The increased mass flux means that the flow is traveling faster through the channel. This increased velocity will then knock down the liquid waves, thus offering less restriction to the overall flow.

Another interesting observation about the penalty factor is that the data in Figure 4.13 seems to scale with the ratio of hydraulic diameters. The ratio of the basic test section hydraulic diameter to the Full enhanced test section hydraulic diameter is 2.18. The average value of all penalty factor data is 2.20.

4.2.1 Comparison with Large Tube Pressure Drop Correlations

The large tube pressure correlations, described in section 2.3.1, are the Friedel (1979), Jung and Radermacher (1989), and the Souza et al. (1993) correlations. The results for these correlations are shown in Figures 4.14 to 4.17.

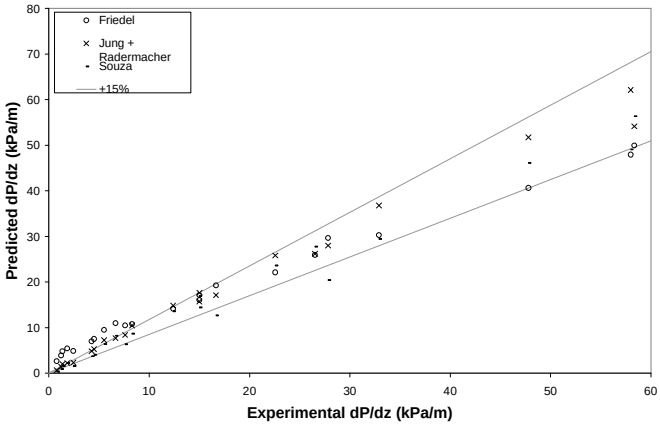

Figure 4.14: Large Tube Pressure Drop Correlation Comparison for Basic Test Section Adiabatic Two Phase Flow

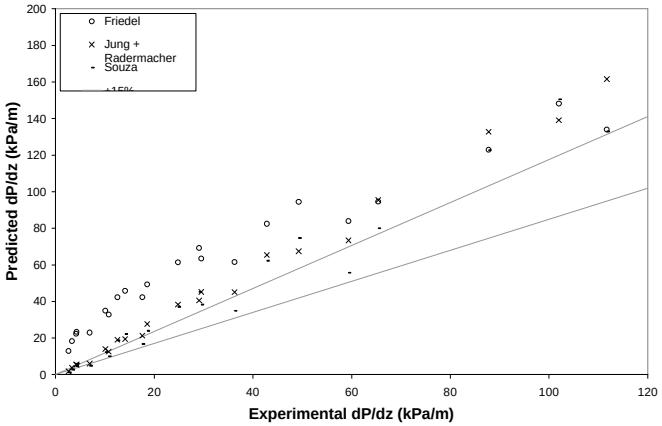

Figure 4.15: Large Tube Pressure Drop Correlation Comparison for Enhanced Test Section Adiabatic Two Phase Flow —Full Geometry

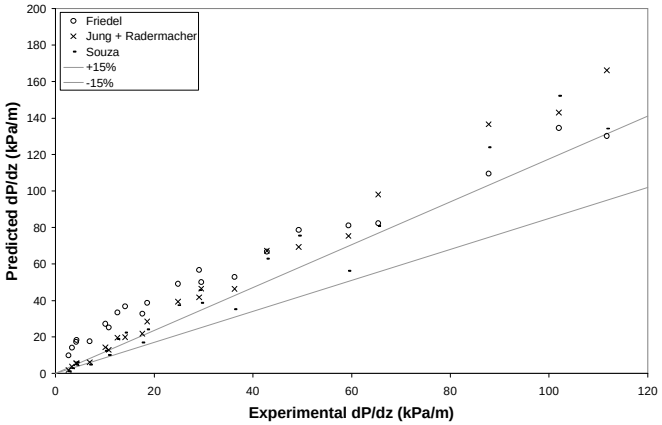

Figure 4.16: Large Tube Pressure Drop Correlation Comparison for Enhanced Test Section Adiabatic Two Phase Flow —Mid Geometry

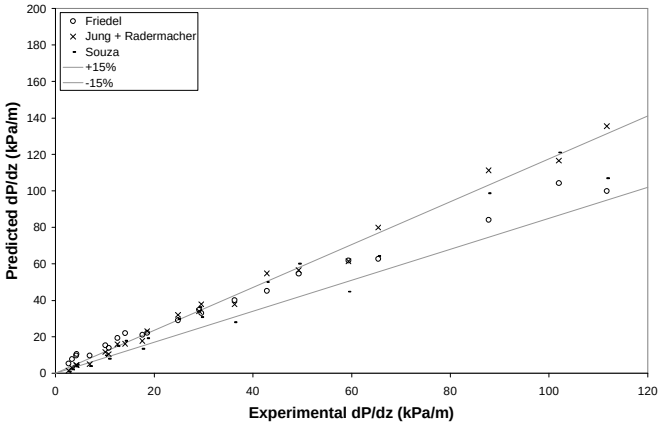

Figure 4.17: Large Tube Pressure Drop Correlation Comparison for Enhanced Test Section Adiabatic Two Phase Flow —Tip Geometry

As can be seen from Figure 4.14, the basic test section is predicted quite well by the large tube pressure drop correlations, especially for higher values of experimental pressure gradient. The higher values of experimental pressure gradient occur at higher mass fluxes, namely mass fluxes of 200, 300, and 400 kg/m^{2}s. Since several of the correlations exhibit this characteristic of performing better at higher mass fluxes, Table 4.1 was made to summarize the errors in the correlations between the low (G=50, 100, and 150 kg/m^{2}s) and high (G=200, 300, and 400 kg/m^{2}s) mass fluxes. For example, the Friedel (1979) correlation shows much better agreement at higher mass fluxes.

Table 4.1: Large Tube Pressure Drop Correlation Average Errors for Low Mass Flux (G=50, 100, and 150 kg/m^{2}s) and High Mass Flux (G=200, 300, and 400 kg/m^{2}s) in Adiabatic Two Phase Flow

	Friedel		***Jung & Radermacher***		***Souza***	
	Low G	***High G***	***Low G***	***High G***	***Low G***	***High G***
Basic	-44.9	0.6	-13.0	-6.9	9.9	10.1
Enh-Full	-71.0	-38.1	-15.9	-27.1	-1.9	-16.3
Enh-Mid	-63.2	-29.3	-18.3	-29.1	-3.5	-17.2
Enh-Tip	-36.0	-3.3	0.3	-13.0	22.1	4.1

In Figures 4.15, 4.16, and 4.17, the differences between the three enhanced test section geometries are shown. When changing the test section geometry from Full to Mid, the correlation results do not shift very much. However, changing the geometry from Mid to Tip results in a large change, and the correlations show the best agreement with experimental data for the Tip geometry. Overall, the Jung and Radermacher (1989) correlation gives the best agreement for the Basic and Enhanced Tip test sections, but the Friedel and Souza (1993) correlations also show good agreement, especially for higher mass fluxes. All three of the large tube correlations are showing reasonable correlation with the experimental data.

4.2.2 Comparison with Microchannel Pressure Drop Correlations

The microchannel pressure drop correlations, as presented in section 2.3.2, include the Yang and Webb (1996), Zhang and Kwon (1999), and the Tran et al. (2000) correlations. The results for these correlations for the various test sections and geometries are shown in Figures 4.18 through 4.20.

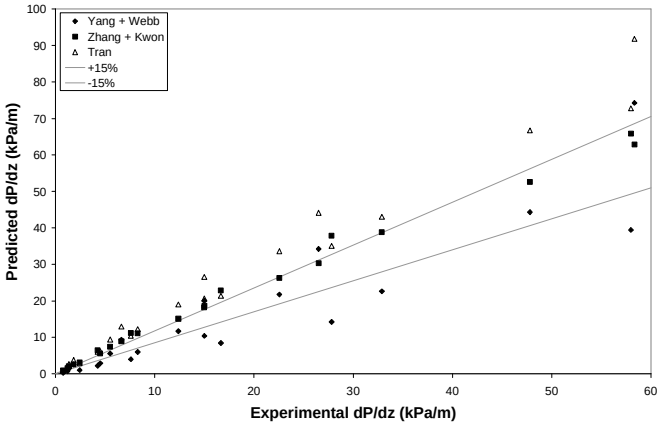

Figure 4.18: Microchannel Pressure Drop Correlation Comparison for Basic Test Section Adiabatic Two Phase Flow

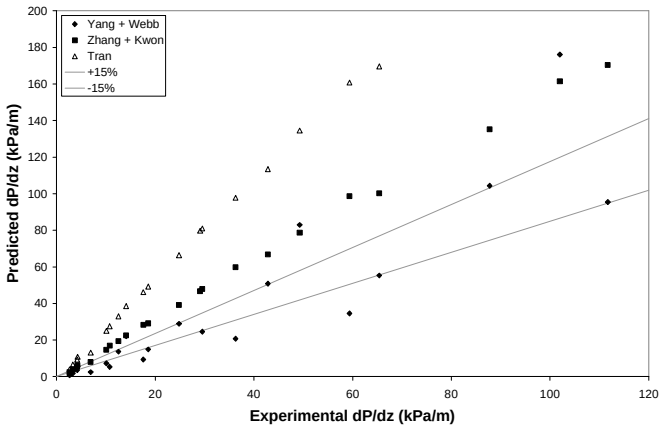

Figure 4.19: Microchannel Pressure Drop Correlation Comparison for Enhanced Test Section Adiabatic Two Phase Flow —Full Geometry

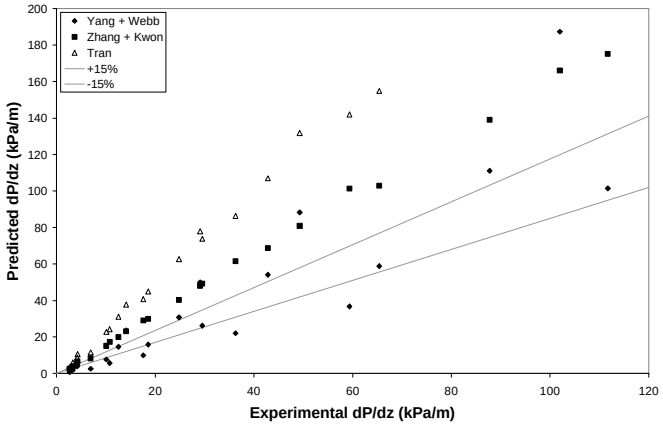

Figure 4.20: Microchannel Pressure Drop Correlation Comparison for Enhanced Test Section Adiabatic Two Phase Flow—Mid Geometry

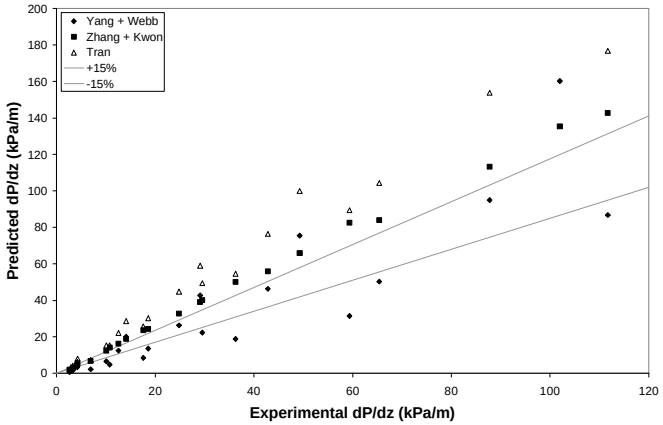

Figure 4.21: Microchannel Pressure Drop Correlation Comparison for Enhanced Test Section Adiabatic Two Phase Flow —Tip Geometry

When reviewing the figures above, it becomes clear that none of the microchannel pressure drop correlations predict either of the test sections to an acceptable degree of accuracy. Overall, when changing the enhanced test section geometry from Full to Mid to Tip, the correlations systematically move closer to the ideal 1:1 ratio with respect to the experimental pressure gradients. This is the same general trend observed for the large tube correlations discussed in the previous section. Of the three geometries, it is clear that the Tip geometry works best in the correlations.

Although the microchannel correlations do not predict the pressure drop in the test sections, they do seem to be able to correlate the pressure drop well, as evidenced by the results falling on straight lines in the figures above. The Yang and Webb and Zhang and Kwon correlations are a good example of this. In particular, when looking at the Full and Mid enhanced test section geometries for these two correlations, we see the data line up very nicely on straight lines, meaning that those correlations could be modified to predict the pressure drop of the enhanced test section.

Table 4.2: Microchannel Pressure Drop Correlation Average Errors for Low Mass Flux (G=50, 100, and 150 kg/m^{2}s) and High Mass Flux (G=200, 300, and 400 kg/m^{2}s) in Adiabatic Two Phase Flow

	Yang & Webb		***Zhang & Kwon***		***Tran***	
	Low G	***High G***	***Low G***	***High G***	***Low G***	***High G***
Basic	39.2	35.5	-23.9	-18.4	-34.3	-28.9
Enh-Full	51.3	18.1	-27.3	-36.6	-56.7	-62.2
Enh-Mid	42.1	10.9	-29.3	-38.3	-53.1	-59.0
Enh-Tip	66.2	29.7	-13.2	-24.3	-31.2	-39.8

As discussed earlier, both sets of pressure drop correlations work best for the Tip geometry in the enhanced test section. In fact, when comparing the graphical and tabular results presented for the Full and Mid geometries, there is only a slight difference between the two. However, when the Tip geometry is used in most cases, there is a very noticeable improvement in the correlation agreement. Coincidentally, changing to the Tip geometry is when the hydraulic diameter increases to a value greater than 1 mm. In addition, the correlations generally work well for the basic test section, which has a hydraulic diameter of 1.66 mm. This suggests that the pressure drop correlations seem to have a marked improvement in agreement with experimental data when the hydraulic diameter passes an observed ‘critical’ value of around 1 mm.

Chapter 5. Heat Transfer Results

In this chapter, results for the heat transfer experiments will be presented. Experimental results for single phase heat transfer are discussed and compared to heat transfer correlations discussed in Chapter 2. For the two phase experiments, both pressure drop and heat transfer results will be presented and compared to the appropriate correlations. The Full, Mid, and Tip geometries are used to define the dimensions of the enhanced test section as described in section 3.1.4.

5.1 Single Phase Heat Transfer

In this section, single phase heat transfer results will be presented. Subcooled liquid and superheated vapor experimental results are compared against heat transfer correlations discussed in section 2.4 of the Literature Review. For single phase flow, the experimental heat transfer coefficients are expressed in terms of the non-dimensional Nusselt number.

$$Nu = \frac{hD_h}{k} \tag{5.1}$$

5.1.1 Subcooled Liquid Results

The experimental Nusselt numbers for subcooled liquid, plotted against Reynolds number, are shown in Figure 5.1. The data in the figure appear to have several data points at each Reynolds number, which is because several heating values were used for each flow condition. The data show the general trend of having an increasing Nusselt number as the Reynolds number is increased. The effect of changing the enhanced test section geometry from Full to Tip is characterized by an increase in Reynolds number because the cross sectional area becomes smaller (increasing the effective mass flux) and the hydraulic diameter increases. The Nusselt number also increases because the surface area decreases, causing the heat transfer coefficient to increase.

The enhanced test section Full geometry data results in a tightly-packed set well within the laminar flow range, and the experimental Nusselt numbers show reasonable agreement with theoretical constant laminar Nusselt numbers toward the higher Reynolds numbers of that group. Table 5.1 summarizes the theoretical constant Nusselt numbers for laminar flow. The majority of the Mid geometry data also fall in the range of theoretical Nusselt numbers for laminar flow. Close inspection of the Basic test section data show a slightly increasing Nusselt number, with values between 3.7 and 5.5 for Reynolds numbers below 2300. The Tip geometry covers a broad range of experimental Nusselt numbers, and does not show reasonable agreement with theoretical Nusselt numbers.

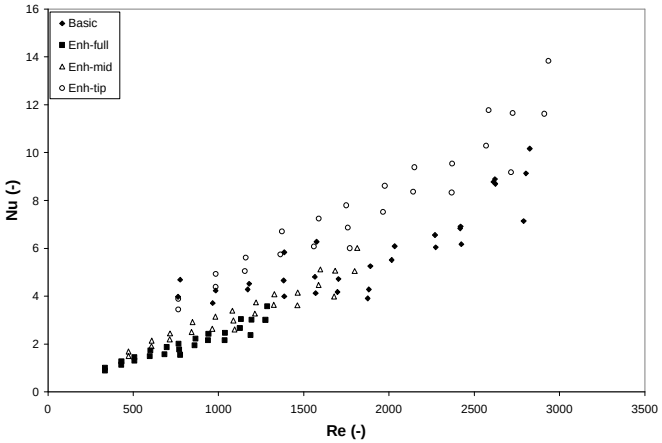

Figure 5.1: Nusselt Number vs. Reynolds Number for Heated Subcooled Liquid Flow

Table 5.1: Theoretical Laminar Flow Nusselt Numbers

		Enhanced		
	Basic	***Full***	***Mid***	***Tip***
Shah & London (1978) Rectangular Duct, Eq. 2.47	4.184	3.85	4.274	4.882
Incropera & Dewitt (1996) Constant Heat Flux			4.36	
Incropera & Dewitt (1996) Constant Surface Temperature			3.66	

The results of the single phase heat transfer correlations for the basic and enhanced test sections are shown in Figures 5.2 through 5.5. For the basic test section results, a large amount of variation is seen in the predictions of the four correlations. The Churchill (1977b) correlation appears to predict the experimental data at the very lowest values of experimental Nusselt numbers. Although it does not do as well as the Churchill correlation, the Gnielinski (1976) correlation also shows limited agreement at its lower range of experimental Nusselt numbers.

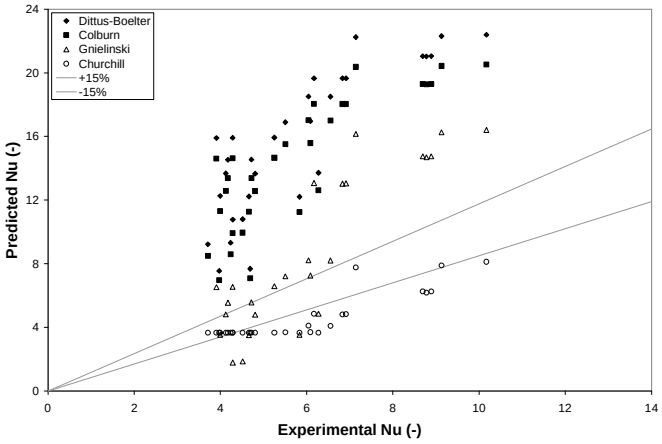

Figure 5.2: Single Phase Heat Transfer Correlation Comparison for Basic Test Section Heated Liquid Flow

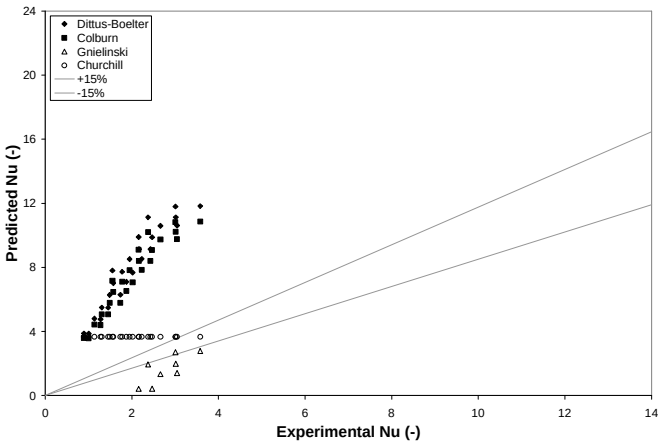

Figure 5.3: Single Phase Heat Transfer Correlation Comparison for Enhanced Test Section Heated Liquid Flow—Full Geometry

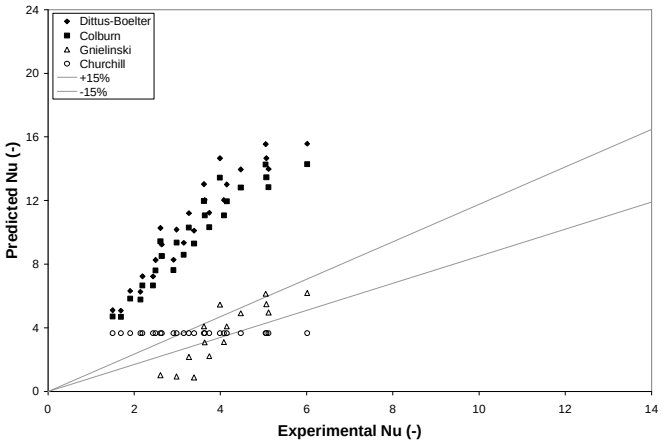

Figure 5.4: Single Phase Heat Transfer Correlation Comparison for Enhanced Test Section Heated Liquid Flow—Mid Geometry

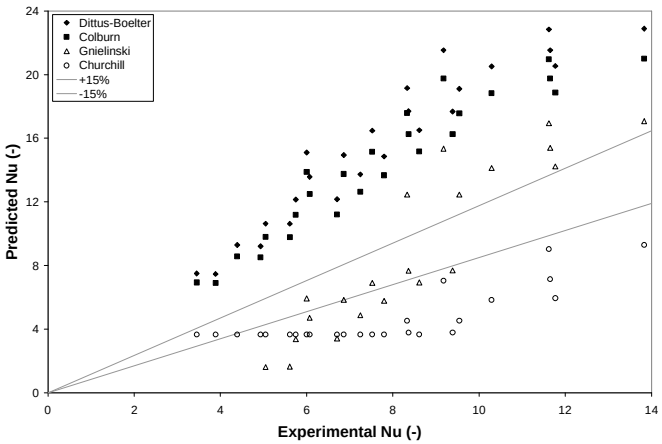

Figure 5.5: Single Phase Heat Transfer Correlation Comparison for Enhanced Test Section Heated Liquid Flow—Tip Geometry

The correlation results for the enhanced test section Full, Mid, and Tip geometries do not give acceptable agreement with experimental data. As discussed earlier, changing the channel geometry results in both horizontal and vertical shifts in the data sets. The only correlation to even limited agreement with experimental data is the Gnielinski correlation when applied to the Mid geometry, and only for higher values of experimental Nusselt numbers. When applied to the Tip geometry the Gnielinski correlation has some points that fall within acceptable limits, where the correlation results go from underpredicting at low experimental Nusselt numbers to overpredicting at higher experimental Nusselt numbers. Although no reasonable agreement is realized for the Dittus-Boelter and Colburn equations, they do show a direct relationship with experimental data for the Full and Mid geometries, which suggests that they could be modified to improve their accuracy.

5.1.2 Superheated Vapor Results

The experimental results for heated superheated vapor flow are shown in Figure 5.6 below.

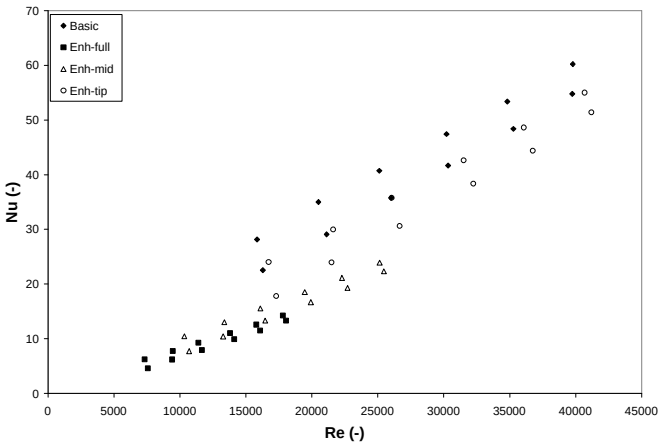

Figure 5.6: Nusselt Number vs. Reynolds Number for Heated Superheated Vapor Flow

The superheated vapor heat transfer data show the same trends for both test sections, which includes an increasing Nusselt number as Reynolds number is increased. When looking at the enhanced test section Full and Mid geometries, there is little difference in results, shown as a slight increase in both Nusselt number and Reynolds number. However, changing to the Tip geometry results in a large change, and the results seem to match up well with the experimental results for the basic test section. Even though these are heat transfer results, this similarity between the basic test section and enhanced Tip geometry is the same as seen before in the pressure drop results for adiabatic flow of superheated vapor.

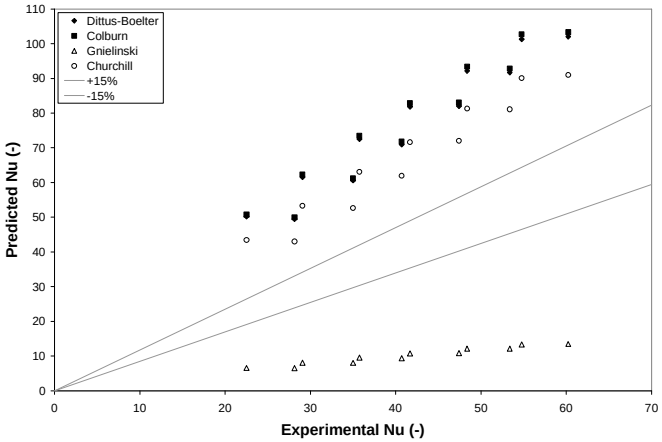

Figure 5.7: Single Phase Heat Transfer Correlation Comparison for Basic Test Section Heated Vapor Flow

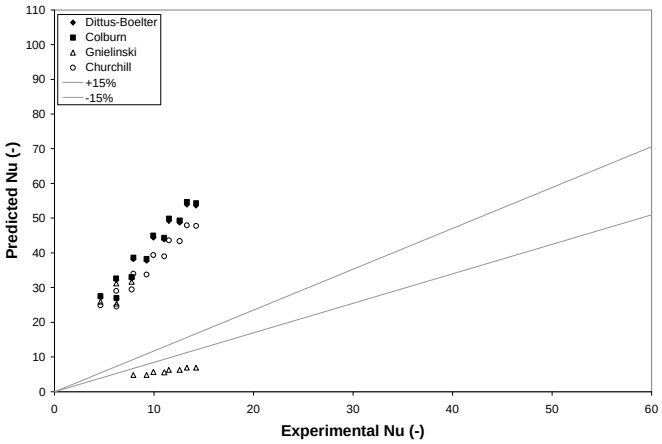

Figure 5.8: Single Phase Heat Transfer Correlation Comparison for Enhanced Test Section Heated Vapor Flow—Full Geometry

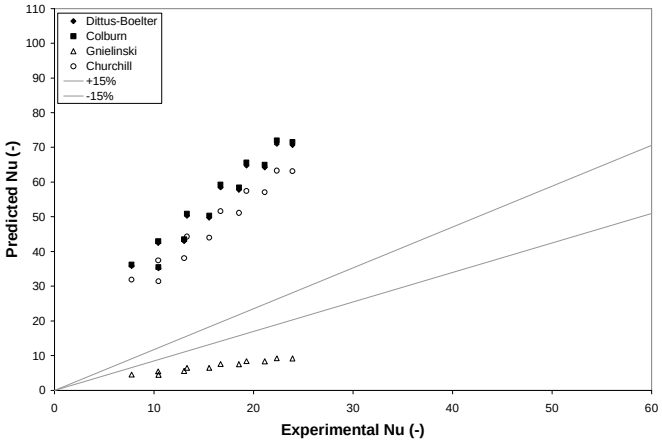

Figure 5.9: Single Phase Heat Transfer Correlation Comparison for Enhanced Test Section Heated Vapor Flow—Mid Geometry

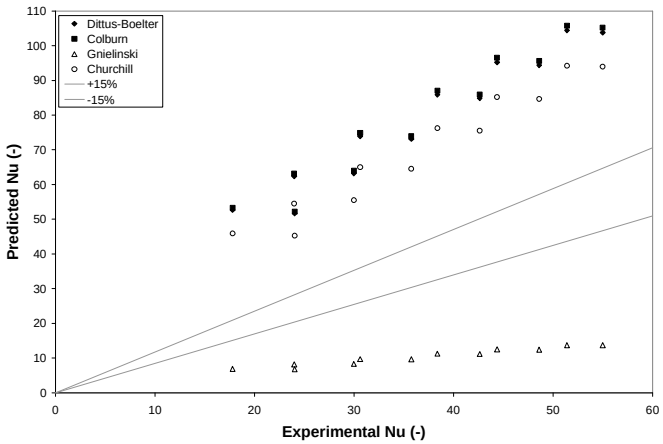

Figure 5.10: Single Phase Heat Transfer Correlation Comparison for Enhanced Test Section Heated Vapor Flow—Tip Geometry

Figures 5.7 through 5.10 show the single phase heat transfer correlation comparisons for the basic and enhanced test section geometries. As can be seen from these figures, none of the correlations come close to predicting any test section or geometry to any acceptable degree of accuracy. Contrary to what was seen for the liquid results from the previous section, no data points even lie in the ±15% range. Even though they cannot predict the experimental results, the correlations appear to be able to correlate the results. Since the data for all four correlations fall on straight lines in the figures above, they could be modified to adequately predict the experimental results. Another interesting point is the relative differences between these correlations when applied to these correlations, as they are all considered to predict experimental results quite well.

5.2 Two Phase Evaporation Heat Transfer

In this section, two phase evaporation results will be presented. In addition to the heat transfer results and comparison with heat transfer correlations, the pressure drop data will also be discussed and compared to pressure drop correlations. Please refer to Table 3.3 for the heat input and quality change values used for the two phase experiments.

5.2.1 Evaporation Pressure Drop Results

The experimental pressure drop results for the evaporation tests for the basic and enhanced test section are shown in Figures 5.11 and 5.12, respectively. Equation 2.13 is used to account for the accelerational pressure gradient, which changed the results by 2.0 to 6.5%. A copy of Figure 5.12 is shown in Figure A.2 to demonstrate the error in pressure drop measurements and to show the quality change ranges for each point (see Table 3.3).

A few key observations can be obtained from the figures below. As seen for adiabatic two phase flow, the pressure gradient increases linearly with quality until an intermediate quality of around 70% is reached. At that point, the pressure gradient begins to increase at a lower rate, and in some cases, remain constant. Although this effect was seen in the adiabatic two phase pressure drop, it is more pronounced for these data sets because the outlet quality reaches higher values, giving data points at average qualities near 90%. The reason for this phenomenon lies in the characteristics of the liquid layer. At higher qualities, it becomes thinner and its apparent roughness is minimized due to its reduced ability to sustain turbulent waves. Although it is an expected result, another trend seen

in the data is an increased pressure gradient as the mass flux is increased. The physical explanations of these trends are the same as those discussed for adiabatic two phase pressure drop in section 4.2.

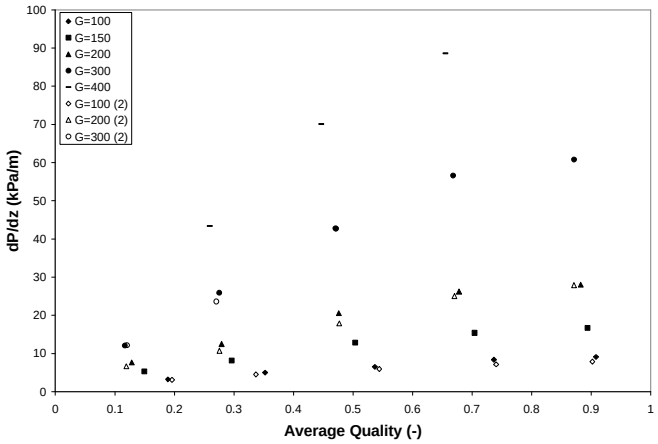

Figure 5.11: Experimental Pressure Gradient vs. Average Quality for Basic Test Section Two Phase Flow in Evaporation (Mass Flux, G, in kg/m^{2}s)

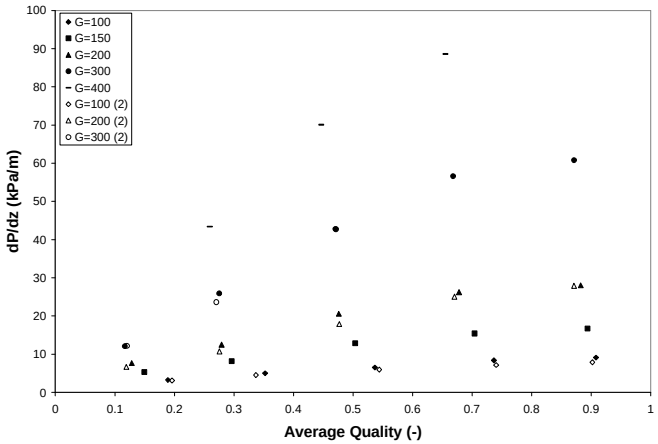

Figure 5.12: Experimental Pressure Gradient vs. Average Quality for Enhanced Test Section Two Phase Flow in Evaporation (Mass Flux, G, in kg/m^{2}s)

The penalty factor, as defined previously, is used to compare the pressure gradient data between the two test sections. The penalty factor data is shown in Figure 5.13. Although there is more data shown in this figure than for the adiabatic two phase penalty factor, the trends are the same. Namely, the penalty factor decreases with mass flux and quality. The physical interpretations of these effects are the same as discussed earlier for adiabatic two phase flow.

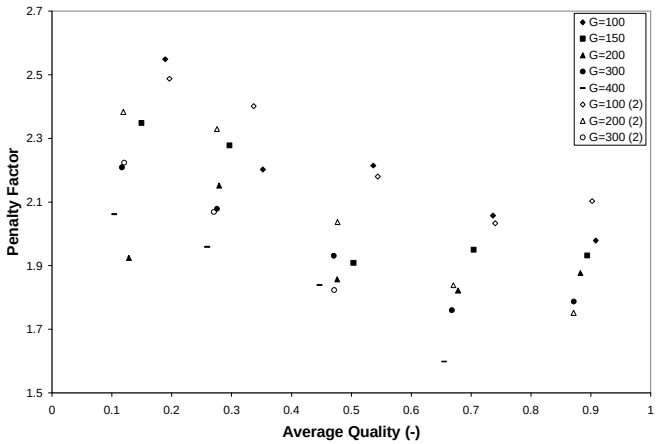

Figure 5.13: Penalty Factor vs. Average Quality for Two Phase Evaporation Tests (Mass Flux, G, in kg/m^{2}s)

In addition to the experimental pressure drop results for the evaporation tests, the pressure drop correlations were also applied to the data. The correlations are the same set as used in the previous chapter. In order to use the correlations for a phase change condition, equation 2.15 is used to integrate the two phase pressure drop multiplier over the range of quality change. Figures 5.14 through 5.17 show the results for the large tube correlations. As can be seen in Figure 5.14, the pressure gradient of the basic test section is predicted to a reasonable degree of accuracy by all three large tube correlations, with the Jung and Radermacher (1989) correlation giving the best agreement with experimental data. In fact, the Jung and Radermacher correlation also gives the best overall agreement for the three enhanced test section geometries. When comparing to the results in Figure 4.14, the large tube correlations tend to underpredict the evaporative pressure gradients more than for adiabatic flow, where much of the data fell within the ±15% range.

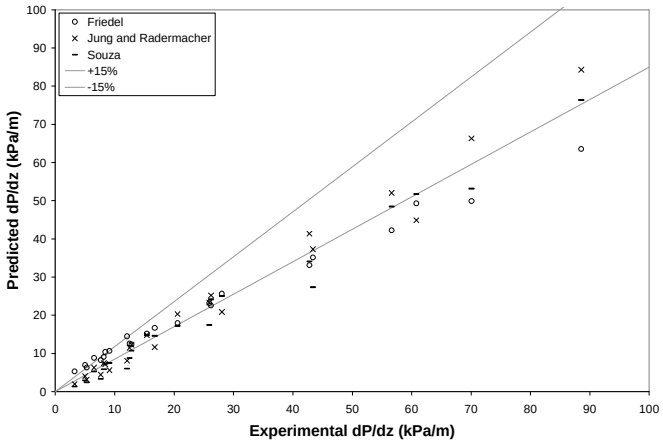

Figure 5.14: Large Tube Pressure Drop Correlation Comparison for Basic Test Section Evaporative Two Phase Flow

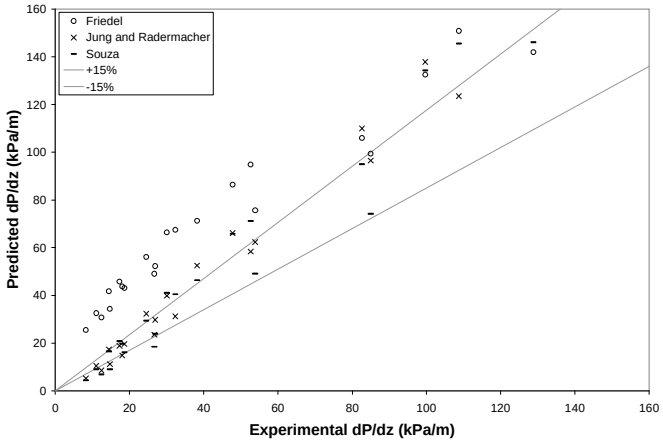

Figure 5.15: Large Tube Pressure Drop Correlation Comparison for Enhanced Test Section Evaporative Two Phase Flow—Full Geometry

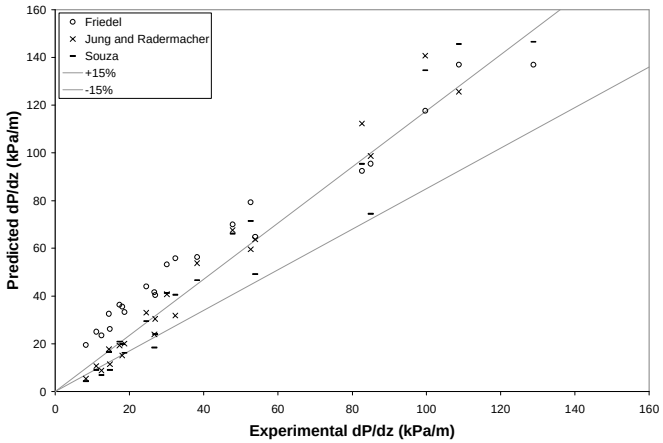

Figure 5.16: Large Tube Pressure Drop Correlation Comparison for Enhanced Test Section Evaporative Two Phase Flow—Mid Geometry

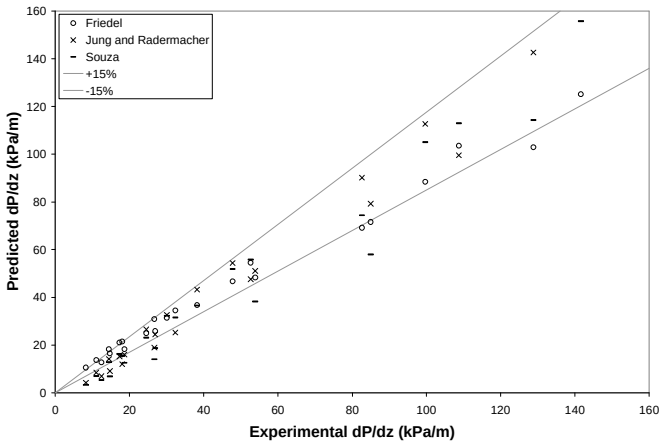

Figure 5.17: Large Tube Pressure Drop Correlation Comparison for Enhanced Test Section Evaporative Two Phase Flow —Tip Geometry

The results in Figures 5.15, 5.16, and 5.17 show the correlations applied to the enhanced test section Full, Mid, and Tip geometries, respectively. Each change in geometry causes the correlation results to fall closer to the ideal 1:1 prediction ratio for the graphs above. Obviously, the results from Figure 5.17 show that the Tip geometry results in the best prediction of experimental pressure gradient for the large tube correlations, where most of the data points fall within ±15% of the experimental data. It should be noted that the Jung and Radermacher and Souza correlations also give excellent agreement for the Full and Mid geometries. Table 5.2 summarizes the average prediction errors for all pressure drop correlations. Since no significant difference was detected between low and high mass fluxes, the overall errors are given in the table.

Table 5.2: Pressure Drop Correlation Average Errors for Evaporative Two Phase Flow

	Yang & Webb	***Zhang & Kwon***	***Tran***	***Friedel***	***Jung & Radermacher***	***Souza***
Basic	82.9	-2.3	-15.6	-2.7	21.4	41.7
Enh-Full	54.1	-23.8	-55.1	-47.9	-5.7	3.3
Enh-Mid	46.9	-25.4	-51.1	-37.5	-7.6	3.2
Enh-Tip	77.9	-7.0	-27.0	-4.8	15.8	33.1

Figures 5.18 through 5.21 show the results for the microchannel pressure drop correlations. For the basic test section, Figure 5.18 shows that the Zhang and Kwon (1999) correlation gives excellent agreement with experimental data, and the Tran et al. (2000) correlation also gives good agreement. In figures 5.19, 5.20, and 5.21, the microchannel pressure drop correlation results are presented for the enhanced test section Full, Mid, and Tip geometries. As with the adiabatic pressure drop, the microchannel correlations do not predict the enhanced geometries very well overall. However, the Zhang and Kwon correlation does an excellent job predicting the experimental pressure gradient data when applied to the Tip geometry. As described in the previous chapter, the correlations work best on the Tip geometry because it is apparently making use of the grooves as a place to 'hide' the liquid layer so that its roughness does not contribute as much to increasing the overall pressure drop.

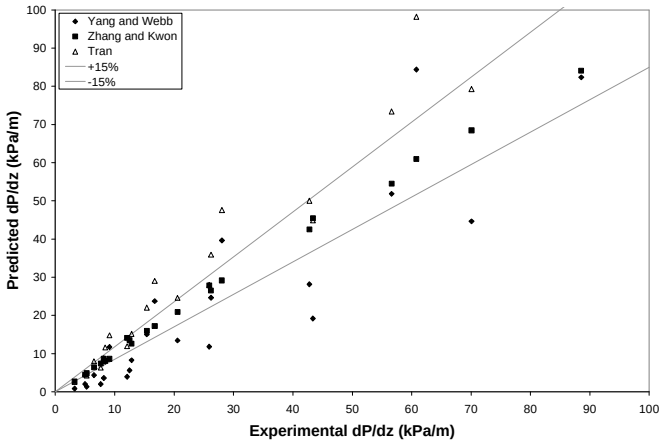

Figure 5.18: Microchannel Pressure Drop Correlation Comparison for Basic Test Section Evaporative Two Phase Flow

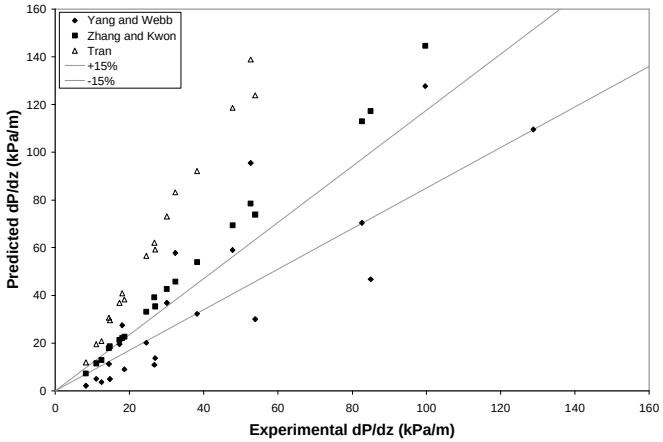

Figure 5.19: Microchannel Pressure Drop Correlation Comparison for Enhanced Test Section Evaporative Two Phase Flow —Full Geometry

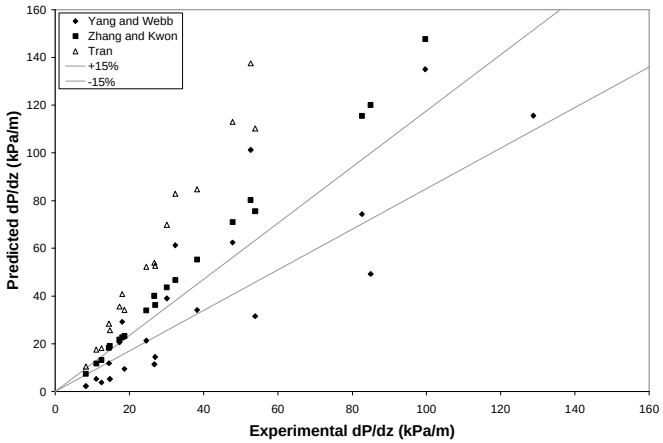

Figure 5.20: Microchannel Pressure Drop Correlation Comparison for Enhanced Test Section Evaporative Two Phase Flow—Mid Geometry

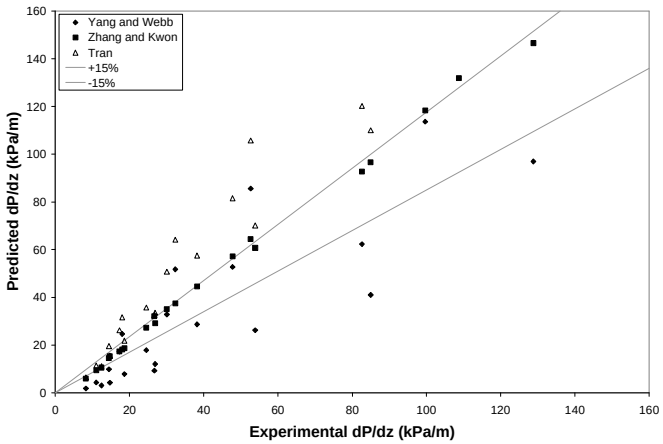

Figure 5.21: Microchannel Pressure Drop Correlation Comparison for Enhanced Test Section Evaporative Two Phase Flow —Tip Geometry

5.2.2 Evaporation Heat Transfer Results

The goals of this project center around exploring the heat transfer characteristics of the enhanced test section geometry. In this section, the evaporation heat transfer results will be presented and the thermo-physical mechanisms behind the experimental observations will be explained, as well as comparing the experimental results to heat transfer correlations found in the literature. For two phase heat transfer, the results will be expressed in terms of the heat transfer coefficient instead of using the non-dimensional Nusselt number because that is the method commonly used in the literature.

Figures 5.22 and 5.23 show the experimental heat transfer results for the basic test section and enhanced test section Full geometry, respectively.

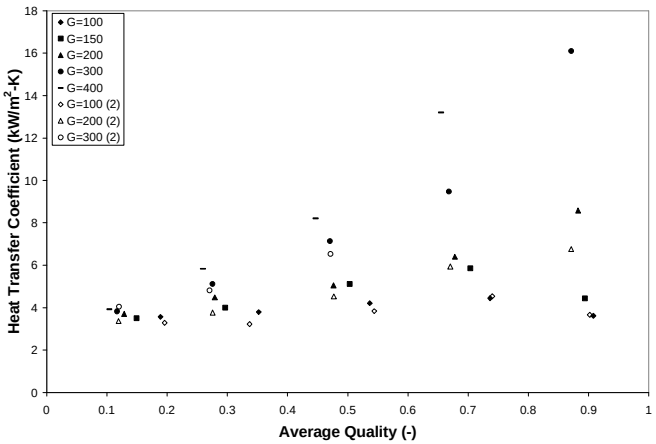

Figure 5.22: Experimental Heat Transfer Coefficient vs. Average Quality for Basic Test Section Evaporative Two Phase Flow (Mass Flux, G, in kg/m^{2}s)

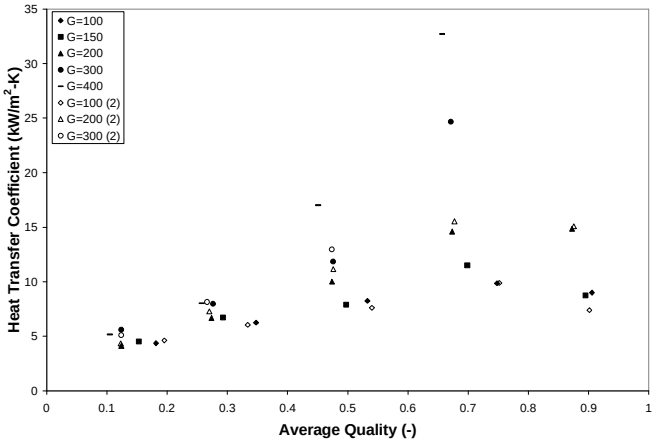

Figure 5.23: Experimental Heat Transfer Coefficient vs. Average Quality for Enhanced Test Section Full Geometry Evaporative Two Phase Flow (Mass Flux, G, in kg/m^{2}s)

Two data sets are shown in Figures 5.22 and 5.23. These data sets were taken months apart and show the repeatability in the experimental heat transfer data. To show the relative uncertainty in heat transfer measurements in the two test sections, Figures A.3 and A.4 were made. It should be noted that there are a few points in these figures that could be susceptible to increased error due to a smaller average temperature difference. Since the

temperature difference is in the denominator of equation 3.6, it makes the heat transfer coefficient become larger. Those points with increased error in the basic test section are G=300 kg/m^{2}s, x_{avg}=0.87 and G=400 kg/m^{2}s, x_{avg}=0.65, and for the enhanced test section are G=300 kg/m^{2}s, x_{avg}=0.67 and G=400 kg/m^{2}s, x_{avg}=0.66.

As can be seen from the data, the heat transfer coefficient increases with quality until an intermediate value of around 70%. At qualities greater than this value, the heat transfer coefficients begin to decrease for most mass flux cases. This is also the same quality range that the pressure drop data began to decrease. Again, the reason for this behavior can be explained by understanding the characteristics of the liquid layer. Turbulent motion of the liquid layer enhances its heat transfer, which can be offset by the conduction resistance through the liquid thickness. At low qualities, the liquid layer is thicker, but still rather turbulent. As the quality is increased the liquid layer becomes thinner while still maintaining turbulence, which results in an increasing heat transfer coefficient. However, for higher qualities, the liquid layer has become very thin. Although the conduction resistance is now greatly reduced, the liquid layer is now too thin to sustain the large turbulent waves that enhance the heat transfer at lower qualities. Consequently, the heat transfer coefficient is reduced because the liquid layer begins to be dominated by conduction through its thickness rather than convection from its turbulent motion.

In addition, the heat transfer coefficient increases as the mass flux is increased. This result can be explained by an expected increase in turbulence at higher mass fluxes.

In order to compare the heat transfer coefficients between the two test sections, two enhancement factors were defined to illustrate the changes in the enhanced test section heat transfer. The enhancement factors are calculated for the same experimental conditions only. The first enhancement factor, *EF1*, is the ratio of the heat transfer coefficients between the two test sections.

$$EF1 = \frac{h_{Enhanced}}{h_{Basic}} \tag{5.2}$$

The second enhancement factor, *EF2*, is the ratio of the *hA* values of the two test sections.

$$EF2 = \frac{(hA)_{Enhanced}}{(hA)_{Basic}} \tag{5.3}$$

The surface areas used in the enhancement factor calculations for the enhanced test section are from the Full geometry. Figures 5.24 and 5.25 show the first and second enhancement factors, respectively.

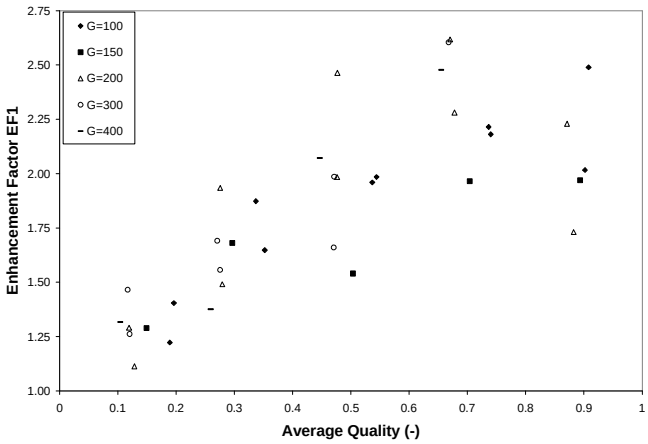

Figure 5.24: First Enhancement Factor (EF1) vs. Average Quality for Two Phase Evaporation Tests (Mass Flux, G, in kg/m^2s)

Because all of the data lie above a value of unity, The data in Figure 5.24 show a definite increase in heat transfer coefficient for the enhanced test section. In general, the enhancement factor increases as the quality is increased. This result means that, while both test sections are experiencing increases in heat transfer coefficient for low- to mid-range qualities, the enhanced test section is increasing at a faster rate than the basic test section. A possible explanation for this key phenomenon lies in the nature of the grooves of the enhanced test section. Since the liquid flow seems to be filling up the microgrooves, the heat transfer of the enhanced test section is increased, but further enhancement can be achieved through the turbulence effects constantly moving the liquid flow within and around the fins and grooves. Because of their small size and limited flow capabilities, an increased nucleate boiling contribution from the grooves also appears to be enhancing the heat transfer of the enhanced test section. Although the data seem to be rather scattered between the various mass flux conditions, the first enhancement factor is also showing increased values at higher mass fluxes. This result is explained through increased turbulence at higher mass fluxes.

Figure 5.25 shows the second enhancement factor, *EF2*, vs. average quality for the evaporation experiments. Although the areas used in this figure are for the Full geometry of the enhanced test section, the same characteristics are found for the Mid and Tip geometries. Since *EF2* is basically the same as *EF1*, but modified by a constant multiplier equal to the area ratios, the results shown in Figure 5.25 can be modified by constant values to yield the results for the Mid and Tip geometries.

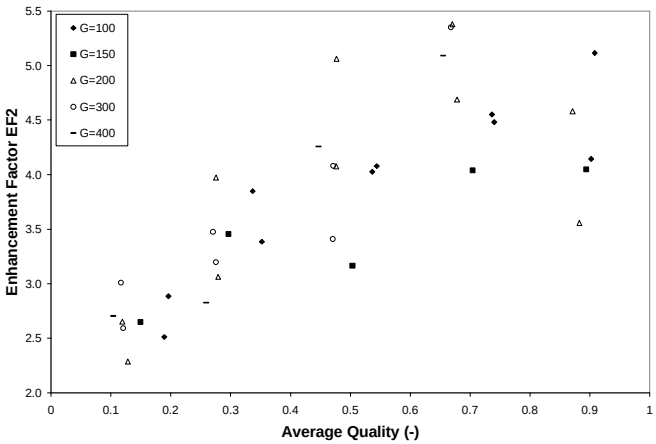

Figure 5.25: Second Enhancement Factor (EF2) vs. Average Quality for Two Phase Evaporation Tests (Mass Flux, G, in kg/m^{2}s)

The second enhancement factor was defined as a way to compare the heat transfer capacity between the two test sections. While the first enhancement factor showed that the heat transfer coefficient increased by an average of a factor of two, the second enhancement factor shows that the enhanced test section achieves almost four times the heat transfer capacity of the basic test section. The increased effects at higher mass fluxes are more visible in the data for the second enhancement factor.

The heat transfer data is also compared to correlations to help predict and explain the differences between the two test sections. The heat transfer correlations used are discussed in section 2.5 of the Literature Review. The results of these correlations are shown in Figures 5.26 through 5.29.

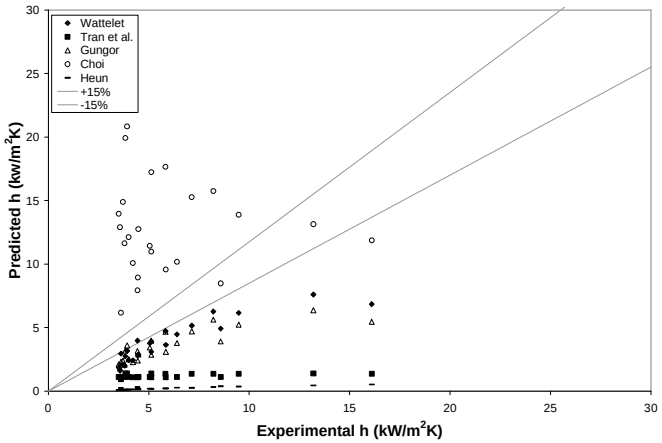

Figure 5.26: Heat Transfer Correlation Comparison for Basic Test Section in Evaporation

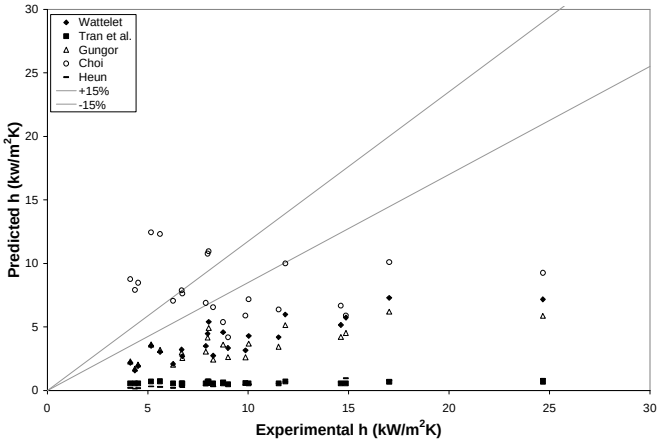

Figure 5.27: Heat Transfer Correlation Comparison for Enhanced Test Section in Evaporation—Full Geometry

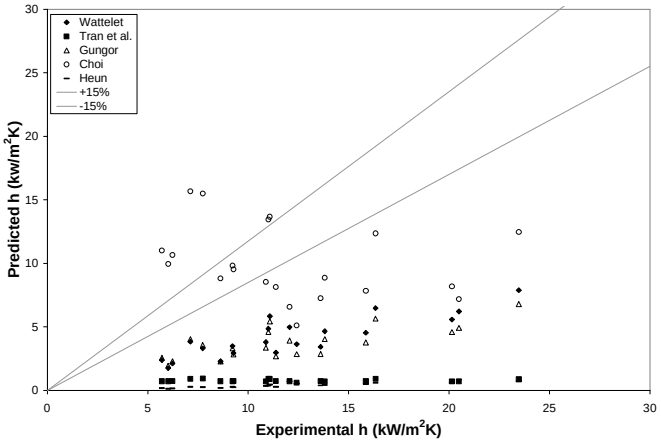

Figure 5.28: Heat Transfer Correlation Comparison for Enhanced Test Section in Evaporation—Mid Geometry

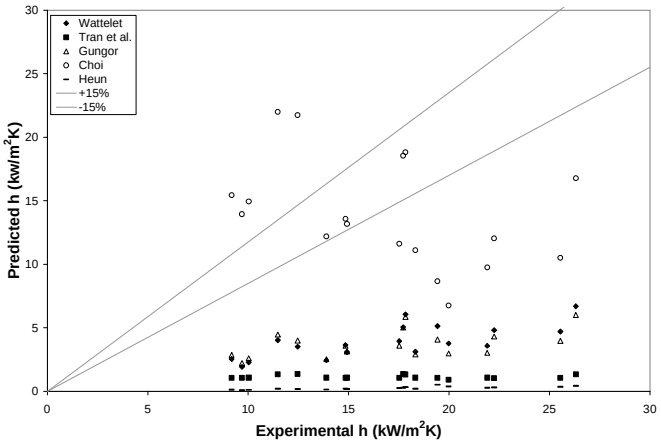

Figure 5.29: Heat Transfer Correlation Comparison for Enhanced Test Section in Evaporation—Tip Geometry

As can be seen, the heat transfer correlations do not predict the heat transfer coefficients of either test section to a reasonable degree of accuracy. However, for the basic test section, the Wattelet (1994) and Gungor and

Winterton (1987) correlations show reasonable correlation of the experimental data, shown as the direct relation between predicted and experimental values in Figure 5.26. An interesting observation about these two correlations is that they seem to follow the same trends, with the Wattelet correlation giving just slightly higher prediction than the Gungor and Winterton correlation for all points. Although the Wattelet correlation has a superposition form and the Gungor and Winterton has as two phase multiplier form, close inspection of the two correlations shows that they use very similar groups and terms in their models.

Figures 5.27, 5.28, and 5.29 show the heat transfer correlation results for the enhanced test section Full, Mid, and Tip geometries. Changing the channel geometry does not result in an appreciable improvement in agreement with experimental data, just a systematic shift of the data points. For the Full and Mid geometries, the Wattelet and Gungor and Winterton correlations show some correlation with the experimental data.

Although not used in the previous figures, the Yun (2002) correlation was also used. Its results are shown in Figure 5.30.

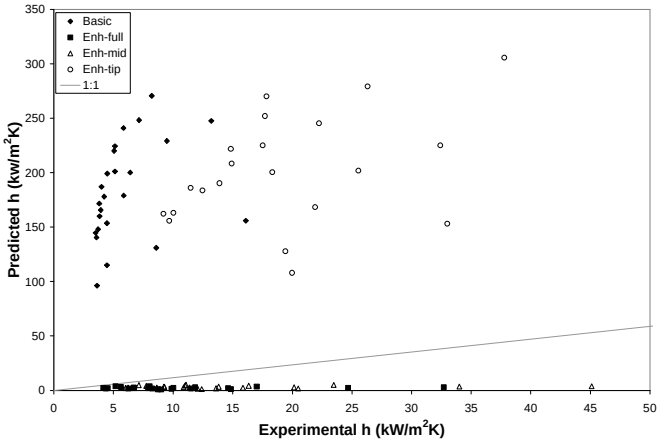

Figure 5.30: Yun (2002) Correlation Results for Evaporation Tests

The results for the Yun correlation are quite strange. For the basic test section, the correlation overpredicts the experimental data to a very high degree. For the enhanced test section Full and Mid geometries, it underpredicts the experimental data. However, when the Tip geometry is used, the Yun correlation goes back to overpredicing the experimental data by a very large amount. Changing from Mid to Tip geometry is when the hydraulic diameter increases to a value greater than 1.0 mm. This effect was also discussed for the two phase adiabatic pressure drop results, which suggests that some correlations somehow have an inherent 'critical' hydraulic diameter value of 1.0 mm that makes them perform drastically different. When applying the Wattelet correlation to the two test sections, an interesting result was found in that its two components predicted that the convective boiling contribution was always 3-4 times that of the nucleate boiling contribution.

In addition, the Yan and Lin (1998) correlation was used, but the predicted heat transfer coefficients were on the order of 10^{-13} kW/m^{2}K. These values are obviously incorrect, but the correlation was checked several times to be sure no errors were present in the equations.

5.3 Two Phase Condensation Heat Transfer

Although the main goals of this project center around characterizing the heat transfer of the enhanced geometry in evaporation, a limited range of condensation tests were also conducted. As described in section 3.2.2, the condensation tests were run at the same inlet temperature, and opposite heat transfer, as the evaporation tests. The purpose of these tests was not to fully explore the mechanisms of condensation, but to use the results as a comparison to the evaporation results in hopes of isolating the nucleate boiling contribution. Since the grooves were thought to be too small for the liquid flow to make full use of them in convection, they were thought to contribute to the total heat transfer more prominently as nucleation sites for evaporation. Because the heat transfer in evaporation was thought to be higher than in condensation, the condensation results would show the magnitude of the nucleate boiling contribution by how much lower they would be compared to the evaporation heat transfer coefficients. However, the condensation results were quite unexpected, as they did not turn out to be lower than in the evaporation results. In fact, the condensation heat transfer coefficients were higher than the evaporation heat transfer coefficients in most cases. The condensation heat transfer coefficients, plotted with the evaporation heat transfer coefficients for the same conditions for the basic and enhanced (Full geometry) test sections, are shown in Figures 5.31 and 5.32, respectively. Please note that the data points for the basic test section G=300 kg/m^{2}s, x_{avg}=0.87 and enhanced test section G=300 kg/m^{2}s, x_{avg}=0.67 are determined to have a large experimental error.

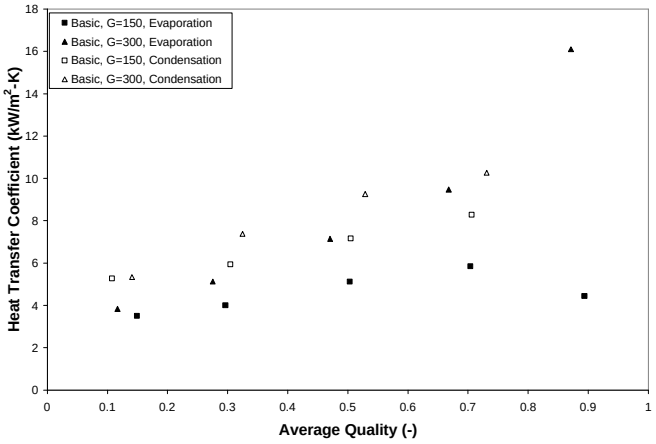

Figure 5.31: Evaporation/Condensation Comparison for Basic Test Section (Mass Flux, G, in kg/m^{2}s)

For the basic test section, the condensation heat transfer coefficients are shown to have a nearly constant separation from the evaporation heat transfer coefficients, and they follow similar slopes as the evaporation data. The condensation heat transfer coefficients increase almost linearly with mass flux and quality for low- to mid-range qualities. Unfortunately, no data was taken at higher average qualities that could show if the condensation heat transfer coefficients decreased as they did for the evaporation tests.

The condensation results for the enhanced test section show similar trends at low qualities as for the basic test section, but there are several important differences elsewhere. At a mass flux of 150 kg/m^{2}s, the condensation heat transfer coefficients are separated from the evaporation heat transfer coefficients by a much larger amount than was seen for the basic test section. Although this was not seen in the basic test section, the condensation heat transfer coefficients begin to decrease as the quality passes around 50%. This degradation in heat transfer was also

seen in evaporation, but the transition is happening at lower qualities for condensation. This can be explained by a decreased mixing effect at higher qualities, causing the liquid to not cover the entire fin and thus not taking full advantage of the heat transfer surface.

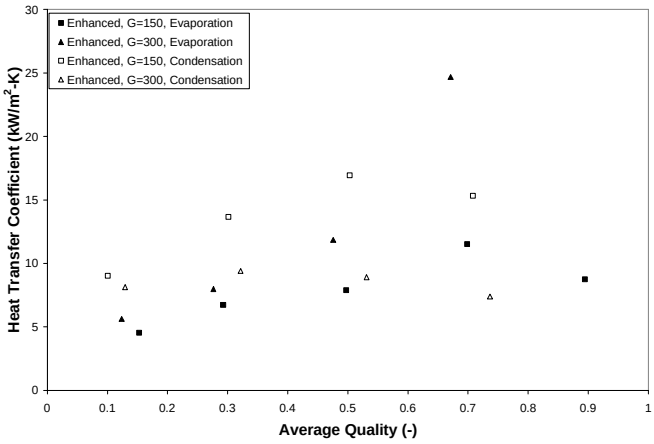

Figure 5.32: Evaporation/Condensation Comparison for Enhanced Test Section (Mass Flux, G, in kg/m^{2}s)

At a mass flux of 300 kg/m^{2}s in the enhanced test section, the condensation heat transfer coefficient becomes smaller than in evaporation. Although the highest quality data point at this mass flux in evaporation has a large error, the data point at a quality of 48% is clearly greater than the condensation heat transfer coefficients at higher qualities. This is the result that was originally expected for the condensation experiments, and suggests that the nucleate boiling contribution has increased at higher mass fluxes.

Chapter 6. Numerical Simulations

Two numerical simulations were developed in Microsoft Excel to characterize the basic and enhanced test sections. The simulations are two-dimensional models of the test section geometries that use a finite-difference method to balance the heat input for each cell. The simulation requires an iterative procedure to converge to a final solution. Depending on the size of the cells, the model can take a very long time (up to 5 hours) to converge to a solution. The input parameters for the model are: refrigerant-side temperature, refrigerant-side heat transfer coefficient, material conductivity, air-side temperature, and air-side heat transfer coefficient. Please note that the terms 'refrigerant' and 'air-side' do not necessarily imply that refrigerant and air are the fluids on either side, but rather mean the inside and outside surfaces of the model. Since the temperature and heat transfer coefficients for these surfaces can be changed, any fluid can be simulated.

Since the numerical simulation is a two-dimensional model, its purpose was not to compare with and verify the experimental data. Instead, the model offers a way to show how different input parameters effect the overall heat transfer of each geometry. By changing such parameters as material conductivity and interior and exterior heat transfer coefficients, we are able to simulate different potential applications and show how the two geometries compare in those situations.

The simulations were run at low and high values typical of the inside heat transfer coefficient results from each test section. Heat transfer coefficients of 4000 and 9000 W/m^2K were used for the basic test section, and 7500 and 15000 W/m^2K for the enhanced test section. Table 6.1 summarizes the matrix of input parameters used for the simulations. Since the simulation is two-dimensional, the heat transfer, Q_{out}, is in units of W/m. The inside and outside temperatures used for all simulations were 5 and 25ºC, respectively. The conductivities used were selected in order to simulate different materials, namely steel, aluminum, and copper with conductivities of 50, 120, and 400 W/mK, respectively. Although most parameters were chosen to simulate a standard air-to-refrigerant microchannel heat exchanger, several simulations were also run for higher outside heat transfer coefficients typical for a refrigerant flowing on the outside.

Table 6.1: Input Parameters Used for Numerical Simulations (T_{in}=5°C, T_{out}=25°C)

Geometry	k [W/mK]	h_{out} [W/m^2K]	h_{in} [W/m^2K]	Q_{out} [W/m]
Basic	50	100	4000	88.6
Basic	50	100	9000	89.7
Basic	120	100	4000	88.7
Basic	120	100	9000	89.8
Basic	120	200	4000	173.3
Basic	120	200	9000	177.7
Basic	120	4000	4000	1864.1
Basic	120	4000	9000	2525.4
Basic	120	9000	4000	2615.2
Basic	120	9000	9000	4126.8
Basic	400	100	4000	88.7
Basic	400	100	9000	89.9

Geometry	k [W/mK]	h_{out} [W/m^{2}K]	h_{in} [W/m^{2}K]	Q_{out} [W/m]
Enhanced	50	100	7500	90.1
Enhanced	50	100	15000	90.4
Enhanced	120	100	7500	90.2
Enhanced	120	100	15000	90.5
Enhanced	120	200	7500	179.1
Enhanced	120	200	15000	180.2
Enhanced	120	4000	7500	2858.8
Enhanced	120	4000	15000	3163.2
Enhanced	120	9000	7500	5104.6
Enhanced	120	9000	15000	6149.1
Enhanced	400	100	7500	90.2
Enhanced	400	100	15000	90.5

The first group of simulations were run to investigate how different materials (steel, aluminum, and copper) would effect the overall heat transfer. These simulations were typical of an air-to-refrigerant heat exchanger with an outside heat transfer coefficient of 100 W/m^{2}K. Figure 6.1 shows the results of these simulations, plotted as overall heat transfer vs. material conductivity for various inside heat transfer coefficients. This figure shows that the material conductivity has little effect on the microchannel's heat transfer. Although it appears as though the heat transfer goes up considerably, the scale in Figure 6.1 is rather small. In fact, the highest increase observed was for the basic test section with an inside heat transfer coefficient of 4000 W/m^{2}K, where the heat transfer increased by only 0.175%. Even though the effect of material conductivity was minimal, Figure 6.1 shows the impact of the inside heat transfer coefficient and channel geometry. As can be seen, the enhanced geometry has higher heat transfer than the basic geometry for both values of inside heat transfer coefficient. Although the inside heat transfer coefficients are not the same between the two geometries, the enhanced geometry gives higher heat transfer for a lower inside heat transfer coefficient (7500 W/m^{2}K) than the basic geometry for a higher inside heat transfer coefficient (9000 W/m^{2}K). This effect is primarily due to the increased areas of the enhanced geometry that can make better use of lower inside heat transfer coefficients.

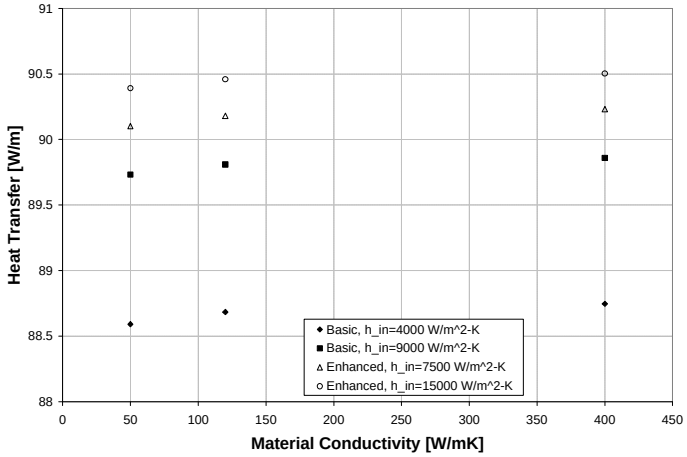

Figure 6.1: Heat Transfer vs. Material Conductivity with Constant Outside Heat Transfer Coefficient of 100 W/m^{2}K

After the material conductivity was determined to have an indistinguishable effect on heat transfer, the next set of simulations were conducted to investigate the impact of the outside heat transfer coefficient. These simulations were run at the same inside and outside temperatures as before (5 and 25ºC), and only for the conductivity of aluminum (120 W/mK). The outside heat transfer coefficients used for this set were 100, 200, 4000, and 9000 W/m^{2}K. The lower values of 100 and 200 W/m^{2}K are typical of standard air-to-refrigerant microchannel heat exchangers, while the higher values of 4000 and 9000 W/m^{2}K would be typical of refrigerant flowing on the outside of the microchannel. Figure 6.2 shows the results for the lower values of outside heat transfer coefficient.

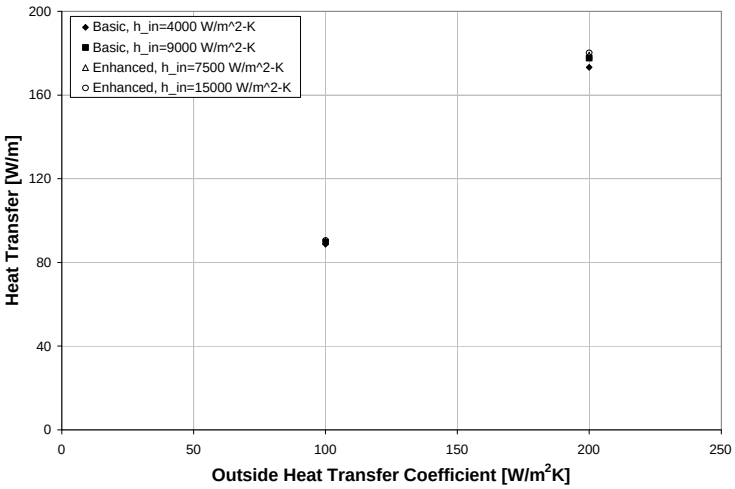

Figure 6.2: Heat Transfer vs. Outside Heat Transfer Coefficient (Low Range)

As can be seen from Figure 6.2, changing the inside heat transfer coefficient has little effect on the overall heat transfer for either geometry. For an outside heat transfer coefficient of 100 W/m^{2}K, there is only a 2.0% difference between the basic, h_{in}=4000 W/m^{2}K and the enhanced, h_{in}=15000 W/m^{2}K cases. When the outside heat transfer coefficient increases to 200 W/m^{2}K, this difference becomes more apparent and increases to 4.0%. These results show that while the enhanced geometry gives much greater inside heat transfer coefficients, they have little effect because the outside heat transfer coefficients represent the highest restriction to heat transfer for applications typical of air-to-refrigerant heat exchangers.

Although air-to-refrigerant applications do not appear to be taking advantage of the increased heat transfer coefficients of the enhanced geometry, there are several potential applications that might be able to benefit from these higher heat transfer coefficients. Some examples are a refrigerant-to-refrigerant heat exchanger using the enhanced geometry on either (or both) surfaces, or an electronics cooling application in which a high heat flux is supplied to the outside surface of the microchannel. Figure 6.3 shows the simulation results for higher outside heat transfer coefficients. For comparison, this figure also shows the results presented in Figure 6.2, which are so tightly grouped on this scale that they are shown by the two groups of points in the lowest range of outside heat transfer coefficient.

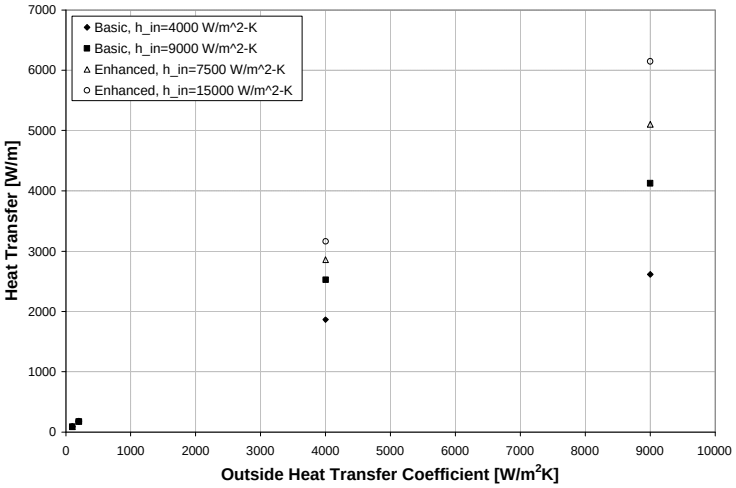

Figure 6.3: Heat Transfer vs. Outside Heat Transfer Coefficient (Full Range)

As can be seen, the various geometry and inside heat transfer coefficient combinations have very clear differences at an outside heat transfer coefficient of 4000 W/m^{2}K. If the outside heat transfer coefficient is increased to 9000 W/m^{2}K, these differences are more amplified and the heat transfer increases by almost a factor of two for the enhanced geometry. These results show that the heat transfer may not change for low values of outside heat transfer coefficient, but when it is increased, the enhanced geometry gives definite increases in heat transfer. Consequently, for applications in which high outside heat transfer coefficients or heat fluxes are possible, the increased inside heat transfer coefficient capabilities of the enhanced geometry could be used to effectively increase the total heat transfer.

Chapter 7. Conclusion

Pressure drop and heat transfer experiments were conducted to investigate the effects of internal surface enhancements in aluminum microchannels. The results of this project were presented and explained in the previous chapters.

The pressure drop results show increased pressure gradients for both adiabatic and evaporative conditions in the enhanced test section. However, the penalty factor results show diminishing effects as the mass flux and quality are increased. Pressure drop correlations gave good prediction for the basic test section. Pressure drop correlations also show that the Tip geometry gives the best prediction of experimental pressure drop results for the enhanced test section, thus suggesting that the flow acts as if the grooves are not present. Similarities in the results for the enhanced test section Full and Mid geometry suggest that there is a pseudo-critical hydraulic diameter of around 1.0 mm above which the correlations start to give better prediction of experimental results.

Heat transfer results show a definite increase in heat transfer coefficient for the enhanced test section with an average increase of a factor of two. When considering the area enhancement of the enhanced geometry, the heat transfer capacity increases by an average of a factor of four. The heat transfer correlations generally do not predict the experimental results to any reasonable degree of accuracy for any test section or geometry definition. While the pressure drop correlations were able to be applied to geometries and conditions for which they were not intended, the heat transfer correlation results suggest that there are additional mechanisms present for the enhanced geometry that have not been encountered before. The heat transfer results show that the enhanced geometry is making use of the area in the grooves to increase the heat transfer.

Numerical simulations show that enhanced geometry may not be beneficial for air-to-refrigerant heat exchanger applications, but could be used effectively to increase the heat transfer in refrigerant-to-refrigerant applications or applications with high imposed heat fluxes.

Bibliography

Ackers, W.W., H.A. Deans, and O.K. Crosser, "Condensation heat transfer within horizontal tubes," *Chemical Engineering Progress Symposium Series*, 55, 171-176, 1959.

Choi, T.Y., Y.J. Kim, M.S. Kim, and S.T. Ro, "Evaporation heat transfer of R-32, R-134a, R-32/134a, and R-32/125/134a inside a horizontal smooth tube," *International Journal of Heat and Mass Transfer*, 43, 3651-3660, 2000.

Churchill, S.W., "Friction-factor equation spans all fluid-flow regimes," *Chemical Engineering*, 84, 91-92, 1977(a).

Churchill, S.W., "Comprehensive correlating equations for heat, mass, and momentum transfer in fully developed flow in smooth tubes," *Ind. Eng. Chem. Fundam.*, 16, 109-116, 1977(b).

Colburn, A.P., "A method of correlating forced convection heat transfer data and a comparison with fluid friction," *AIChE Transactions*, 19, 174-210, 1933.

Colebrook, C.F., "Turbulent flow in pipes with particular reference to the transition region between the smooth and rough pipe laws," *Journal of the Institution of Civil Engineers*, 11, 133-156, 1938-1939.

Collier, J.G., and J.R. Thome, *Convective Boiling and Condensation*, 3rd edition, Oxford University Press, New York, 1996.

Cooper, M.G., "Saturation pool boiling—a simple correlation," *International Chemical Engineering Symposium Series*, 86, 785-792, 1984.

Dittus, F.W., and L.M.K. Boelter, "Heat transfer in automobile radiators of the tubular type," *University of California Publications on Engineering*, 2, 443-461, 1930.

Dobson, M.K., J.P. Wattelet, and J.C. Chato, "Optimal sizing of two-phase heat exchangers," ACRC Technical Report 42, 1994.

Dobson, M.K., and J.C. Chato, "Condensation in smooth horizontal tubes," *ASME Transactions Journal of Heat Transfer*, 120, 193-213, 1998.

F-Chart Software, "Engineering Equation Solver (EES)," version 6.575. Computer Software. 2002.

Friedel, L., "Improved friction pressure drop correlations for horizontal and vertical two phase pipe flow," Paper E2, European Two Phase Flow Group Meeting, Ispara, Italy, 1979.

Gnielinski, V., "New equations for heat and mass transfer in turbulent pipe and channel flow," *International Chemical Engineering*, 16, 359-368, 1976.

Gungor, K.E., and R.H.S. Winterton, "Simplified general correlation for flow saturated boiling and comparisons of correlations with data," *Chemical Engineering Research Design*, 65, 148-156, 1987.

Heun, M.K, and W.E. Dunn, "Performance and optimization of microchannel condensers," ACRC Technical Report 81, 1995.

Incropera, F.P. and D.P. Dewitt, *Fundamentals of Heat and Mass Transfer*, 4th edition, Wiley, New York, 1996.

Jung, D.S. and R. Radermacher, "Prediction of pressure drop during horizontal annular flow boiling of pure and mixed refrigerants," *International Journal of Heat and Mass Transfer*, 32, 2435-2466, 1989.

Kew, P.A., and K. Cornwell, "Correlations for the prediction of boiling heat transfer in small-diameter channels," *Applied Thermal Engineering*, 17, 705-715, 1997.

Lockhart, R.W. and R.C. Martinelli, "Proposed correlation of data for isothermal two-phase, two-component flow in pipes," *Chemical Engineering Progress*, 45, 39-48, 1949.

Moody, L.F., *ASME Transactions*, 66, 671, 1944

Newell, T.A., "ME 213 Heat Transfer Notes," University of Illinois, Spring Semester, 2000.

Nikuradse, J. (1933), "Strömungsgesetze in rauhen Rohren," *Forch.* Arb. Ing.-Wes., No361; English translation, NACA TM 1292.

Petukhov, B.S., V.A. Kurganov, and A.I. Gladuntsov, “Heat transfer in turbulent pipe flow of gases with variable properties,” *Heat Transfer Sov. Ref. 5*, no. 4, 109-116, 1973.

Prandtl, L., *Guide to Flow Theory*, Vieweg and Son, Graunschweig, 359, 1935.

Rouhani, Z., and E. Axelsson, “Calculation of volume void fraction in the subcooled and quality region,” *International Journal of Heat and Mass Transfer*, 13, 383-393, 1970.

Shah, R.K., and A.L. London, “Laminar flow forced Convection in Ducts,” in *Advances in Heat Transfer*, supplement 1, Academic Pres, New York, 1978.

Souza, A.L., J.C. Chato, J.P. Wattlet, and B.R. Christoffersen, “Pressure drop during two-phase flow of pure refrigerants and refrigerant-oil mixtures in horizontal smooth tubes,” ASME-HTD-Vol. 243, Heat Transfer with Alternative Refrigerants, 1993.

Stephan, K., and M. Abdelsalam, “Heat transfer correlations for natural convection boiling,” *International Journal of Heat and Mass Transfer*, 23, 73-87, 1980.

Tran, T.N., M.C. Chyu, M.W. Wambsganss, and D.M. France, “Boiling heat transfer with three fluids in small circular and rectangular channels,” Argonne National Laboratory, Report ANL-95-9. NTIS, Springfield, VA, 1995.

Tran, T.N., M.C. Chyu, M.W. Wambsganss, and D.M. France, “Two-phase pressure drop of refrigerants during flow boiling in small channels: an experimental investigation and correlation development,” *International Journal of Multiphase Flow*, 26, 1739-1754, 2000.

Wattelet, J.P., J.C. Chato, B.R. Christoffersen, J.A. Gaibel, M. Ponchner, P.J. Kenney, R.L. Shimon, T.C. Villanueva, N.L. Rhines, K.A. Sweeney, D.G. Allen, and T.T. Hershberger, “Heat Transfer Flow Regimes of Refrigerants in a Horizontal-Tube Evaporator,” ACRC Technical Report 55, 1994

Yan, Y-Y, and T-F Lin, “Evaporation heat transfer and pressure drop of refrigerant R-134a in a small pipe,” *International Journal of Heat and Mass Transfer*, 41, 4183-4194, 1998.

Yang, C-Y., and R.L. Webb, “Friction pressure drop of R-12 in small hydraulic diameter extruded aluminum tubes with and without micro-fins,” *International Journal of Heat and Mass Transfer*, 39, 801-809, 1996.

Yun, R., Y. Kim, K. Seo, and H.Y. Kim, “A generalized correlation for evaporation heat transfer of refrigerants in micro-fin tubes,” *International Journal of Heat and Mass Transfer*, 45, 2003-2010, 2002.

Zhang, M. and S.L. Kwon, “Two-phase frictional pressure drop for refrigerants in small diameter tubes,” Submitted to Compact Heat Exchangers and Enhancement Technology for the Process Industries, edited by R.K. Shah, Begell House, New York. 1999.

Appendix A. Sample Figures with Error Analysis

This appendix presents several copies of figures presented in previous chapters. These figures show the error in the experimental pressure drop and heat transfer measurements.

As can be seen in Figures A.1 and A.2, the error in the pressure gradient error is quite small. The error bars are so small, in fact, that they limit the readers ability to decipher between the various data sets presented in each figure. This is the reason why error bars were not included in figures presented in the actual text. In Figure A.2, the horizontal bars indicate the range over which the fluid changed quality for each experiment, with the data point representing the average quality.

Figures A.3 and A.4 show the error bars for the heat transfer coefficients in the basic and enhanced test sections, respectively. The horizontal bars indicating the quality change are not shown on these figures because it is the same information shown in Figure A.2.

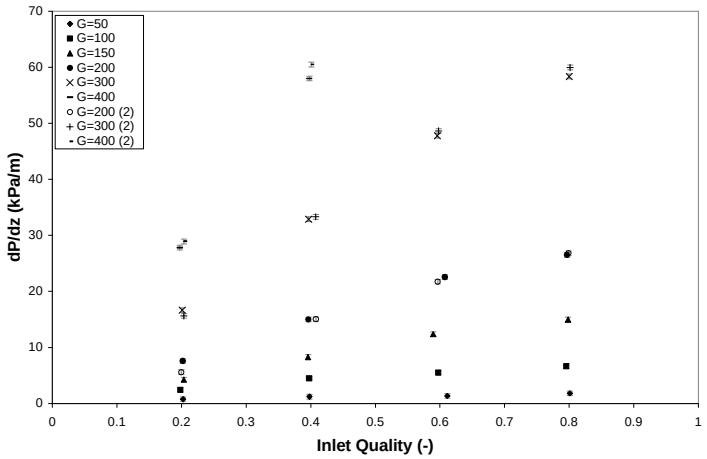

Figure A.1: Experimental Pressure Gradient vs. Inlet Quality for Basic Test Section Adiabatic Two Phase Flow, with Error Bars (Mass Flux, G, in kg/m^{2}s)

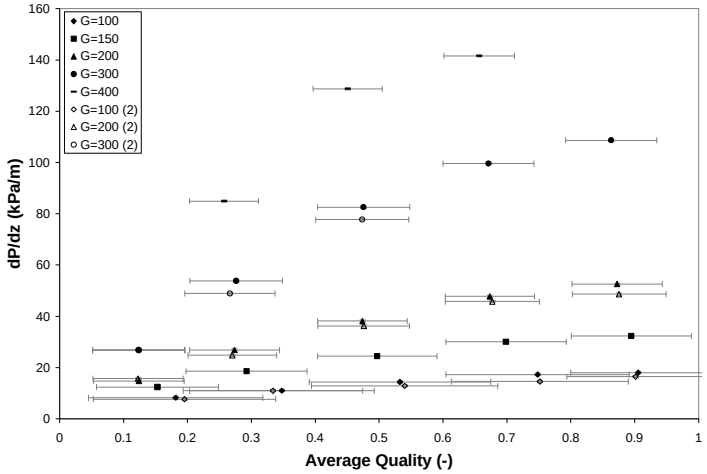

Figure A.2: Experimental Pressure Gradient vs. Average Quality for Enhanced Test Section Two Phase Flow in Evaporation, with Error and Quality Change Bars (Mass Flux, G, in kg/m^{2}s)

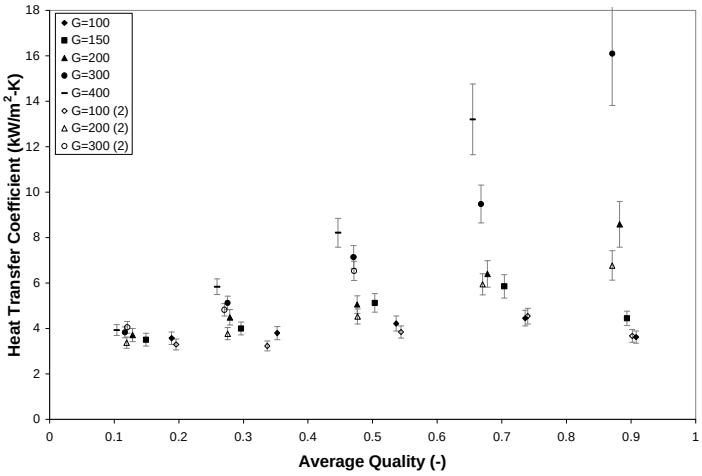

Figure A.3: Experimental Heat Transfer Coefficient vs. Average Quality for Basic Test Section Evaporative Two Phase Flow, with Error Bars (Mass Flux, G, in kg/m^{2}s)

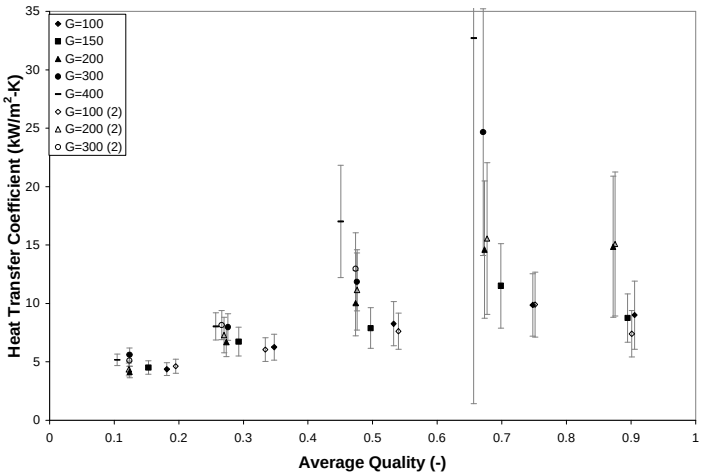

Figure A.4: Experimental Heat Transfer Coefficient vs. Average Quality for Enhanced Test Section Full Geometry Evaporative Two Phase Flow, with Error Bars (Mass Flux, G, in kg/m^{2}s)

Appendix B. Adiabatic Data

The units used in this table are: G (kg/m^2s), x_{in} (-), $T_{TS,in}$ (ºC), $T_{sat,TS,in}$ (ºC), dP_{raw} (kPa), $T_{TS,out}$ (ºC), $T_{sat,TS,out}$ (ºC).

Tube Profile	G	x_{in}	$T_{TS,in}$	$T_{sat,TS,in}$	dP_{raw}	$T_{TS,out}$	$T_{sat,TS,out}$
Basic	197	0	5.0	8.5	-0.02	5.7	8.5
Basic	198	0	4.9	9.7	0.09	5.7	9.7
Basic	291	0	7.7	11.4	0.23	7.7	11.4
Basic	299	0	4.9	10.2	0.12	5.4	10.2
Basic	303	0	4.9	9.2	0.29	5.5	9.1
Basic	304	0	5.0	9.6	0.28	5.4	9.6
Basic	332	0	5.2	11.4	0.21	5.1	11.4
Basic	376	0	3.2	5.4	0.49	3.5	5.4
Basic	405	0	5.0	6.7	0.70	5.2	6.6
Basic	402	0	5.1	8.7	0.48	5.3	8.7
Basic	410	0	2.0	5.1	0.61	2.2	5.1
Basic	428	0	1.0	5.4	0.57	1.1	5.3
Basic	150	0	2.7	14.0	0.14	4.2	14.0
Basic	151	0	5.0	5.8	0.52	5.0	5.8
Basic	149	0	9.8	14.8	0.14	9.3	14.7
Basic	180	0	7.2	10.5	0.21	7.2	10.4
Basic	209	0	5.3	8.3	0.16	5.4	8.2
Basic	241	0	3.8	10.0	0.20	4.7	10.0
Basic	270	0	2.6	10.2	0.21	3.1	10.2
Basic	300	0	2.2	11.3	0.22	2.7	11.2
Basic	299	0	9.9	15.1	0.37	9.3	15.0
Basic	329	0	8.0	15.3	0.48	8.0	15.3
Basic	371	0	6.4	11.4	0.48	6.3	11.3
Basic	401	0	5.1	11.8	0.54	5.5	11.8
Basic	431	0	4.7	13.4	0.60	5.5	13.4
Enhanced	68	0	8.3	12.1	0.02	9.4	12.1
Enhanced	68	0	8.9	12.1	0.05	9.8	12.1
Enhanced	98	0	7.8	10.8	0.13	8.6	10.8
Enhanced	138	0	7.6	10.2	0.28	8.0	10.2
Enhanced	175	0	4.6	10.2	0.56	5.0	10.2
Enhanced	204	0	4.8	6.1	0.60	5.4	6.1
Enhanced	202	0	4.9	7.8	0.79	5.3	7.7
Enhanced	209	0	6.1	12.9	0.58	7.1	12.8
Enhanced	215	0	2.6	11.1	0.47	3.7	11.1
Enhanced	241	0	5.2	11.9	1.01	6.5	11.8
Enhanced	244	0	10.7	13.1	1.13	10.2	13.0
Enhanced	246	0	2.9	12.5	0.88	4.1	12.5
Enhanced	297	0	6.9	11.2	1.42	7.0	11.1
Enhanced	302	0	4.9	8.3	1.37	5.4	8.2

Tube Profile	G	x_{in}	$T_{TS,in}$	$T_{sat,TS,in}$	dP_{raw}	$T_{TS,out}$	$T_{sat,TS,out}$
Enhanced	298	0	5.0	9.0	1.58	5.1	8.9
Enhanced	334	0	5.3	10.4	1.55	6.2	10.3
Enhanced	390	0	2.5	10.3	2.15	2.9	10.1
Enhanced	398	0	4.9	9.1	2.22	5.2	9.0
Enhanced	401	0	5.1	11.6	2.32	5.2	11.5
Enhanced	433	0	0.8	4.8	2.66	1.3	4.6
Enhanced	435	0	4.5	13.1	2.45	5.1	12.9
Enhanced	200	0	5.0	5.9	1.20	4.9	5.8
Enhanced	279	0	4.3	9.1	0.00	4.4	9.1
Enhanced	311	0	3.4	11.3	1.53	4.2	11.2
Enhanced	309	0	9.8	12.8	1.58	9.7	12.7
Enhanced	339	0	8.3	10.0	1.88	8.3	10.0
Enhanced	371	0	7.1	10.4	2.14	7.3	10.3
Enhanced	401	0	6.0	12.1	2.37	6.1	12.0
Enhanced	429	0	5.3	13.1	2.62	5.3	13.0
Basic	31	1	17.0	-10.3	0.66	15.9	-10.4
Basic	51	1	16.0	-9.8	1.44	15.3	-9.9
Basic	80	1	14.4	-8.2	2.78	14.2	-8.3
Basic	110	1	13.4	-6.1	4.40	13.5	-6.4
Basic	141	1	13.0	-3.6	6.01	13.1	-3.9
Basic	169	1	12.8	-1.6	7.68	13.1	-2.0
Basic	201	1	12.9	0.6	9.48	13.2	0.1
Basic	230	1	13.2	3.0	10.93	13.4	2.5
Basic	262	1	13.6	4.9	12.75	13.9	3.9
Enhanced	40	1	16.3	-6.4	2.40	15.1	-6.5
Enhanced	71	1	15.0	-5.2	5.22	14.4	-5.5
Enhanced	101	1	14.1	-3.9	8.46	14.0	-4.4
Enhanced	130	1	13.7	-2.4	11.88	13.9	-3.0
Enhanced	160	1	13.2	-2.0	16.26	13.3	-3.7
Enhanced	191	1	13.1	0.1	20.04	13.4	-1.9
Enhanced	220	1	13.3	2.4	23.42	13.7	0.3
Enhanced	249	1	13.7	4.7	26.55	14.5	2.4
Basic	50	0.40	5.0	5.3	0.50	5.02	5.24
Basic	49	0.61	5.0	5.2	0.56	4.96	5.17
Basic	51	0.80	4.9	5.1	0.75	4.89	5.07
Basic	101	0.20	5.1	5.3	1.01	5.00	5.23
Basic	102	0.40	5.1	5.3	1.86	4.93	5.15
Basic	101	0.60	5.0	5.2	2.27	4.80	5.03
Basic	101	0.80	5.0	5.2	2.73	4.68	4.93
Basic	148	0.20	5.0	5.4	1.76	4.88	5.23
Basic	150	0.40	5.0	5.3	3.42	4.77	5.01
Basic	150	0.59	5.0	5.0	5.10	4.56	4.62
Basic	150	0.80	5.0	5.2	6.16	4.42	4.66
Basic	202	0.20	5.0	5.0	3.13	4.74	4.79

Tube Profile	G	x_{in}	$T_{TS,in}$	$T_{sat,TS,in}$	dP_{raw}	$T_{TS,out}$	$T_{sat,TS,out}$
Basic	201	0.40	5.0	5.2	6.19	4.49	4.67
Basic	203	0.61	5.1	5.1	9.30	4.20	4.35
Basic	200	0.80	5.0	5.1	10.90	4.00	4.19
Basic	301	0.20	5.1	5.2	6.88	4.45	4.66
Basic	301	0.40	5.0	5.1	13.57	3.77	3.98
Basic	300	0.60	5.1	5.0	19.69	3.21	3.39
Basic	299	0.80	5.0	4.9	23.94	2.72	2.90
Basic	400	0.20	5.0	5.0	11.48	3.93	4.03
Basic	402	0.40	4.9	4.9	23.91	2.69	2.83
Enhanced	52	0.20	5.0	5.2	1.11	4.93	5.15
Enhanced	50	0.40	5.0	5.3	1.38	4.89	5.16
Enhanced	51	0.60	5.0	5.2	1.74	4.89	5.10
Enhanced	49	0.80	4.9	5.2	1.78	4.82	5.04
Enhanced	100	0.20	5.0	5.3	2.89	4.81	5.02
Enhanced	103	0.40	5.0	5.2	4.22	4.66	4.87
Enhanced	102	0.60	5.0	5.2	5.22	4.59	4.81
Enhanced	100	0.80	5.1	5.2	5.86	4.53	4.76
Enhanced	152	0.20	5.0	5.3	4.49	4.68	4.90
Enhanced	150	0.41	5.0	5.2	7.73	4.35	4.57
Enhanced	150	0.61	5.0	4.8	10.32	4.09	3.95
Enhanced	150	0.79	5.0	5.2	12.07	3.93	4.15
Enhanced	199	0.20	5.0	5.1	7.33	4.42	4.46
Enhanced	201	0.39	5.0	5.1	12.28	3.89	4.06
Enhanced	201	0.61	5.0	4.8	17.80	3.37	3.32
Enhanced	200	0.80	4.9	5.0	20.42	3.07	3.23
Enhanced	300	0.21	5.0	5.0	15.11	3.60	3.77
Enhanced	297	0.41	5.0	5.0	27.18	2.53	2.72
Enhanced	301	0.59	5.0	4.9	36.41	1.63	1.80
Enhanced	299	0.80	5.0	4.8	42.20	0.98	1.18
Enhanced	402	0.20	5.0	5.0	24.69	2.82	2.94
Enhanced	403	0.40	5.0	4.8	46.42	0.68	0.77
Basic	202	0.20	5.0	5.7	2.30	4.75	5.60
Basic	198	0.41	5.0	5.8	6.22	4.48	5.52
Basic	203	0.60	5.0	5.7	8.96	4.16	5.32
Basic	200	0.80	5.0	5.7	11.02	3.96	5.22
Basic	298	0.20	5.0	5.8	6.45	4.37	5.52
Basic	297	0.41	5.0	5.6	13.74	3.72	4.57
Basic	301	0.60	5.1	5.7	20.04	3.21	4.05
Basic	299	0.80	4.9	5.2	24.61	2.53	3.17
Basic	401	0.20	4.9	5.6	11.94	3.82	4.86
Basic	401	0.40	4.9	5.5	24.97	2.57	3.38
Enhanced	199	0.20	5.0	5.8	6.74	4.43	5.49
Enhanced	199	0.40	5.0	5.8	12.53	3.89	4.99
Enhanced	200	0.60	5.1	5.8	17.43	3.53	4.35

Tube Profile	G	x_{in}	$T_{TS,in}$	$T_{sat,TS,in}$	dP_{raw}	$T_{TS,out}$	$T_{sat,TS,out}$
Enhanced	201	0.80	4.9	5.7	20.51	3.06	4.05
Enhanced	297	0.20	5.0	5.7	14.98	3.71	4.55
Enhanced	298	0.41	5.0	5.7	27.28	2.55	3.42
Enhanced	299	0.60	4.9	5.4	37.39	1.43	2.27
Enhanced	301	0.80	5.0	5.2	44.11	0.76	1.42
Enhanced	399	0.20	5.0	5.8	26.34	2.68	3.58
Enhanced	402	0.40	5.0	5.5	47.85	0.49	1.40

Appendix C. Heat Transfer Data

The units used in this table are: G (kg/m^2s), x_{in} (-), $T_{TS,in}$ (ºC), $T_{sat,TS,in}$ (ºC), dP_{raw} (kPa), $T_{TS,out}$ (ºC), $T_{sat,TS,out}$ (ºC), Q_{water} (kW), dx (-), htc (kW/m^2K).

Tube Profile	G	x_{in}	$T_{TS,in}$	$T_{sat,TS,in}$	dP_{raw}	$T_{TS,out}$	$T_{sat,TS,out}$	Q_{water}	dx	htc
Basic	108	0	7.3	18.4	-0.36	17.1	18.4	0.026	-	0.23
Basic	111	0	6.6	17.2	-1.25	16.6	17.3	0.030	-	0.27
Basic	141	0	5.8	16.0	-0.66	15.0	16.0	0.024	-	0.22
Basic	142	0	6.0	17.4	-0.85	15.9	17.4	0.030	-	0.25
Basic	171	0	5.7	20.3	-0.10	14.6	20.3	0.029	-	0.25
Basic	171	0	5.6	20.5	-0.26	15.7	20.5	0.034	-	0.26
Basic	200	0	7.6	20.8	-0.08	14.4	20.7	0.025	-	0.23
Basic	199	0	7.8	21.0	-0.08	14.7	21.0	0.030	-	0.27
Basic	198	0	8.0	21.8	-0.11	15.6	21.8	0.041	-	0.34
Basic	231	0	5.5	21.4	0.05	13.1	21.4	0.030	-	0.24
Basic	231	0	5.4	21.4	0.04	12.9	21.4	0.035	-	0.28
Basic	232	0	5.4	21.3	0.06	13.4	21.3	0.049	-	0.36
Basic	249	0	6.6	13.9	-0.21	12.7	13.9	0.021	-	0.24
Basic	249	0	6.6	14.5	-0.26	13.4	14.5	0.026	-	0.27
Basic	282	0	5.4	13.3	0.14	10.4	13.3	0.018	-	0.22
Basic	281	0	5.4	13.9	0.08	11.2	13.9	0.023	-	0.25
Basic	281	0	5.4	13.8	-0.21	11.9	13.8	0.030	-	0.30
Basic	305	0	4.5	15.0	0.23	10.2	14.9	0.027	-	0.31
Basic	305	0	4.8	16.6	0.14	11.1	16.6	0.032	-	0.35
Basic	340	0	5.5	12.6	0.38	11.0	12.6	0.026	-	0.35
Basic	340	0	5.5	12.5	0.43	10.8	12.5	0.027	-	0.38
Basic	370	0	4.1	11.3	0.79	8.5	11.3	0.023	-	0.39
Basic	369	0	4.2	11.6	0.73	9.2	11.5	0.023	-	0.35
Basic	370	0	4.1	11.5	0.76	8.9	11.4	0.025	-	0.39
Basic	405	0	3.0	10.3	0.81	7.8	10.3	0.032	-	0.50
Basic	404	0	3.1	10.7	0.65	8.8	10.6	0.036	-	0.49
Basic	404	0	3.0	10.6	0.64	8.6	10.6	0.037	-	0.51
Basic	435	0	2.5	10.1	0.68	7.2	10.1	0.026	-	0.40
Basic	436	0	2.7	10.2	0.78	7.4	10.2	0.033	-	0.52
Basic	437	0	2.6	10.6	0.73	8.3	10.5	0.043	-	0.58
Enhanced	103	0	8.5	21.5	-12.50	18.7	21.8	0.024	-	0.12
Enhanced	101	0	8.9	21.7	-12.38	20.1	22.0	0.030	-	0.13
Enhanced	135	0	6.5	18.0	-0.13	16.5	18.0	0.029	-	0.15
Enhanced	133	0	7.6	22.1	-12.30	18.6	22.4	0.035	-	0.16
Enhanced	161	0	5.6	17.7	0.10	15.3	17.7	0.031	-	0.17
Enhanced	161	0	5.8	17.7	0.01	16.3	17.7	0.038	-	0.19
Enhanced	190	0	6.0	20.8	0.73	14.8	20.8	0.031	-	0.19
Enhanced	190	0	6.0	21.4	0.48	16.0	21.4	0.042	-	0.22
Enhanced	220	0	5.8	15.2	0.59	13.5	15.2	0.028	-	0.20
Enhanced	222	0	5.8	16.1	0.49	14.6	16.1	0.039	-	0.24
Enhanced	252	0	5.6	18.8	0.99	12.1	18.8	0.024	-	0.20

Tube Profile	G	x_{in}	$T_{TS,in}$	$T_{sat,TS,in}$	dP_{raw}	$T_{TS,out}$	$T_{sat,TS,out}$	Q_{water}	dx	htc
Enhanced	248	0	6.1	18.5	0.95	13.3	18.5	0.030	-	0.23
Enhanced	245	0	6.1	18.5	0.86	14.2	18.4	0.039	-	0.26
Enhanced	282	0	5.0	17.3	1.19	11.3	17.2	0.028	-	0.24
Enhanced	282	0	5.0	17.5	1.17	12.2	17.5	0.037	-	0.28
Enhanced	309	0	4.8	17.7	1.45	10.9	17.7	0.030	-	0.27
Enhanced	308	0	4.9	17.9	1.40	11.9	17.9	0.039	-	0.31
Enhanced	341	0	5.3	16.8	1.71	10.5	16.8	0.026	-	0.27
Enhanced	340	0	5.5	16.9	1.67	11.3	16.9	0.032	-	0.31
Enhanced	373	0	4.6	18.8	2.05	10.3	18.7	0.034	-	0.33
Enhanced	372	0	4.6	19.1	2.03	11.3	19.1	0.045	-	0.38
Enhanced	397	0	4.3	20.2	2.36	9.1	20.1	0.025	-	0.30
Enhanced	396	0	4.3	20.3	2.33	10.1	20.2	0.039	-	0.38
Enhanced	429	0	3.4	11.5	2.48	8.8	11.4	0.036	-	0.37
Enhanced	429	0	3.5	12.7	2.35	10.2	12.6	0.054	-	0.45
Basic	110	1	18.5	4.3	2.94	26.3	4.2	0.014	-	0.18
Basic	109	1	19.0	4.0	3.00	28.5	3.8	0.022	-	0.23
Basic	141	1	17.4	4.4	4.51	26.0	4.2	0.021	-	0.23
Basic	139	1	17.7	3.9	4.64	28.6	3.7	0.032	-	0.29
Basic	172	1	16.6	4.3	6.42	25.8	4.0	0.027	-	0.29
Basic	169	1	16.6	3.8	6.54	28.3	3.5	0.040	-	0.33
Basic	199	1	16.2	4.3	8.37	25.6	3.9	0.033	-	0.34
Basic	202	1	15.8	3.8	8.94	28.0	3.4	0.048	-	0.38
Basic	231	1	15.8	4.5	10.80	25.3	4.0	0.038	-	0.39
Basic	231	1	15.3	3.9	11.39	27.8	3.4	0.055	-	0.43
Basic	260	1	15.9	4.6	13.40	25.1	3.4	0.042	-	0.44
Basic	264	1	15.3	5.3	13.63	27.5	4.1	0.061	-	0.49
Enhanced	112	1	18.3	4.6	6.34	26.2	4.4	0.013	-	0.08
Enhanced	110	1	18.8	4.5	6.41	29.0	4.2	0.024	-	0.11
Enhanced	137	1	17.3	4.6	9.18	26.1	4.2	0.020	-	0.11
Enhanced	141	1	17.6	5.1	9.66	28.8	4.7	0.032	-	0.14
Enhanced	169	1	16.6	5.4	12.77	25.9	4.4	0.027	-	0.14
Enhanced	169	1	16.6	5.0	13.29	28.5	3.9	0.040	-	0.17
Enhanced	203	1	16.0	6.2	17.19	25.7	4.8	0.034	-	0.18
Enhanced	202	1	15.7	5.4	18.04	28.3	3.9	0.049	-	0.20
Enhanced	231	1	15.7	6.3	21.64	25.5	4.5	0.039	-	0.20
Enhanced	230	1	15.3	5.8	22.48	28.0	4.0	0.056	-	0.22
Enhanced	259	1	16.0	6.6	26.60	25.3	4.4	0.044	-	0.23
Enhanced	259	1	15.2	6.2	27.54	27.8	4.0	0.063	-	0.25
Basic	100	0.05	5.1	5.9	1.34	5.1	5.9	0.098	0.28	3.57
Basic	99	0.21	4.9	5.8	2.07	4.8	5.6	0.101	0.29	3.80
Basic	101	0.39	5.1	5.9	2.68	4.9	5.8	0.099	0.28	4.21
Basic	102	0.59	5.1	5.9	3.45	4.8	5.8	0.101	0.28	4.45
Basic	102	0.81	4.9	5.6	3.73	4.6	5.4	0.075	0.21	3.62
Basic	150	0.05	5.1	5.9	2.19	5.0	5.8	0.100	0.19	3.51
Basic	152	0.20	5.0	5.9	3.37	4.7	5.7	0.100	0.19	4.00

Tube Profile	G	x_{in}	$T_{TS,in}$	$T_{sat,TS,in}$	dP_{raw}	$T_{TS,out}$	$T_{sat,TS,out}$	Q_{water}	dx	htc
Basic	149	0.41	4.9	5.6	5.29	4.5	5.4	0.100	0.19	5.12
Basic	149	0.61	5.0	5.8	6.33	4.5	5.5	0.100	0.19	5.86
Basic	150	0.80	5.0	5.7	6.84	4.4	5.4	0.100	0.19	4.44
Basic	200	0.06	5.0	5.8	3.17	4.8	5.7	0.102	0.14	3.71
Basic	200	0.21	5.1	5.7	5.16	4.7	5.4	0.100	0.14	4.48
Basic	201	0.40	5.0	5.7	8.48	4.2	5.3	0.102	0.14	5.05
Basic	200	0.61	5.1	5.8	10.77	4.1	5.3	0.102	0.14	6.40
Basic	199	0.81	5.1	5.7	11.46	4.0	5.1	0.102	0.15	8.59
Basic	300	0.05	5.0	5.9	4.98	4.7	5.6	0.147	0.14	3.83
Basic	300	0.20	4.9	5.6	10.68	4.0	5.0	0.149	0.14	5.12
Basic	302	0.40	5.0	5.6	17.61	3.4	4.2	0.148	0.14	7.14
Basic	301	0.60	5.0	5.6	23.24	2.9	3.7	0.150	0.14	9.47
Basic	301	0.80	5.0	5.4	24.78	2.6	3.4	0.151	0.14	16.10
Basic	400	0.05	5.0	5.8	7.58	4.5	5.4	0.148	0.11	3.92
Basic	402	0.21	4.9	5.6	17.89	3.4	4.1	0.149	0.11	5.84
Basic	402	0.39	5.1	5.6	28.84	2.5	3.2	0.148	0.11	8.21
Basic	401	0.60	6.4	6.9	36.31	3.0	3.9	0.149	0.11	13.20
Enhanced	101	0.05	5.0	5.9	3.44	4.8	5.8	0.098	0.27	4.36
Enhanced	98	0.20	5.1	5.9	4.59	4.8	5.7	0.099	0.29	6.26
Enhanced	104	0.39	5.0	5.9	6.00	4.6	5.6	0.100	0.28	8.25
Enhanced	101	0.60	5.0	5.8	7.18	4.4	5.5	0.101	0.29	9.86
Enhanced	101	0.80	5.0	5.8	7.47	4.4	5.5	0.075	0.21	9.00
Enhanced	149	0.06	5.0	5.8	5.17	4.6	5.6	0.100	0.19	4.52
Enhanced	153	0.20	5.1	5.8	7.75	4.5	5.5	0.100	0.19	6.72
Enhanced	149	0.40	4.9	5.8	10.18	4.1	5.3	0.098	0.19	7.89
Enhanced	151	0.60	5.0	5.8	12.47	3.9	4.9	0.100	0.19	11.51
Enhanced	150	0.80	5.0	5.8	13.37	3.8	4.7	0.100	0.19	8.75
Enhanced	198	0.05	5.1	6.0	6.13	4.6	5.7	0.099	0.14	4.13
Enhanced	200	0.20	5.0	5.7	11.19	4.1	5.1	0.099	0.14	6.69
Enhanced	200	0.40	5.0	5.8	15.87	3.6	4.5	0.098	0.14	10.02
Enhanced	200	0.60	5.0	5.8	19.80	3.3	4.1	0.098	0.14	14.61
Enhanced	200	0.80	5.0	5.6	21.75	3.0	3.8	0.099	0.14	14.86
Enhanced	301	0.05	5.0	5.7	11.09	4.1	5.0	0.152	0.14	5.61
Enhanced	301	0.20	5.0	5.7	22.39	3.0	3.8	0.152	0.14	7.98
Enhanced	302	0.40	5.0	5.6	34.28	1.9	2.7	0.152	0.14	11.85
Enhanced	301	0.60	5.0	5.5	41.23	1.2	2.0	0.150	0.14	24.67
Enhanced	401	0.05	5.1	5.8	15.76	3.7	4.6	0.148	0.11	5.16
Enhanced	401	0.20	5.0	5.7	35.31	1.9	2.7	0.150	0.11	8.03
Enhanced	400	0.40	5.2	5.8	53.44	0.3	1.2	0.150	0.11	17.02
Enhanced	396	0.60	8.0	8.4	58.53	3.0	3.8	0.150	0.11	32.71
Basic	102	0.05	5.0	5.2	1.26	4.9	5.1	0.102	0.29	3.29
Basic	102	0.20	5.0	5.2	1.87	4.9	5.1	0.100	0.28	3.23
Basic	100	0.40	5.0	5.3	2.41	4.9	5.1	0.100	0.28	3.84
Basic	101	0.60	5.1	5.3	2.92	4.8	5.1	0.100	0.28	4.54
Basic	101	0.80	5.0	5.3	3.18	4.8	5.0	0.075	0.21	3.67

Tube Profile	G	x_{in}	$T_{TS,in}$	$T_{sat,TS,in}$	dP_{raw}	$T_{TS,out}$	$T_{sat,TS,out}$	Q_{water}	dx	htc
Basic	202	0.05	5.0	5.2	2.74	4.9	5.0	0.098	0.14	3.37
Basic	200	0.20	5.0	5.2	4.39	4.7	4.9	0.102	0.15	3.77
Basic	199	0.40	5.0	5.2	7.32	4.4	4.6	0.102	0.15	4.53
Basic	201	0.60	5.0	5.2	10.24	4.1	4.4	0.101	0.14	5.94
Basic	204	0.80	5.1	5.2	11.35	4.0	4.3	0.101	0.14	6.77
Basic	302	0.05	5.1	5.2	5.00	4.8	4.7	0.151	0.14	4.05
Basic	302	0.20	4.9	5.0	9.73	4.1	4.2	0.152	0.14	4.82
Basic	302	0.40	5.0	5.0	17.53	3.4	3.6	0.151	0.14	6.53
Enhanced	99	0.05	5.0	5.2	3.15	4.8	4.9	0.100	0.29	4.62
Enhanced	102	0.19	5.0	5.2	4.53	4.7	4.8	0.101	0.28	6.05
Enhanced	101	0.39	4.9	5.2	5.32	4.5	4.8	0.104	0.29	7.62
Enhanced	100	0.61	5.1	5.3	6.01	4.6	4.8	0.098	0.28	9.90
Enhanced	101	0.79	5.0	5.2	6.78	4.4	4.6	0.076	0.22	7.40
Enhanced	199	0.05	5.1	5.3	6.59	4.6	4.8	0.098	0.14	4.35
Enhanced	200	0.20	5.1	5.2	10.32	4.2	4.4	0.097	0.14	7.29
Enhanced	200	0.40	5.1	5.2	15.06	3.8	3.9	0.100	0.14	11.16
Enhanced	200	0.60	5.0	5.1	19.00	3.4	3.5	0.103	0.15	15.55
Enhanced	199	0.80	5.0	5.0	20.11	3.1	3.3	0.102	0.15	15.09
Enhanced	300	0.05	5.0	5.1	11.22	4.1	4.2	0.150	0.14	5.11
Enhanced	302	0.20	5.1	5.2	20.32	3.4	3.5	0.148	0.14	8.15
Basic	151	0.20	5.1	6.0	1.53	4.8	6.0	-0.101	-0.19	5.28
Basic	150	0.40	5.0	5.9	3.06	4.7	5.8	-0.099	-0.19	5.94
Basic	149	0.60	4.8	5.7	4.67	4.4	5.5	-0.099	-0.19	7.17
Basic	150	0.80	4.9	5.5	5.89	4.3	5.3	-0.100	-0.19	8.28
Basic	300	0.21	4.8	5.7	5.24	4.2	5.5	-0.144	-0.14	5.34
Basic	300	0.40	5.1	5.7	11.31	4.0	5.1	-0.152	-0.15	7.38
Basic	301	0.60	5.0	5.6	18.62	3.3	4.1	-0.150	-0.14	9.26
Basic	301	0.80	5.1	5.6	23.10	2.9	3.6	-0.148	-0.14	10.27
Enhanced	154	0.19	5.1	6.1	3.72	4.8	5.9	-0.100	-0.19	9.02
Enhanced	149	0.40	5.1	6.1	6.95	4.6	5.8	-0.102	-0.19	13.65
Enhanced	149	0.60	5.0	5.8	9.02	4.2	5.5	-0.100	-0.19	16.93
Enhanced	149	0.80	4.9	5.7	11.45	3.9	5.2	-0.100	-0.19	15.31
Enhanced	299	0.20	4.9	5.6	11.58	3.8	4.9	-0.151	-0.15	8.12
Enhanced	303	0.39	5.1	5.7	22.91	3.0	3.8	-0.151	-0.14	9.39
Enhanced	301	0.60	5.0	5.5	34.61	1.8	2.5	-0.152	-0.14	8.90
Enhanced	300	0.80	5.0	5.3	41.82	1.0	1.7	-0.133	-0.13	7.38